Design, Characterization, and Manufacturing of Ultra-sharp Metallic Probes for Near-field Optics

A DISSERTATION

SUBMITTED TO THE FACULTY OF THE GRADUATE SCHOOL

OF THE UNIVERSITY OF MINNESOTA

BY

Timothy Walter Johnson

IN PARTIAL FULFILLMENT OF THE REQUIREMENTS

FOR THE DEGREE OF

Doctor of Philosophy

Sang-Hyun Oh

May, 2014

Acknowledgements

I would first like to thank my advisor, Professor Sang-Hyun Oh, for his continued support, guidance, and motivation throughout my research. I would also like to thank the numerous collaborators who have contributed to this work since it is though their knowledge and expertise that I have been able to apply my work to a broad range of areas. A special thanks goes out to my fellow lab members, especially to the initial group consisting of Nate Lindquist, Antoine Lesuffleur, Hyungsoon Im, Si-Hoon Lee, and Nate Wittenberg for helping to teach me and providing me a solid foundation. Current lab members including Jonah Shaver, Luke Jordan, Xiaoshu Chen, Shailabh Kumar, Avijit Barik, Lauren Otto, Dan Klemme, and Steve Olson have also helped provide me with great support and good friendships through this time.

I would also like to thank my family and friends for all the support, distractions, and fun they provided during these past six years. My parents, Craig and Judy Johnson get top honors along with my sisters and their families, Minda, Moy, and Rafa Gomez and Janelle, Matt, Micah, and Jonah Knutson. Additionally, Rob, Caroline, Christine, and Sarah Olsen have been a great support. I would also like to thank my great friends who have traveled alongside of me including, but certainly not limited to: Cory Lindh, Randy Johnson, and Thomas Finn for being my core group since high school, and also Bret Larson, Kendra Finn, Sarah Anderson, Jay Woodbury, Darcy Huspek, Tyler Gerdin, Eric Tuininga, Lindsey Cline, Bethany Fast, and Kirsten Babb. All of these people helped me make it through, and I know I couldn't have done it alone.

Dedication

I dedicate this dissertation to my parents, Craig and Judy Johnson, for all of their love and support throughout my life.

I also dedicate it to the one I have dedicated my life to, Jesus Christ.

Abstract

The ability to manipulate and nanofocus light has many potential applications such as surface-enhanced spectroscopy, optical trapping, heat-assisted magnetic recording, and near-field imaging. In this thesis a new method to fabricate devices for nanofocusing is introduced and then demonstrated for use in near-field imaging. This method uses a sharp, metallic tip to confine and focus the light. Current methods to produce these sharp tips suffer from low reliability and low-throughput processing methods. Here a fabrication method called template stripping is introduced. With this method, precise control over the fabrication of metal films with integrated bumps, grooves, and holes is shown. Next, the method is used to fabricate sharp, metallic tips. The tips are used for near-field imaging and show a resolution of $<$20 nm and observed fluorescence enhancements of $\approx$200x from single fluorescent molecules. The tips are also demonstrated for near-field Raman imaging of carbon nanotube bundles and show good results. These tips provide high-quality results, but one of the more important features is that the yield of the tips is around 95%, much higher than current methods for fabricating sharp, metallic tips. Also, different schemes to create nanofocusing are presented. One method makes use of an asymmetric metal deposition and another a C-shaped aperture around the tip to focus light illuminating the tip from inside itself. Both of these methods show significant nanofocusing and provide new structures for nanofocusing studies. The processes to fabricate these structures are developed with the hope that they will be widely disseminated to allow more researchers access to reliable tips and hopefully bringing more people into the field of near-field imaging.

Contents

List of Tables

List of Figures

List of Publications

The following contains work has been produced though a collaborative effort, and is largely derived from the following publications. Throughout this dissertation, an attempt was made to describe where the work was shared with collaborators and colleagues. These are the publications I have completed during during the time working on this dissertation. Not all are referenced in this dissertation, but represent other work completed.

1. Im, H., Lee, S. H., Wittenberg, N. J., Johnson, T. W., Lindquist, N. C., Nagpal, P., Norris, D. J. & Oh, S.-H. Template-stripped smooth Ag nanohole arrays with silica shells for surface plasmon resonance biosensing. *ACS Nano* **5**, 6244-6253 (2011).[1]

2. Wittenberg, N. J., Im, H., Johnson, T. W., Xu, X., Warrington, A. E., Rodriguez, M. & Oh, S.-H. Facile assembly of micro- and nanoarrays for sensing with natural cell membranes. *ACS Nano* **5**, 7555-64 (2011).[2]

3. Lindquist, N. C., Johnson, T. W., Norris, D. J., and Oh, S.-H. Monolithic integration of continuously tunable plasmonic nanostructures. *Nano Letters* **11**, 3526 (2011).[3]

4. Luhman, W. A., Hoon Lee, S., Johnson, T. W., Holmes, R. J. & Oh, S.-H. Self-assembled plasmonic electrodes for high-performance organic photovoltaic cells.

Applied Physics Letters **99**, 103306 (2011).[4]

5. Lee, S. H., Johnson, T. W., Lindquist, N. C., Im, H., Norris, D. J. & Oh, S.-H. Linewidth-Optimized Extraordinary Optical Transmission in Water with Template Stripped Metallic Nanohole Arrays. *Advanced Functional Materials* **22**, 4439-4446 (2012).[5]

6. Wittenberg, N. J., Johnson, T. W. & Oh, S.-H. High-density arrays of submicron spherical supported lipid bilayers. Analytical Chemistry 84, 8207-8213 (2012).[6]

7. Lindquist, N. C., Johnson, T. W., Jose, J., Otto, L. M. & Oh, S.-H. Ultrasmooth metallic films with buried nanostructures for backside reflection-mode plasmonic biosensing. *Annalen der Physik* **524**, 687-696 (2012).[7]

8. Johnson, T. W., Lapin, Z. J., Beams, R., Lindquist, N. C., Rodrigo, S. G., Novotny, L. & Oh, S.-H. Highly reproducible near-field optical imaging with sub-20-nm resolution based on template stripped gold pyramids. *ACS Nano* **6**, 9168-9174 (2012).[8]

9. Olmon, R. L., Slovick, B., Johnson, T. W., Shelton, D., Oh, S.-H., Boreman, G. D., and Raschke, M. B. Optical dielectric function of gold. *Physical Review B* **86**, 235147 (2012).[9]

10. Lindquist, N. C., Johnson, T. W., Nagpal, P., Norris, D. J., & Oh, S.-H. Plasmonic nanofocusing with a metallic pyramid and an integrated C-shaped aperture. *Scientic Reports* **3**, 1857 (2013).[10]

11. Jose, J., Jordan, L. R., Johnson, T. W., Lee, S. H., Wittenberg, N. J. & Oh, S.-H. Topographically Flat Substrates with Embedded Nanoplasmonic Devices for Biosensing. *Advanced Functional Materials* **23**, 2812-2820 (2013).[11]

12. Im, H., Bantz, K. C., Lee, S. H., Johnson, T. W., Haynes, C. L. & Oh, S.-H. Self-assembled plasmonic nanoring cavity arrays for SERS and LSPR biosensing.

Advanced Materials **25**, 2678-2685 (2013).[12]

13. Joy, N. a., Janiszewski, B. K., Novak, S., Johnson, T. W., Oh, S.-H., Raghunathan, A., Hartley, J. & Carpenter, M. a. Thermal Stability of Gold Nanorods for High-Temperature Plasmonic Sensing. *The Journal of Physical Chemistry C* **117**, 11718-11724 (2013).[13]

14. Lindquist, N.C., Jose, J., Cherukulappurath, S., Chen, X., Johnson, T. W., & Oh, S.-H. Tip-based plasmonics: squeezing light with metallic nanoprobes. *Laser & Photonics Reviews* **7**, 453-477 (2013).[14]

15. Reitich, F., Johnson, T. W., Oh, S.-H. & Meyer, G. A fast and high-order accurate surface perturbation method for nanoplasmonic simulations: basic concepts, analytic continuation and applications. *Journal of the Optical Society of America A* **30**, 2175-2186 (2013).[15]

16. Beams, R., Smith, D., Johnson, T. W., Oh, S.-H., Novotny, L., & Vamivakas, A. N. Nanoscale Fuorescence lifetime imaging of an optical antenna with a single diamond NV center. *Nano Letters* **13**, 3807-3811 (2013).[16]

17. Cherukulappurath, S., Johnson, T. W., Lindquist, N. C., & Oh, S.-H. Template-stripped asymmetric metallic pyramids for tunable plasmonic nanofocusing. *Nano Letters* **13**, 5635-5641 (2013).[17]

18. Wittenberg, N. J., Johnson, T. W., Jordan, L. R., Xu, X., Warrington, A. E., Rodriguez, M., & Oh, S.-H., Formation of biomembrane microarrays with a squeegee-based assembly method. *Journal of Visualized Experiments* (2014). e51501 doi: 10.3791/51501

19. Barik, A., Otto, L. M., Yoo, D., Jose, J., Johnson, T. W., and Oh, S.-H. Dielectrophoresis enhanced plasmonic sensing with gold nanohole arrays *Nano Letters* (2014).[18]

20. Jose, J., Kress, S., Barik, A., Otto, L. M., Shaver, J., Johnson, T. W., Lapin, Z. J., Bharadwaj, P., Novotny, L., & Oh, S.-H. Individual Template-Stripped Conductive Gold Pyramids for Tip-enhanced Dielectrophoresis. *ACS Photonics* (2014).[19]

Chapter 1

Introduction

1.1 Introduction and motivation

The word "light" generally refers to photons with an energy lying within or near the range of perception of our eyes. This comprises only a small portion of the electromagnetic spectrum, but is responsible for much of how we perceive the world around us. Light has the ability the transfer information about a material (e.g. color) through space which can then be spectrally isolated and interpreted by our eyes. From this basis, many scientific studies and advancements have come from our ability to manipulate light to allow us to glean more information from it. Inventions such as the telescope allowed Galileo Galilei to observe features in the sky and the microscope allowed Robert Hooke and Antony van Leeuwenhoek to observe cells in ways not possible previously, both though careful manipulation of light. With the addition of detectors and filters we are able to get even more information about the light though polarization and spectroscopic studies. This makes the use of light a powerful tool across many scientific disciplines including nanotechnology.

The field of nanotechnology has been rapidly growing and all indications point to its continued growth. The field gained traction through the miniaturization of computer

components and the results have been staggering. The first computer, the ENIAC, weighed 27 tons, had a footprint of about 167 m^2 (1800 ft^2), and consumed 150 kW of power. Partially through advancements in nanotechnology, computers today are capable today of orders of magnitude more computing power with orders of magnitude less mass, volume, and power consumption. But the push towards nanotechnology is no longer isolated to computing and now is extensively multi-disciplinary with influence in a wide range of fields. This drive is not only powered by the desire for more compact devices which require less resources to operate, but also because many interesting phenomena manifest themselves only at these length scale. Today nanotechnology is being used for everything from textiles, to food production, to medical devices, to street signs. To follow this trend of miniaturization, it is important to understand light at this scale.

Light is important at the nanoscale not only for characterization of new devices, but as an integral component to some devices as well. When light and the nanoscale intersect, they cross through what is called the diffraction limit. Due to the wave nature of light, the diffraction limit places restrictions on how tightly it can be focused in free-space to about $\lambda/2$. The same applies to information being carried by the light, where the spatial information it can carry is also limited to about the same amount. These restrictions, though, don't apply in the same way when multiple different materials as present, especially at the interfaces between the materials. The interfaces between the materials create different boundary conditions depending where the light is, allowing for increased flexibility. One especially useful interface is between a dielectric and a metal. At this interface it is possible to to create *plasmons*, which are collective oscillations of the free electrons in the metal and *surface plasmon polaritons* (SPPs) where photons are coupled to the electron oscillations forming a hybrid wave.[20] Understanding and controlling these resonances can be very powerful, but it also requires precise fabrication of features at the nanoscale to interact with them. Once materials are able to be controlled at the nanoscale, they can interact with light to provide new devices not before possible and help continue advances in nanotechnology throughout the science

community.[21–25]

There are many different types of nanostructures which harness the abilities of SPPs, making them quite versatile. One structure which seemed to spark the current increased interest consists of an array of subwavelength holes through a thin metal film. When the film is made from a plasmonic material, (such as Ag or Au in the visible) it will transmit much more light than would be expected based on the wavelength of the incident light, size of the holes, and opacity of the metal film.[26,27] This increase is partially due to surface plasmons formed on the surfaces of the metal. Metamaterials, metals with a negative refractive index,[28] have also been of interest especially since new techniques are extending their performance to optical wavelengths[29] and allowing for possibilities such as ultra-high-resolution imaging[30–32] and optical cloaking.[33–35] Even this is just scratching the surface, and there is also intense research to apply these techniques to fields such as photovoltaics,[36] optical circuitry,[37] optical trapping,[38] data storage,[39–41] surface-enhanced spectroscopy,[42–44] and biosensing.[45–49]

1.2 Scope of this thesis

The field of plasmonics is very broad with potential applications through an array of different disciplines. While many of the techniques presented here could be applied to multiple fields, the focus of this thesis is nanofocusing. Nanofocusing allows for a very small, intense spot of light to be formed in a precise location. One of the most useful methods for nanofocusing, and the one presented here, uses a sharp, metallic tip. The first problem solved in this thesis is the fabrication of such tips. A variety of methods have been used to make sharp metallic tips, but most have low throughput and low reliability. Here I present a method called template stripping which I show can produce thousands of tips in parallel with a yield of $< 95\%$. These tips are then used to perform near-field imaging experiments of single molecules. Also presented are a variety of different modalities to excite the tips to provide flexibility in nanofocusing

experiments. Finally, a number of other novel fabrication methods are presented along with a number of different plasmonic devices to be used as sensors.

1.2.1 Outline of chapters

This dissertation is organized into the following chapters, each outlining a significant portion of the original research performed throughout the dissertation.

- Chapter 2 presents the theoretical background as a basis for the other chapters. Derived from Maxwell's equations are the solution for free-space light and the solution for a surface plasmon polariton.

- Chapter 3 demonstrates a fabrication technique called template stripping which can create metallic structures with ultrasmooth surfaces. The capabilities for the method are demonstrated by the fabrication of ramped gratings, hole arrays, and bull's eyes and optical measurements are also obtained. Optical constants of template stripped films are also measured.

- Chapter 4 introduces nanofocusing which allows for light to be confined into very small and intense spots. Two new structures for nanofocusing are presented and characterized.

- Chapter 5 presents a very useful application of nanofocusing called near-field imaging. A new method to create tips to use for near-field imaging is demonstrated through the imaging of single molecules, single-walled carbon nanotubes, and single nitrogen vacancy centers.

- Chapter 6 introduces the use of surface plasmons for biosensing. A new sensor is presented and proof-of-concept experiments are performed.

- Chapter 7 provides a brief conclusion and summary of the work and a variety of ideas for future directions.

Chapter 2

Theoretical Considerations

2.1 Optical properties of metals

2.1.1 Maxwell's equations

Macroscopic electromagnetism and all its related phenomena can be described using Maxwell's equations. In 1865 J. C. Maxwell surveyed the various equations being used to explain electricity and magnetism and through some slight adjustments was able to create a set of self-consistent equations to explain electromagnetic fields and how they evolve over time.[50] These provide the foundation for our understanding of optical fields and are:

$$\nabla \cdot \mathbf{D} = \rho \tag{2.1}$$

$$\nabla \cdot \mathbf{B} = 0 \tag{2.2}$$

$$\nabla \times \mathbf{E} = -\frac{\partial \mathbf{B}}{\partial t} \tag{2.3}$$

$$\nabla \times \mathbf{H} = \mathbf{J} + \frac{\partial \mathbf{D}}{\partial t} \tag{2.4}$$

where $\mathbf{D}$ is the displacement in units of coulombs per square meter, $\mathbf{B}$ is the magnetic induction in units of tesla, $\mathbf{E}$ is the electric field in units of volts per meter, and $\mathbf{H}$ is the magnetic field in units of ampere per meter. Also, ρ is the charge density in units

of coulomb per cubic meter and **J** is the current density in ampere per square meter, both of which are zero in a region free of charges or currents, which is the case we will consider from here on. When we also limit ourselves to systems with linear, isotropic media, two more useful relations can be formed which are:

$$\mathbf{D} = \epsilon\mathbf{E} \tag{2.5}$$

$$\mathbf{B} = \mu\mathbf{H} \tag{2.6}$$

where ϵ is the electric permittivity and μ is the magnetic permeability. For convenience it is useful to further define:

$$\epsilon_r = \frac{\epsilon}{\epsilon_0} \tag{2.7}$$

$$\mu_r = \frac{\mu}{\mu_0} \tag{2.8}$$

where ϵ_r is the relative permittivity of a substance (or dielectric constant) and μ_r is the relative permeability and are both dimensionless. Also used are the fundamental constants of the electric permittivity of free space ($\epsilon_0 \approx 8.854\times10^{-12}$ F/m) and magnetic permeability if free space ($\mu_0 \approx 1.256 \times 10^{-6}$ H/m). These definitions help in future discussions. In this work we are mainly only concerned with non-magnetic materials, and so we can set $\mu_r = 1$ making $\mathbf{B} = \mu_0\mathbf{H}$.

The relationship describing how a linear material responds to an applied electric field **E** can be extended from equations (2.5) - (2.6) and given by:

$$\mathbf{D} = \epsilon_r\epsilon_0\mathbf{E} = \epsilon_0(1+\chi)\mathbf{E} = \epsilon_0\mathbf{E} + \mathbf{P} \tag{2.9}$$

where **P** is defined as the macroscopic polarization, and χ is the dielectric susceptibility. This can be simplified to:

$$\mathbf{P} = \epsilon_0\chi\mathbf{E}\ . \tag{2.10}$$

Using this foundation to describe electromagnetic fields interacting with matter we are able to look more closely at specific systems.

2.1.2 Propagating plane waves

Using Maxwell's equations it is possible to find a solution which is a traveling wave and represents the transport of energy from one point to another. This common solution for a propagating plane wave can be very useful in explaining the propagation and interactions of light. Starting with equations (2.1) – (2.4) along with equations (2.5) – (2.5), our previously stated assumptions about the material properties, and assuming a harmonic time dependence of $e^{-i\omega t}$, we can write the equations for $\mathbf{E}$ and $\mathbf{H}$ as:

$$\nabla \times \mathbf{E} - i\omega\mathbf{B} = 0 \tag{2.11}$$

$$\nabla \times \mathbf{B} - i\omega\mu\epsilon\mathbf{B} = 0\,. \tag{2.12}$$

These two equations can then be combines to form the Helmholtz wave equation:

$$(\nabla^2 + \mu\epsilon\omega^2)\left\{\frac{\mathbf{E}}{\mathbf{B}}\right\} = 0\,. \tag{2.13}$$

From here we one possible solution for $\mathbf{E}$ is:

$$\mathbf{E}(\mathbf{x}, t) = \mathbf{E_0} e^{i\mathbf{k}\cdot\mathbf{x} - i\omega t} \tag{2.14}$$

where the wave has an angular frequency of ω and wavevector $\mathbf{k}$. A similar equation can also be derived for $\mathbf{H}(\mathbf{x}, t)$. From equation (2.13) we can see there is a restriction on our wavevector of $\mathbf{k} = \sqrt{\mu\epsilon}\,\omega\,\hat{\mathbf{k}} = k\,\hat{\mathbf{k}}$. If we now define a new value $n = \sqrt{\epsilon_r\mu_r}$ and recognize that the speed of light in a vacuum is $c = 1/\sqrt{\mu_0\epsilon_0}$ we can write our wavevector as $\mathbf{k} = n\omega/c\,\hat{\mathbf{k}}$. The quantity n defined here is called the index of refraction and, since we are considering non-magnetic materials where $\mu_r = 1$, is fully described by material's dielectric constant ϵ_r. This value can also be complex to represent losses in the metal. The other term we are accustomed to when working with light is the wavelength, and is related to the wavevector through $k = 2\pi/\lambda$. This formulation can be used to describe how light interacts with matter as an electromagnetic wave.

2.1.3 Dielectric function of a metal

When light travels through different media it incurs dispersion to varying degrees. Dispersion means that the matter interacts differently with light depending on the frequency of the wave. Here we develop a simple model for the dispersion in metals. The metal is modeled as a set of electrons which are oscillating with respect to their ion cores. The equation of motion for an electron $-e$ driven by a time-varying electric field $\mathbf{E}(\mathbf{x}, t)$ can be written as:

$$m[\ddot{\mathbf{x}} + \gamma\dot{\mathbf{x}} + \omega_0^2\mathbf{x}] = -e\mathbf{E}(\mathbf{x}, t) \tag{2.15}$$

where m is the effective mass of the electron and γ measures the phenomenological damping force which can be related to the average time between collisions in the free electron gas τ through $\gamma = 1/\tau$. For an incident light wave, the driving electric field will vary in time with frequency ω as $e^{-i\omega t}$. This means that the dipole moment contribution for a single electron is given by:

$$\mathbf{p} = -e\mathbf{x} = \frac{e^2\mathbf{E}}{m(\omega_0^2 - \omega^2 - i\omega\gamma)}\,. \tag{2.16}$$

This can then be extended to the full material by allowing for N molecules per unit volume with Z electrons per molecule. We also want to allow for the different electrons in the molecule to have different binding frequencies, so we say that there are f_j electrons per molecule with damping constant γ_j and binging frequency ω_j. This makes our macroscopic polarization be:

$$\mathbf{P} = \frac{Ne^2\mathbf{E}}{\epsilon_0 m}\sum_j \frac{f_i}{(\omega_j^2 - \omega^2 - i\omega\gamma_j)} \tag{2.17}$$

where the oscillator strengths f_j satisfy the sum:

$$\sum_j f_j = Z\,.$$

We can then combine equation 2.17 with equations (2.9) and (2.10) to give:

$$\epsilon_r(\omega) = 1 + \frac{Ne^2}{\epsilon_0 m}\sum_j \frac{f_i}{(\omega_j^2 - \omega^2 - i\omega\gamma_j)} \tag{2.18}$$

which is a general form for the Lorentz model of a material which incorporates multiple resonances. This model can give an accurate description of the the dielectric constant if suitable definitions of f_j, γ_j, and ω_j are used. This can be useful for applications such as finite-difference time-domain (FDTD) modeling which require accurate constants to produce accurate results. If we impose a few constraints, a simplified form can be obtained which is useful for simple analytic equations and can, in general, still produce good results. These calculations can then be checked later with the more complex model for the dielectric constant if desired. We first remove the contribution of the bound electrons represented by ω_0 and also assume the electrons are all the same, which removes the summation. This gives us the following approximation of the dielectric function:

$$\epsilon_r(\omega) = 1 - \frac{\omega_p^2}{\omega^2 + i\gamma\omega} \tag{2.19}$$

where ω_p is called the plasma frequency and is defined as:

$$\omega_p^2 = \frac{Ne^2}{\epsilon_o m}\,. \tag{2.20}$$

This is a form of the Drude model[51] and incorporates the plasma frequency ω_p which represents the frequency regime where the metal transitions from dielectric behavior to metallic behavior. The dielectric function here has both real and imaginary components which can be split apart by $\epsilon_r(\omega) = \epsilon_1(\omega) + i\epsilon_2(\omega)$ giving:

$$\epsilon_1(\omega) = 1 - \frac{\omega_p^2\tau^2}{1 + \omega^2\tau^2} \tag{2.21}$$

$$\epsilon_2(\omega) = \frac{\omega_p^2\tau}{\omega(1 + \omega^2\tau^2)} \tag{2.22}$$

where $\gamma = 1/\tau$ has been substituted. Here $\epsilon_2(\omega)$ is related to the losses in the material and the real and imaginary components can be studied separately. Using this description of how metals interact with light, we can see how their interactions vary through different regimes and how we can leverage different phenomena to produce useful devices.

2.2 Plasmons

We now look at how the metal reacts to external fields as the frequency ω of the driving field varies with respect to the plasma frequency ω_p. At the frequencies we are interested in here generally $\omega \gg \gamma$ and so for convenience we reduce equation (2.19) to its lossless form of:

$$\epsilon_r(\omega) \approx 1 - \frac{\omega_p^2}{\omega^2} \tag{2.23}$$

to look at the regions where $\omega > \omega_p$, $\omega = \omega_p$, and $\omega < \omega_p$.

For the region where $\omega > \omega_p$, equation (2.23) will give a positive value for $\epsilon_r(w)$ and allows for waves to propagate through the metal. In this regime the metal acts like a simple dielectric.

The next region, where $\omega = \omega_p$, is more interesting and is where we are introduced to the idea of a plasmon. A plasmon is a collective oscillation of free electrons[20] which, as we will see, can be very useful. In this regime $\epsilon_r = 0$ which when coupled with equation (2.14) means that $k = 0$, and therefore must correspond to a collective longitudinal mode. This oscillation is called a volume plasmon and describes a situation were all of the electrons are moving in phase at the plasma frequency. This type of oscillation is possible in a metallic slab where one can think of all the electrons moving in-sync with respect to their positively charged ion cores. As the electrons move away from their ion cores an electric field is established inside of the slab which then creates a restoring force on the electrons. Since this oscillation is longitudinal, it does not couple with transverse electromagnetic waves making its excitation difficult and can only be accomplished by events such as a particle collision. If instead of a slab only an interface between a metal and a dielectric is assumed where the metal and dielectric extend infinitely from the interface, a surface plasmon (SP) can be generated with a resonant frequency of $\omega_{sp} = \omega_p/\sqrt{2}$.[52] Similarly, if a metallic sphere is excited, a localized surface plasmon resonance (LSPR) is generated with a resonant frequency of $\omega_{lspr} = \omega_p/\sqrt{3}$. It should be noted that the derivation of ω_{lspr} assumes that the radius r of the sphere is much

shorter than the wavelength of the incident light, or that $r \ll (2\pi c)/\omega$. In these cases the plasmons are not propagating and rather oscillate in the same location. The case of a LSPR is used to understand the interactions of light with either small pieces of metal or metal surfaces with nanoscale features. If a surface has a small metallic protrusion, it is possible to generate a LSPR at that point and has the potential to generate extremely high field enhancements.

The final region we will look at is where $\omega < \omega_p$. Here the wavevector k becomes complex and the wave equation, equation (2.14), no longer propagates but rather decays exponentially into the metal. This is called an evanescent wave. In this regime light is usually simply reflected by the surface (as we are used to with metals and why they are used as mirrors), but since the wavevector has an imaginary component it opens up the door to many possibilities. The wavevector of light is restricted by the relationship $k^2 = k_x^2 + k_y^2 + k_z^2 = n^2\omega^2/c^2 = 4\pi^2 n^2/\lambda^2$ and thus so is its confinement. It is not possible for the z, y, or z components to increase arbitrarily since they are bound by the total k and explains why a free-space electromagnetic wave cannot be confined to a volume smaller than the Rayleigh resolution limit which is $\approx \lambda/(2n)$. This is also the underpinnings for the diffraction limit of an optical microscope, since the wave is not able to carry spatial information for scales less than $\approx \lambda/(2n)$. This limit can be overcome, though, if one of the components of k is imaginary, since the other components can then increase while still satisfying the equality $k^2 = k_x^2 + k_y^2 + k_z^2$. This leads us to the trade-off where if we want to get high spatial information, our waves need to have an evanescent component. Since evanescent waves decay quickly, this means that the information needs to be collected very close to the surface, since once the wave propagates to the far-field that information is lost. By using various geometries, such as the ones presented in this thesis, it is possible to tailor the use of evanescent waves combined with propagating waves to read out the nanoscale information we want.

2.2.1 Surface Plasmon Polaritons

At the interface between a metal and dielectric it is possible to form what is called a surface plasmon polariton (SPP). A polariton is a quasi-particle resulting from the coupling of an electromagnetic wave (here photon) and a electronic dipole (here a surface plasmon). So an SPP is a combination of photons coupled to the electron oscillations in a metal.[53] Figure (2.1) shows a schematic of an SPP where the wave is evanescent going into the dielectric ($+z$ direction) as well as going into the metal ($-z$ direction) and propagates along the surface in the $+x$ direction.

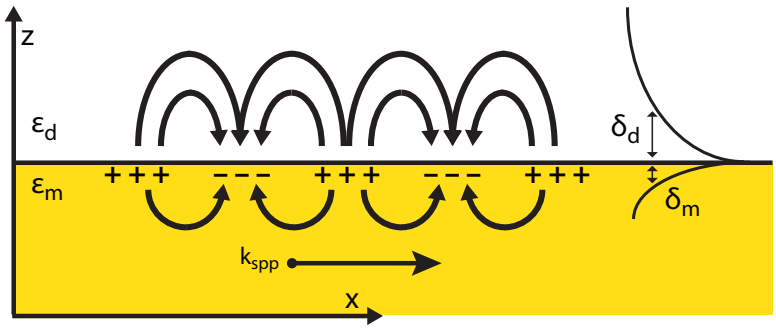

Figure 2.1: **Surface plasmon polariton** An SPP is an electromagnetic wave which is bound to, and propagates along the interface of a metal and dielectric. The field is evanescent in the $+z$ and $-z$ directions and the field penetrates into the metal and dielectric with decay lengths of δ_m and δ_d.

Solving the wave equation for the boundary conditions of the metal and dielectric and assuming the wave propagates in the x direction, the dispersion relation $k_x(\omega)$ for an SPP can be found to be:

$$k_x(\omega) = k_{spp}(\omega) = \frac{\omega}{c}\sqrt{\frac{\epsilon_m \epsilon_d}{\epsilon_m + \epsilon_d}} \tag{2.24}$$

where ϵ_m is the dielectric constant of the metal in ϵ_d is the dielectric constant of the surrounding medium. We now will restrict ourself slightly to cases where ω and ϵ_d are real. Also, after splitting ϵ_m into its real and imaginary components $\epsilon_m = \epsilon'_m + \epsilon''_m$,

we restrict ourself to cases where $|\epsilon'_m| > \epsilon''_m$, $\epsilon'_m < 0$, and $|\epsilon'_m| > \epsilon_d$. This allows us to obtain a complex $k_{spp} = k'_{spp} + ik''_{spp}$ where:

$$k'_{spp} = \frac{\omega}{c}\left(\frac{\epsilon'_m \epsilon_d}{\epsilon'_m + \epsilon_d}\right)^{1/2} \tag{2.25}$$

$$k''_{spp} = \frac{\omega}{c}\left(\frac{\epsilon'_m \epsilon_d}{\epsilon'_m + \epsilon_d}\right)^{3/2} \frac{\epsilon''_m}{2(\epsilon'_m)^2}\,. \tag{2.26}$$

If we look at the imaginary component which is responsible for the dissipation of the energy in the wave, mostly though ohmic damping, we can see that the wave intensity decreases as $e^{-2k''_{spp}x}$ making the propagation length to be $L_{ohmic} = (2k''_{spp})^{-1}$. For $\lambda =$ 514.5 nm at a silver/air interface $L_{ohmic} \approx 22\mu m$.[53] The field also decays exponentially normal to the surface as $e^{-|k_{z,m}||z|}$ in the metal and $e^{-|k_{z,d}||z|}$ in the dielectric, from which we can get the depth at which the field falls to $1/e$, often called the penetration depth, in the dielectric and the metal to be:

$$\frac{1}{\delta_m} = \frac{\omega}{c}\sqrt{\frac{-\epsilon_m^2}{\epsilon_m + \epsilon_d}} \tag{2.27}$$

$$\frac{1}{\delta_d} = \frac{\omega}{c}\sqrt{\frac{-\epsilon_d^2}{\epsilon_m + \epsilon_d}} \tag{2.28}$$

which at $\lambda = 600nm$ for a silver/air interface gives $\delta_d \approx 390nm$ and $\delta_m \approx 24nm$.[53] This also clearly shows that the maximum energy is at the interface.

Examining the dispersion relationship in equation (2.24) we can see that it is different from the dispersion of a normal beam propagating through air. This difference is shown graphically in figure (2.2). For a beam of light to couple into an SPP both the energy and momentum components must be the same. Since the "light-line" and SPP line never cross in figure (2.2) it is not possible to couple free-space light directly into SPPs, and something more complex needs to happen for an SPP to be generated. One possible solution is to have a thin sheet of metal with air on one side and a higher dielectric material on the other. This is often referred to as the Kreteshmann configuration. Since the dispersion relationship in the higher dielectric material is different than in air [as

depicted by the blue line in figure (2.2)], there is a place where light traveling in the higher dielectric material matches the energy and momentum conditions of an SPP on the metal-air interface. If the film is thin enough, the light meeting the conditions on one side can generate SPPs on the other surface of the metal. A second way to get the added momentum needed to generate an SPP from free-space light is with the use of a grating. We know that when light is incident on a grating momentum along the plane of the grating is added to some modes of the incident beam. If this added momentum equals the momentum needed to generate the SPP [as shown by the purple line in figure (2.2)] then both conditions are met and an SPP can be generated. The special properties of SPPs make them useful in many applications. For example, since the wave is evanescent in one direction it is possible to focus the energy of the beam down further than would be possible with a propagating beam. Also, since the generation of plasmons only occurs when certain conditions are met, it is possible to make a sensor which can determine when parts of the system, such as the index of refraction of the dielectric are varied.

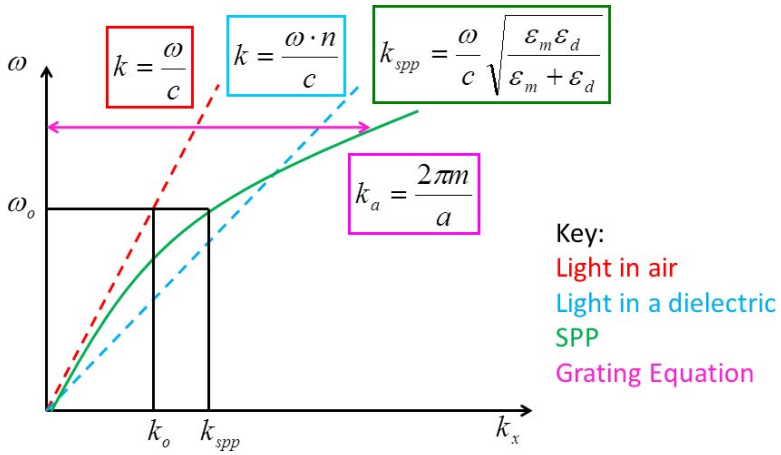

Figure 2.2: **Dispersion relationship of surface plasmon polaritons** The dispersion relationship of three different waves are plotted; a plane wave in free-space, a plane wave traveling through a dielectric medium with an index of refraction of n, and an SPP. To couple from free-space light to an SPP both the momentum and energy conditions need to be matched. One coupling method uses extra momentum imparted by a grating and the equation is given.

Chapter 3

Ultrasmooth Patterned Metals Formed via Template Stripping

The manipulation of light at the nano scale, mediated by plasmons, has been shown to have many important applications. Many of these applications require metals to be precisely machined at the nano level. One of the great benefits of SPPs is that they are very tightly confined to the surface of the metal. This confinement means that the SPPs are very sensitive to small variations at the interface, which make them good as sensors, but also means their supporting structures need to be carefully fabricated with nanometric precision. On the surface this doesn't seem like a problem, since nanofabrication techniques developed largely by the semiconductor industry have progressed significantly and have refined techniques for working at such scales, but the polycrystalline nature of the metals which need to be used, gold and silver, cause problems.

These metals, when deposited, exhibit a roughness on the order of a few nanometers. This roughness is enough to hinder the propagation of SPPs and quality of a LSPR. Additionally, most applications for these devices require the metals to have patterns on them. The most common methods of creating patterns, e-beam lithography and focused ion beam lithography (FIB), are both serial techniques and don't scale well to create

large-area devices. Also, when using FIB milling, gallium ions are implanted into the metal which reduces its ability to support plasmons.

In this chapter I present a method which was developed to overcome these challenges and the work done to extend the method for use in various applications.

The following contains work that has been produced though a collaborative effort, and is largely derived from the following publications:

1. Lindquist, N. C., Johnson, T. W., Norris, D. J., and Oh, S.-H. Monolithic integration of continuously tunable plasmonic nanostructures. *Nano Letters* **11**, 3526 (2011).[3]

   Contributions: In this paper I performed much of the fabrication and characterization. I also was involved in the FDTD simulations, interpreting the results, and the writing of the final paper.

2. Olmon, R. L., Slovick, B., Johnson, T. W., Shelton, D., Oh, S.-H., Boreman, G. D., and Raschke, M. B. Optical dielectric function of gold. *Physical Review B* **86**, 235147 (2012).[9]

   Contributions: For this paper I fabricated two of the three samples and performed ellipsometry measurements on all three samples. I also gave input to the interpretation of the results and had some input in the final paper.

3.1 Introduction to Template Stripping

To create the type of ultrasmooth metal films required for many advanced plasmonic devices, a fabrication method which could produce these high quality films while still being cost-effective was needed. One method which has been gaining popularity is called template stripping. The idea of template stripping was first introduced by Hegner *et al.* and consists of using an ultra-flat substrate, such as mica, as a mold for the metal to be deposited on and then later removed.[54] This method only produced flat films, but the

method was extended by Nagpal *et al.* using patterned silicon as a mold.[55] This allows for patterns to be created in the ultrasmooth films. The use of silicon as the mold is helpful for two reasons. First, the nobel metals we use have excellent wetting on and poor adhesion to silicon. This combination allows for the metals to follow the contours of the template almost perfectly, and still be easily stripped off. Second, a typical silicon wafer is single-crystalline which allows for very smooth surfaces and also makes it easy to pattern. Also, extensive research into the precise nanofabrication of silicon has been done by the semiconductor industry. Using this method many different types of patterns have been formed. An example of a template-stripped vs. non-template-stripped film is shown in Figure (3.1) where the difference in roughness is clearly visible.

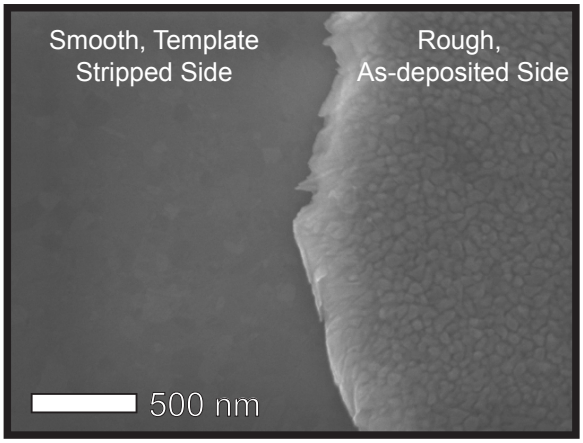

Figure 3.1: **Template-stripped vs. As-deposited Au.** An SEM of the two sides of a 200 nm thick Au film. The left side shows the template-stripped, ultrasmooth interface which was in contact with the mold while the right side shows the as-deposited, rough surface.

3.2 Monolithic Integration of Continuously Tunable Plasmonic Nanostructures

Here we extend the method of template stripping to integrate complex three-dimensional shapes with precisely controlled geometries above, below, and through an optically thick metallic film. Using a silicon template we are able to perform high-fidelity replication and monolithic integration of bumps, grooves, and apertures. The template we create is also reusable, enabling multiple copies of the metal film to be created and only requiring a simple metal evaporation to make a new copy. We also show precise control over the size of our features and are able to tune our groove depth and bump height down to the 1-2 nm length scale. Such fine control is essential, since even these small changes can cause significant differences in the optical properties of the device.

3.2.1 Fabrication

The method used to fabricate these structures is shown in Figure (3.2). First, a single-crystalline silicon wafer is patterned using a FIB to make a master template [Figure (3.2a)]. Three types of features were integrated together, and each require a different patterns in the template. To create a bump in the final product, a small groove in the mold was patterned where the length of the mill determines the height of the final bump and can be precisely controlled. To create a hole a similar process is used, but a much deeper hole ($\approx$ 300 nm) is milled. This allows for the material deposited at the bottom of the mold to be disconnected from the rest of the film and left in the mold during template stripping, creating the hole. Finally, to create a groove, ion-beam-induced metal deposition[56] was performed to selectively deposit small amounts of platinum on the silicon surface to create a bump which will be replicated as a groove in the final product. To protect the platinum from the metal later deposited on the mold, a thin 11 nm thick later of silica was deposited on the mold in an atomic layer deposition chamber before metal deposition.

After creation of the mold, a thin layer of metal was deposited on the template through electron-beam induced evaporation [Figure (3.2b)]. For this step it is important to use a deposition technique with directionality so that the holes are formed well. If a conformal deposition technique (such as evaporation with a planetary fixture or some sputtering methods) is used the metal at the bottom of the hole will not be disconnected from the bulk of the film and thus a hole will not be formed. Next, we want to access the ultrasmooth, pristine metal at the interface between the metal and the template.[57] To do this a layer of UV curable epoxy is applied to the film [Figure (3.2c)], cured, and then used to pull the film away from the template [Figure (3.2d)]. This produces the ultrasmooth metal patterned with holes, grooves, and bumps.

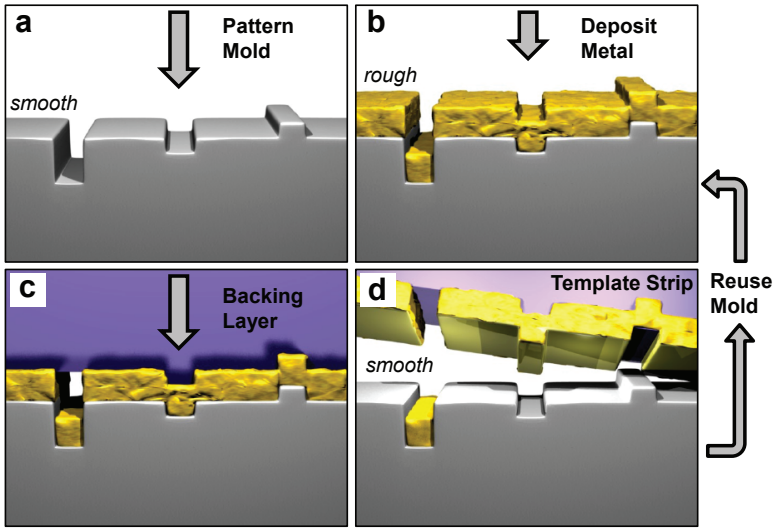

Figure 3.2: **Processing schematic.** (a) The silicon mold is patterned with trenches, grooves, and bumps. (b) Metal is deposited onto the mold and (c) an epoxy backing layer is applied to the film. Finally, (d) the film is peeled away from the mold revealing the ultrasmooth metallic surface patterned with holes, bumps, and grooves. Figure from Lindquist et al.[3]

3.2.2 Ramped Gratings

To exemplify the quality of the devices able to be produced, various test structures were fabricated and characterized. The first example demonstrates the integration of convex and concave structures along with the precision afforded by this method. A mold was make using both FIB milling at the previously mentions ion-beam-induced deposition to create a grating structure where the elements in the gratings are different heights, as seen in Figure (3.3a). This template has both elements extending from and extending into the surface of the mold. After template stripping there are bumps created from the grooves in the mold and grooves created from the bumps on the mold, shown in Figure (3.3b). Figures (3.3c-d) show that the produced structures are smooth and well defined.

Gratings with a ramped height for both a bump structure [Figure (3.5a)] and groove structure were fabricated and characterized through both SEM and atomic-force microscopy (AFM). The ramped bump grating has features which vary in height linearly from 10 to 120 nm, with a periodicity of 520 nm while the bump width also varies from 210 nm to 270 nm. Similarly, the ramped groove grating has features which vary in depth from 20 to 100 nm, with a periodicity of 530 nm while the groove width varies from 180 to 290 nm. AFM scans of the gratings are shown in Figure (3.4) from which the precise height differences can be seen exemplifying the level of control possible from line to line of 1 – 2 nm.

To measure the plasmon generation efficiency of our gratings, we used an inverted microscope (Nikon Eclipse) with a 5x 0.15 NA objective coupled to an imaging spectrometer (Newport MS257) with a cooled CCD camera (CoolSNAP HQ^2) all controlled with custom LabVIEW^{TM} software. In this configuration we are able to measure the spectral reflectivity as a function of the bump height [Figure (3.5b)] or groove depth [Figure (3.5c)] in a single measurement. In these graphs the vertical axis represents space while the horizontal axis represents wavelength. The measured data are taken

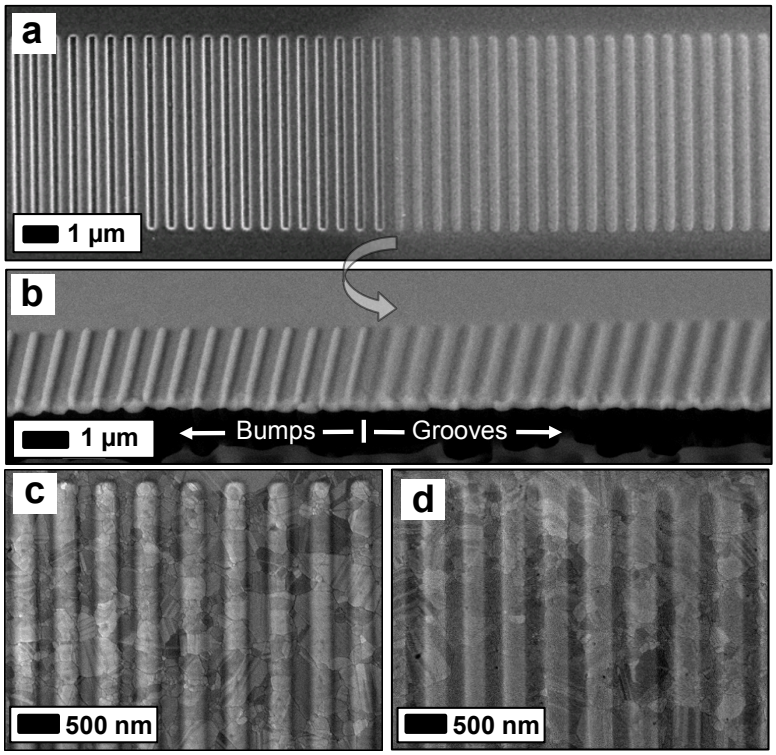

Figure 3.3: **Template-stripped bumps and grooves.** (a) SEM image of a silicon template containing both grooves and bumps created by both milling into the surface or depositing platinum with the FIB. (b) A cross-section of the template-stripped film corresponding to the mold shown in (a). It can be seen that the grooves turn into bumps and the bumps to grooves. (c) Zoomed images of the template-stripped silver bumps and (d) grooves show smooth, well-defined features. Figure partially adapted from Lindquist et al.[3]

with the incident polarization oriented perpendicular to the grating lines to generate surface plasmons and normalized to the reflection when the light is polarized parallel to the gratings lines. The sharp dip in the reflectivity and its movement as the bump height or groove depth changes indicates that generation of plasmons is strong function of bump height and groove depth. Our samples show that the minimum in reflectivity occurred at a bump height of 60 nm and a groove depth of about 60 nm. The width of the reflectivity dip for the bumps is 10 nm. Normally we would expect that as our

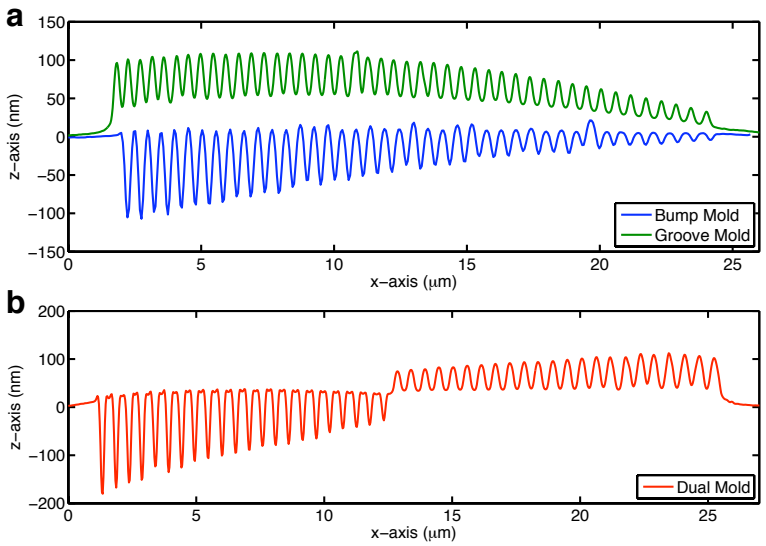

Figure 3.4: **AFM characterization of molds.** (a) AFM scans of the fabricated silicon mold used to create the ramped bump and groove grating. (b) AFM scan of the mold for a ramped grating containing both bumps and grooves. From these scans the heights of the bumps and depths of the grooves can be measured. Figure from Lindquist et al.[3]

grooves got deeper we would see a red shift. Here though, we see a minimal shift since the width of the groove is also increasing which will blue shift the resonance. Figure (3.5d) shows spectra for a single bump height and groove depth extracted from Figures (3.5b-c). It is seen that for these devices the reflection minimum for a metallic bump grating (537 nm) is to the blue of that for the groove grating (580 nm). These results show good correlation to the reflectivity spectra simulated by finite-difference time-domain (FDTD) simulations. Further simulations were performed on a ramped grating and are shown in Figure (3.5e). Here we can see that there is a bump height which is optimal for surface plasmon generation at this wavelength and the optical energy is more strongly localized in one section of the grating. This control of optical energy placement may be useful for various plasmonic applications such as photovoltaics,[36] photon sorting,[58] and trapped rainbows.[59,60]

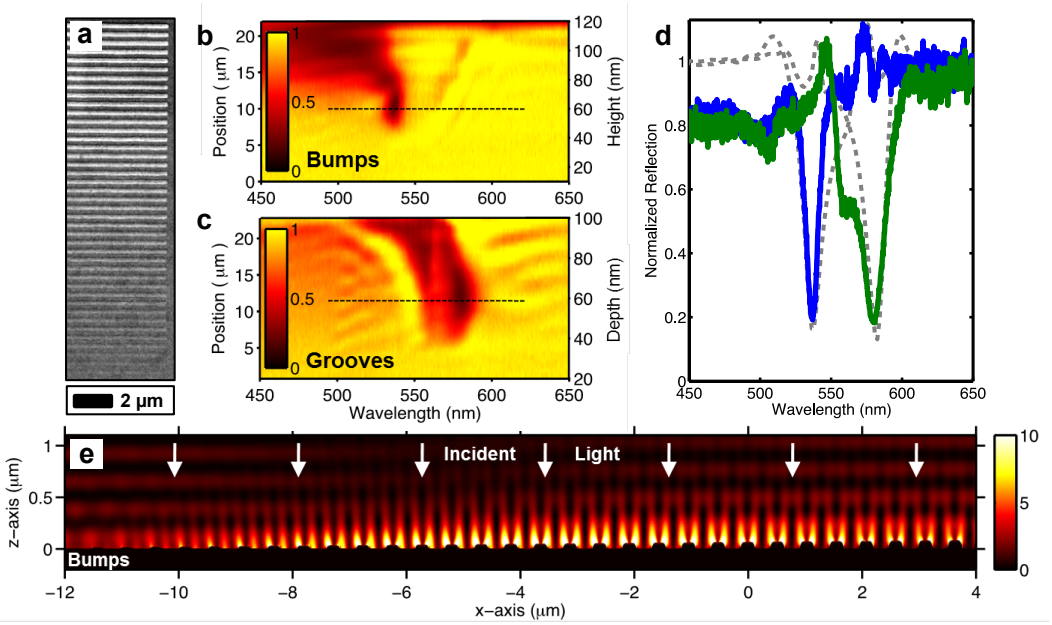

Figure 3.5: **Measurements and simulations of ramped gratings.** (a) SEM of a ramped grating. (b) Reflection map for the bump and (c) groove grating. The vertical axis represents different locations along the ramped gratings and the horizontal axis represents spectra. The dark regions represent areas where surface plasmons are being generated. (d) Cross-section spectra from the horizontal dashed lines in (b-c) showing sharp reflectivity minimums. These results are compared with FDTD simulations. (e) Field map plot of the time-averaged electric field around a ramped bump grating. It can be seen that the plasmons are most efficiently generated for bump heights in the middle, showing the optimal height for plasmon generation at this wavelength. Figure from Lindquist et al.[3]

Gratings were also fabricated with bumps of a constant height to demonstrate the high-quality of resonances possible with this method. Gratings where fabricated with a period of 690 nm and bump heights of about 20 nm [Figure (3.6b)], 30 nm [Figure (3.6c)], 40 nm [Figure (3.6d)], and 50 nm [Figure (3.6a)]. In each grating there were 50 bumps which were 20 μm long giving the grating a size of about 20 μm by 43 μm. Reflection spectra were taken from each of the gratings and the results are show in Figure (3.6a). It can be seen that the spectra are much sharper than the ones obtained

from the ramped grating. This is because the measurements from the ramped grating always contained many slightly varying heights, each height wanting to contribute a slightly different spectra. The reflection spectra have a full-width half-max (FWHM) line-width of about 2.2 nm for the bumps 20 nm tall and about 3.2 nm for the bumps 30 nm tall. These ultra-sharp resonances indicate that there is minimal damping within the gratings fabricated by this method.

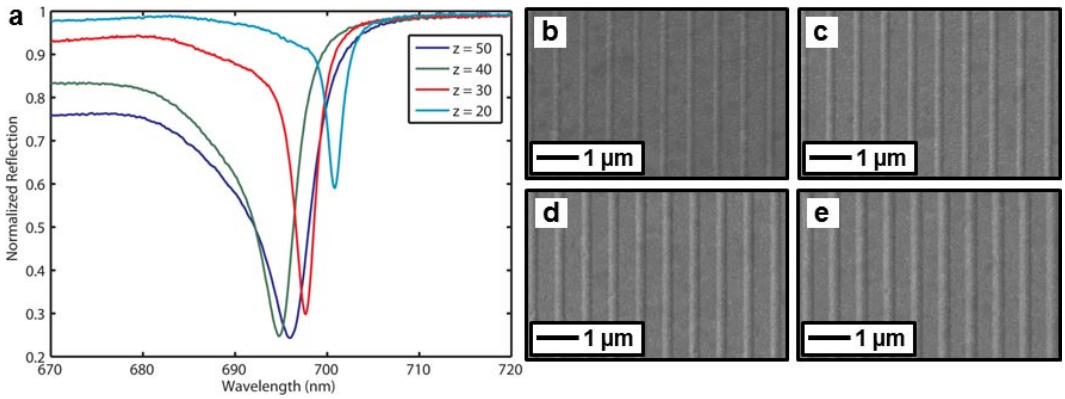

Figure 3.6: **Constant height gratings.** (a) Reflection spectra measured from gratings fabricated with a constant bump height. The gratings all had a period of about 690 nm. SEMs of the gratings are shown for the bump heights of (b) 20 nm, (c) 30 nm, (d) 40 nm, and (e) 50 nm. The reflection spectra from gratings with a bump height of 20 nm and 30 nm had line-widths of 2.2 and 3.2 nm respectively. These ultra-sharp resonances demonstrate the high-quality of these devices.

3.2.3 Fabrication of Integrated Structures

Another type of device we are able to template strip contains apertures decorated with various plasmonic elements. The forming of apertures through a 30 nm thick Ag film[55] has been shown previously, but here we use a 100 nm thick Ag film which is optically opaque, making is suitable for plasmon-enhanced transmission experiments. To create clean apertures it is important that the hole made in the mold is deeper than the thickness of the deposited film and has vertical sidewalls, as shown in Figure (3.2a). To

create vertical sidewalls with FIB milling, a 25 nm thick titanium layer was temporarily added to the mold before milling and removed before the final metal deposition. Figures (3.7a-b) show a checkerboard device creating an array of alternating bumps and apertures. The optical transmission spectra of this array, a similar array with the bumps and aperture exchanged, and an array of only bumps are shown in Figure (3.7c). From these spectra it is clear that a bump can contribute to the excitation of SPPs to create extraordinary optical transmission[61] (EOT) through the metal film.

Bull's eye structures are a common plasmonic element and contain a series of concentric rings which work together to generate plasmons and focus them to the center.[62] Here we make a bull's eye structure with an aperture added in the middle [Figures (3.7d-e)]. This geometry combination generates plasmons with the bull's eye structure to focus the energy towards and through the aperture. It is useful to note that this entire structure was made from a single mold and no additional milling was needed. This allows for the features to be perfectly aligned, rather than trying to re-align between sequential patterning steps. The transmission spectra of this structure is in Figure (3.7f) and is compared to the transmission from only a single aperture. It can be seen that the addition of the concentric rings greatly enhance the transmission.

Another benefit of this method is that patterns on both sides of the metallic film can be created which are perfectly aligned. Such alignment can be useful when structures are wanted on both sides to help couple light both into the film on one side and back in to free-space on the other side.[62] This alignment is shown in Figure (3.8a) through the cross-section of a grating. Also, a comparison can be seen between the template-stripped, smooth side in Figure (3.8b), and the other, rough side in Figure (3.8c).

To characterize and engineer many devices, it is important to gain free access to both sides of the metallic film. Here we show a method to enable template stripping in situ with the use of a sharp tungsten needle micromanipulator and is demonstrated in Figure (3.9). This method enables an engineer to use a series of copy, cut, move, rotate, and paste functions to create the desired structure. Inside the FIB chamber a sharp

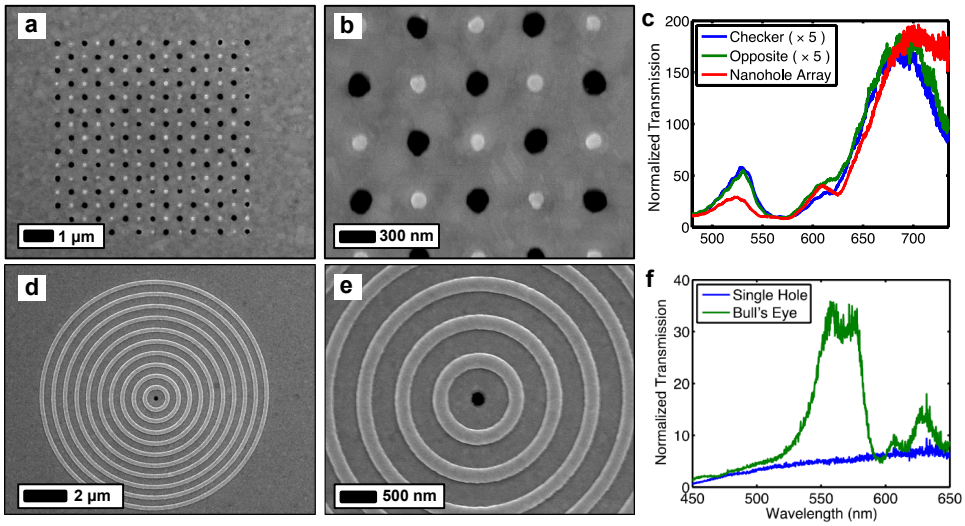

Figure 3.7: **Template stripping integrated structures.** (a)-(b) SEM images of a structure containing both bumps and apertures alternating along a 2-D grid replicated in a 100 nm thick silver film. The difference in the final features is determined by the depth of the FIB-milled features as shown in Figure (3.2). (c) The transmission spectra of the structure shown in (a)-(b) matches with that of the opposite polarity structure (bumps and apertures exchanged) as well as a structure with only holes. This indicates that the bumps can generate the grating-coupled surface plasmons responsible for enhanced optical transmission. (d-e) A bull's eye structure fabricated with concentric rings around a single aperture which (f) increases the transmission greatly when compared to an isolated hole. Figure partially adapted from Lindquist et al.[3]

tungsten needle is welded onto our 300 nm thick silver film which is still on its silicon template. The FIB-induced platinum deposition[56] weld is strong enough to template strip a 30 μm long strip [Figures (3.9a-c)] which can then be rotated, translated, imaged, and set back down in situ. This method is similar to the preparation of transmission electron microscope (TEM) samples, allowing a thin sample to be obtained, but doesn't require many of the laborious steps usually involved such as deep cuts, polishing, and thinning. With this method TEM preparation which can often take many hours can instead be completed in a fraction of the time.

This same method can be used to template strip patterned films such as those shown

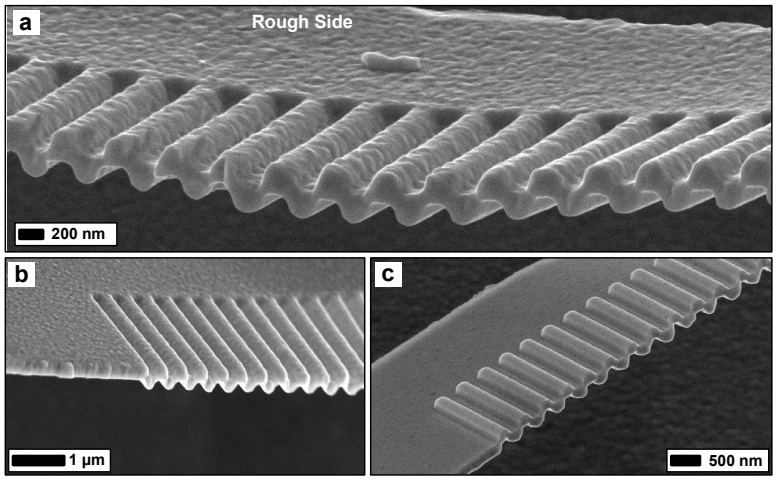

Figure 3.8: **Cross-section of metallic gratings.** (a) Cross-sectional SEM image of a metallic grating exemplifying the alignment between the two sides of the film. (b) SEM of the smooth side of a template-stripped film and (c) SEM of the rough side of the film. Figure partially adapted from Lindquist et al.[3]

in Figures (3.9d-f). Once removed the films can be extensively manipulated with precision. This process offers tremendous flexibility in sample preparation, manipulation, and characterization, allowing detailed inspection and precise three-dimensional placement of smooth, patterned metallic films.

3.3 Optical dielectric function of gold

Using template stripping to create films changes the morphology of the metal, which in turn changes the optical dielectric function of it. It has been shown that the dielectric functions of silver can vary greatly depending on how it is deposited.[63] There is also a great disparity between the constants published in literature for both silver[64,65] and gold.[64–69] Having accurate dielectric functions is important for successful nano-optical device engineering. To better understand the effect of surface texture we measured the dielectric function from three different samples and compared them to results from

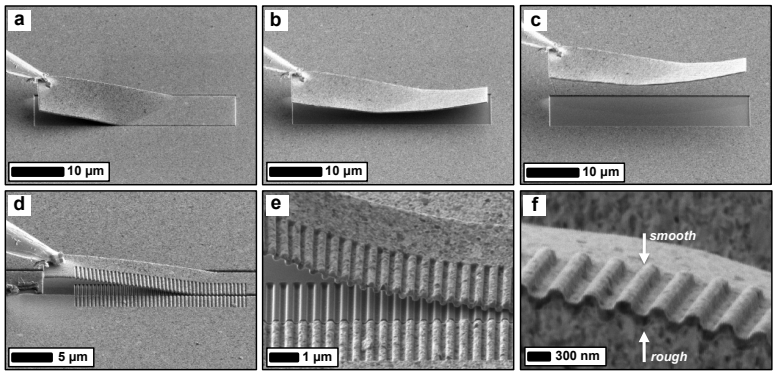

Figure 3.9: **In situ template stripping.** (a)-(c) Time-series SEM images demonstrating the removal of a 30 μm long strip of 300 nm thick silver inside a FIB chamber. Once removed the strip can be relocated and placed back on the surface. (d) SEM image of a grating being removed and (e) a close-up of film being removed. (f) A suspended metallic film after removal indicating both the smooth and rough sides of the film. This film can then be relocated or imaged and characterized further. Figure partially adapted from Lindquist et al.[3]

literature.

The first sample measured was a single-crystal Au(111) disk (SC, thickness 1 mm, diameter 10 mm, MaTecK GmbH), the second was a 200 nm thick Au film deposited on a soda-lime glass substrate (EV), and the third was a 200 nm thick Au template-stripped (TS) film deposited at the same time as the evaporated film, but template stripped from a flat silicon mold. The evaporation was done in an electron-beam evaporator (CHA Industries SEC600) with a base pressure of 2×10^{-6} torr. A deposition rate of 0.1 Å/s was used for the first 25 nm and increased to 1 Å/s for the rest. For the template-stripped sample a drop of optical epoxy (Norland 61) was placed on the gold surface after the evaporation. The epoxy was then cured under a UV lamp for 15 min. and put on a hot plate at 50°c for for 12 hr. The film was them peeled away from the mold with no additional post-annealing performed.

The surface topography of the each of the three samples is shown Figure 3.10 and measured by dynamic atomic force microscopy (AFM, Innova, Bruker). Each sample

was rinsed with isopropanol and dried with N_2 before being scanned. The measured root mean square (rms) roughnesses are R_{RMS} = 1.12 nm for the SC sample, 1.26 nm for the EV sample, and 0.25 nm for the TS sample. The SC sample lacks crystal grain boundaries, but still exhibits roughness from its polishing process. The grain size of the EV and TS samples is similar at about 10 - 70 nm. This would be expected since they were created in the same deposition and no additional annealing steps were performed. It has previously been shown that the the grain size of a template-stripped film can be increased without increasing the surface roughness though an annealing step while the film is still on the silicon mold.[55] While the grain size was similar between the EV and TS samples, there was a significant reduction in roughness for the TS sample which would be expected from the template stripping process.

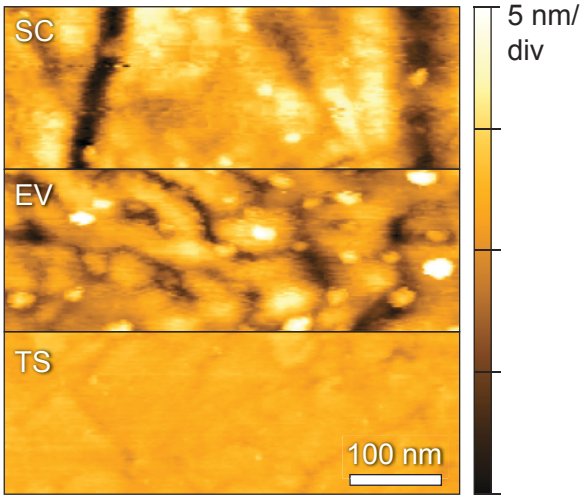

Figure 3.10: **Topography of samples measured by an AFM.** (a) Single-crystalline gold (SC), (b) evaporated gold (EV), and (c) template-stripped gold (TS). The template-stripped surface shows significantly less roughness when compared to the others. Figure from Olmon et al.[9]

After the samples were prepared, their dielectric functions were measured via spectroscopic ellipsometry. Ellipsometry measures the complex reflection ratio (ρ) which is

determined from the complex reflection coefficients for the s- (r_s) and p- (r_p) polarizations of light incident on the surfaces at an oblique angle θ_i which is generally picked to be close the the Brewster angle to maximize their difference. The value of ρ can also be written in terms of the amplitude ratio ($\tan\psi$) and phase difference ($\Delta = \phi_p - \phi_s$) of the two complex reflection coefficients giving the equation:

$$\rho = \frac{\phi_p}{\phi_s} = (\tan\psi)e^{i\Delta}. \tag{3.1}$$

These values can then be used to determine the values of n and k of the system at each wavelength investigated.[70]

Measurements were performed on two variable angle spectroscopic ellipsometers (VASE and IR-VASE, J. A. Woollam) with a rotating analyzer in the visible and a rotating compensator in the IR. The measurements were made at three angles of incidence, $\theta_i = 65°, 70°$, and $80°$ over a range of 300 nm – 2 μm in the visible and 1.25 μm – 25 μm in the IR. The overlapping region was used to check the consistency between machines and showed good agreement. The data were also checked through taking measurements in the visible regime using instruments from two different laboratories. They showed a standard deviation of less than 0.18 and 0.15 for ϵ_1 and ϵ_2 over the visible range.

Figure (3.11) shows the real (ϵ_1) and imaginary (ϵ_2) parts of the measured dielectric functions in the visible range of the evaporated, template-stripped, and evaporated samples. Also shown for comparison are data obtained from literature. Data from Johnson and Christy,[64] Théye,[66] Schulz,[68,69] Weaver,[67] and Blanchard et al.[71] are plotted as symbols. Data from the IR range can be see in the original publication.[9]

In the visible spectral range shown in Figure (3.11), it can be seen that our measured dielectric function data falls within the range of measurements from literature. The three samples we choose to measure show slight variations due to their significantly different topographies, but don't show the large variations shown in some of the other measured dielectric functions from literature. The large apparent variations in the different values

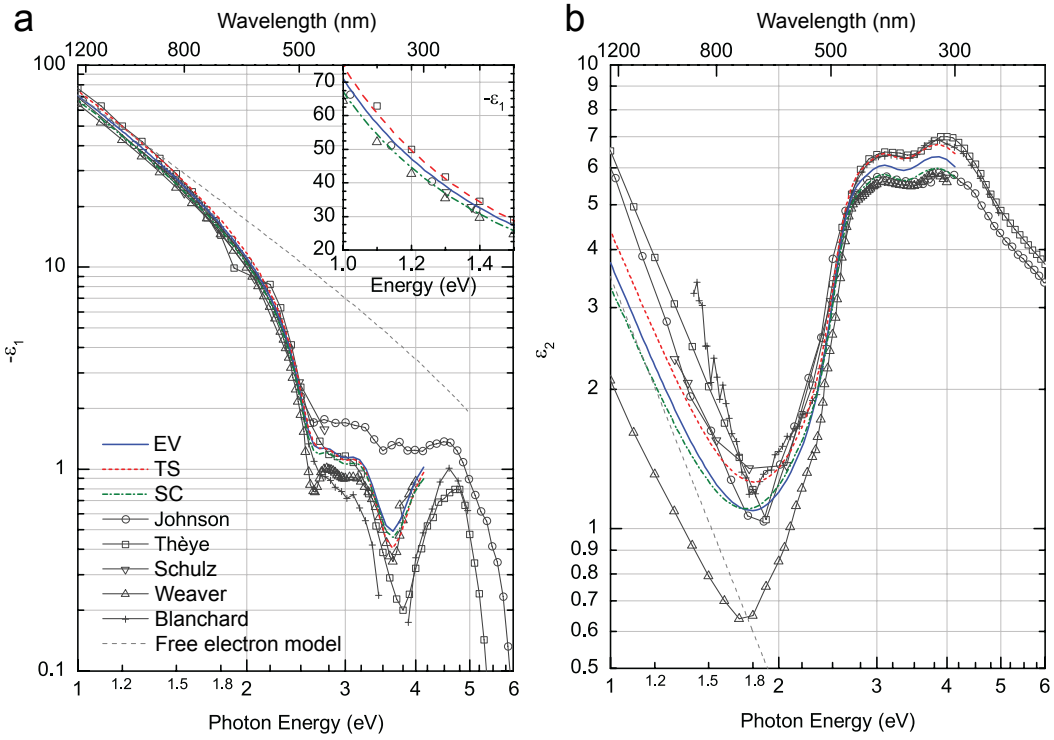

Figure 3.11: **Measured dielectric functions of gold.** The measured (a) negative real part ($-\epsilon_1$), and (b) imaginary part (ϵ_2) of the dielectric function in the visible range from the evaporated (EV), template-stripped (TS), and single-crystal (SC) samples. Various other dielectric functions found in literature are also plotted including date from Johnson and Christy,[64] Théye,[66] Schulz,[68,69] Weaver,[67] and Blanchard et al.[71] for comparison. Figure adapted from Olmon et al.[9]

reported in literature have previously been thought to be due to sample morphology and preparation. Our investigation, though, shows these to have minimal effect and it is more likely that the variations are due to systematic errors and too coarse assumptions underlying some of the more indirect procedures applied which led to the deduction of incorrect dielectric functions. Here, though, we also show that the dielectric function can be slightly effected by attributes such as sample morphology and that if precise values need to be know, they should be measured on-demand.

Chapter 4

Nanofocusing

In Chapter 3 we saw that metal nanostructures enable the control of light at the nanoscale. This control gives the ability to squeeze optical energy down to volumes much smaller than what can be done through conventional optics due to the diffraction limit and is called nanofocusing.[21,72,73] Nanofocusing can create very high local field enhancements which many applications can benefit from such as super-resolution optical microscopy,[74] surface-enhanced spectroscopy,[25,75] optical trapping,[76–79] non-linear optics,[80–83] and heat-assisted magnetic recording.[39,84,85] There have been many theoretical investigations into a variety of geometries for efficient nanofocusing[86–88] and experimentally demonstrated for geometries such as sharp metallic tips,[73,89,90] wedges,[72] and nanogaps.[12,91–94]

One of the most useful of these structures is the sharp metallic tip since they can be easily integrated into scanning probe systems and used for nanoscale imaging and spectroscopy.[8,74,95] There have been many types of metallic tips used for nanofocusing created through an array of methods such as electrochemical etching,[80,96] coating of optical fibers,[80,97] attaching metallic nanoparticles to optical fibers,[98–101] and FIB milling.[89,102]

Each of these methods have their own benefits and difficulties. The major problems

are the low yield and unreadability of methods such as electrochemical etching and coating of optical fibers and the extensive effort needed for attaching metallic nanoparticles to optical fibers and FIB milling. This chapter describes two different nanofocusing schemes which make use of the template stripping method described in Chapter 3. Both methods start with smooth pyramidal molds created through anisotropic KOH etching, a method previously demonstrated,[55] but refined here significantly. Starting from the base mold, the first method makes use of placing the mold at an angle during metal deposition to create an asymmetry between two facets of the pyramid. This allows for efficient coupling of free-space light incident below the pyramid to plasmons on the top side which propagate to the tip. Using this a 100-fold increase in Raman signal is seen. The second method makes use of FIB milling after metal deposition, but prior to removal from the mold, to create a C-shaped aperture around the tip of the pyramid. This aperture allows for light to couple from the backside to the topside of the pyramid and focus light at the tip. The intensity enhancement at the tip using this method is estimated from FDTD simulations to be >500x. These new methods for nanofocusing show high quality results while maintaining a high yield and ease of fabrication and will enable more exploration in the field.

The following contains work that has been produced though a collaborative effort, and is largely derived from the following publications:

1. Cherukulappurath, S., Johnson, T. W., Lindquist, N. C., & Oh, S.-H. Template-stripped asymmetric metallic pyramids for tunable plasmonic nanofocusing. *Nano Letters* **13**, 5635-5641 (2013).[17]

   Contributions: For this paper I conceptualized the idea and developed the entire process. I also performed all of the SEM imaging along with some of the optical characterization. I also performed all of the FDTD simulations, interpreted the results, and helped write the paper.

2. Lindquist, N. C., Johnson, T. W., Nagpal, P., Norris, D. J., & Oh, S.-H. Plasmonic

nanofocusing with a metallic pyramid and an integrated C-shaped aperture. *Scientic Reports* **3**, 1857 (2013).[10]

Contributions: For this paper I was involved in the conceptual design and performed part of the process development and fabrication. I also performed all SEM characterization and helped with the optical characterization. I was involved in interpreting the results and the writing of the paper.

3. Lindquist, N.C., Jose, J., Cherukulappurath, S., Chen, X., Johnson, T. W., & Oh, S.-H. Tip-based plasmonics: squeezing light with metallic nanoprobes. *Laser & Photonics Reviews* **7**, 453-477 (2013).[14]

   Contributions: For this paper I was involved in some of the writing (all of the HAMR section, plus parts of others) and helped with the final editing.

4.1 Theoretical Background

4.1.1 MIM Plasmons

Nanoscale metallic tips all exhibit local field enhancement due to an electrostatic optical "lightning rod" effect, but plasmonic nanofocusing harness the power of the collective oscillations of electrons to enhance the field even further. In Chapter 2 the surface plasmon polariton (SPP) at a single interface was introduced. The equation for single interface SPP is given in Equation (2.24) along with its skin depth into the metal [Equation (2.27)] and dielectric [Equation (2.28)]. These waves are confined in one dimension, perpendicular to the surface of the metal. It is also possible to squeeze SPPs down to subwavelength regions in two or three dimensions by letting them propagate along structured metal surfaces such as sharp tips[86,87] or to narrow gaps.[12,91–94] When two SPPs are traveling along opposite sides of a sufficiently thin metal slab surrounded by a dielectric it creates a insulator-metal-insulator (IMI) slab.

When an SPP is propagating along an IMI slab it can have an electric field distribution with either an even or odd symmetry as seen in Figure (4.1). These correspond to when the SPPs on the top and bottom interfaces are in phase (odd-field mode) or out of phase (even-field mode). When the thickness a of the metal film is decreased to below the penetration depth δ_m into the metal the plasmons on the top and bottom surfaces will couple and create a single IMI plasmon. As the thickness of the metal decreases to nothing, the behavior of the odd- and even-field modes are quite different. The even-field mode transforms and becomes increasingly similar to free-space light. This means that in a very thin film the field will mostly be contained within the dielectric and can travel for long distances with minimal loss. Due to this property the even-field mode is often called a long-range SPP. The lack of significant losses is desirable, but the trade-off is that the mode does not allow for extreme light localization. For extreme light localization the odd-field mode is used. The dispersion relationship for the odd mode IMI SPP for k_{spp} is given by:[53,103]

$$\tanh\left(\frac{a}{2\delta_m}\right) = -\frac{\epsilon_d\,\delta_d}{\epsilon_m(\omega)\,\delta_m} \tag{4.1}$$

$$\left(\frac{1}{\delta_d}\right)^2 = \epsilon_d\left(\frac{\omega}{c}\right)^2 - k_{spp}^2 \tag{4.2}$$

$$\left(\frac{1}{\delta_m}\right)^2 = \epsilon_m\left(\frac{\omega}{c}\right)^2 - k_{spp}^2 \tag{4.3}$$

where a is the film thickness, δ_m and δ_d are the SPP field penetration depths into the metal and dielectric, and $\epsilon_m(\omega)$ and ϵ_d are the dielectric functions of the metal and dielectric. In this mode when a is decreased there is an increase in k_{spp}, and the light gets more tightly confined within the metal. A similar result can be obtain with cylindrically-symmetric geometries.[104] This is the mode which can be used for extreme light confinement, because even though there will be significant losses, the field can be squeezed into a tiny volume.

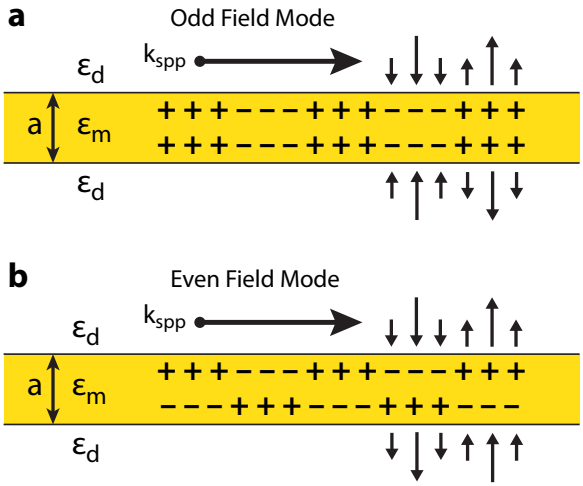

Figure 4.1: **Insulator-metal-insulator (IMI) plasmonic waveguides** with an (a) even and (b) odd field mode distribution. As the slab thickness a decreases to near the field penetration depth the plasmons on each metal-dielectric interface couple together to form a single IMI plasmon.

4.1.2 Plasmonic Nanofocusing

In order to obtain high electric fields around sharp metallic tips, they can be illuminated through a variety of methods. As can be seen in Figure (4.2), the even-field mode at the end of a metallic tip resembles free-space light and has minimal confinement, while the odd-field mode excites a localized resonance at the tip. Since the odd-mode IMI plasmon is desired at the tip, simple linearly polarized light head-on will not be sufficient since it will excite the wrong (even) mode. At the apex of the tip with the odd-mode IMI plasmon the electric field is oriented along the tip axis. It is possible to directly excite this mode though head-on illumination using a tightly focused radially-polarized beam of light,[8] with linearly polarized light at a large tilt angle,[105] or with the edges of a tightly focused Gaussian beam.[80] The proper illumination can generate a localized surface plasmon resonance (LSPR) at the tip. The exact spectra response of the LSPR depends on the tip geometry and materials. For a sharp metallic tip, high

field enhancement occurs through the excitement of the LSPR, but also thought the non-resonant electrostatic "lightning-rod" effect.

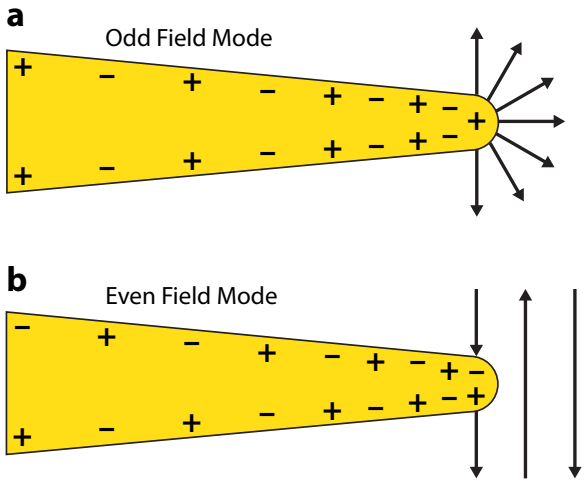

Figure 4.2: **Nanofocusing at a tip.** (a) SPPs traveling towards a metallic tip with an off field mode generate a high intensity spot at the tip while (b) SPPs traveling with an even field mode don't nanofocus since their mode matches that of free-space light.

While it is possible to directly excite the LSPR resonance at the tip, the optics required make it difficult in many situations. Another solution is to use diffraction limited optics to generate SPPs which then propagate towards the tip. As the SPPs propagate towards the tip and the thickness decreases the energy can be converted into the non-propagating LSPR at the apex.[86,87,106] This creates a significant increase in field intensity and a squeezing of the SPP wavelength at the tip. This transfer of energy from the IMI plasmon to the tip can occur through either adiabatic or non-adiabatic nanofocusing. For the adiabatic case, the tapering of the thickness of the waveguide is slow compared to the wavelength of the SPP. This method will minimize back-reflections since the mode is allowed to slowly be transformed.[86,87,107] This slow change comes at a price though. As the field gets more tightly confined within the metal, the dissipation also increases. If the taper angle is small to allow adiabatic change, the

length of the taper will become long, and the total dissipation of the SPP will increase. For the non-adiabatic case a relatively large angle is used to focus the light. Here the distance the SPP needs to travel will be shortened which will minimize losses, but also significant back-reflections may result, which will decrease the overall efficiency of the SPP conversion. By considering these competing mechanisms, an optimal taper may be possible for a specific design.[107] Other considerations may need to be taken into account also though such as how large tip angles have been shown in increase the backwards-radiation efficiency of a tip by increasing the radiative decay rate of an emitter close to the tip which lead to large fluorescence enhancements.[8]

There have been a variety of methods people have used to excite plasmons on a tip to nanofocus light. Previously mentioned are methods which only varying the illumination and include using a radially-polarized beam, illuminating at an angle, and using the edge of a Gaussian beam. Other methods use modifications to the tip itself such as using an electrochemically-etched tip with an integrated FIB milled grating. This grating can couple the free-space light into SPPs which can then travel towards the tip and focus.[89,108] It has also been shown that the use of asymmetric tips[109] or asymmetrically-patterned pyramids[110] can efficiently focus light. These methods are only a start though, and there and many different possibilities for creative advancement of the field.

4.2 Template-Stripped Asymmetric Metallic Pyramids

There are many different methods for nanofocusing light, as discussed perviously, but many require specialized illumination methods. Here a method is presented which transfers complexity from the illumination to the tip itself, allowing excitation with simple, linearly polarized light. This means that while the tips require more care in their fabrication, their use can be greatly simplified. The need for added complexity can be solved by adding asymmetry into the system. Symmetry breaking has been studied for a variety of different plasmonic structures,[111–113] but many methods require

either advanced lithography steps or individual, tip-by-tip fabrication, both of which are unpractical for high-throughput fabrication. To maximize usefulness, it is also desirable to minimize the background signal around the nanofocusing tip to increase the near-field contrast. The scheme presented here solves both of these problems with use of internally illuminated asymmetrically patterned pyramidal shells (i.e. the excitation occurs from inside the pyramid while the 'hot-spot' is generated on the outside). The asymmetry is introduced by making one facet of a pyramid optically thin and the opposing facet optically thick. When illuminated from below with linearly polarized light, plasmons are generated on the thin side and then propagate on the outside towards the tip. On the thick side, however, no optical energy can make it though the film and any resonance is eliminated. Using internal illumination, there is a significant reduction in background light levels since the samples are not directly illuminated. Using this geometry, 3D FDTD simulations show that at the apex of the pyramid light with a wavelength of 785 nm can be squeezed into a spot with a volume of λ^3 / 1,000,000. This nanofocusing is then explored experimentally though far-field optical measurements of the scattered light and angle-dependent spectral measurements of the reradiated light. Finally, the nanofocusing is confirmed through Raman spectra and second harmonic generating (SHG) images.

4.2.1 Method

An important feature of these pyramids is their ability to perform with internal illumination. The internal illumination scheme is shown in Figure (4.3a). Here light is incident onto the large opening of the pyramidal shell, through it's supporting layer, and converted into plasmons on the outside which propagate towards the apex. In order for this method to nanofocus efficiently using linearly polarized incident light at normal incidence, we break the symmetry in the thickness of the metal on opposing facets of the pyramid so that surface plasmons are only launched on one facet of the pyramid. To fabricate these pyramids, template stripping was used since it allows for the mass

fabrication of pyramids with ultra-smooth facets and sharp apexes.[8,55,114]

The fabrication process is shown in Figures (4.3b-e), and starts with fabrication of the mold. Crystal-orientation-dependent anisotropic etching of a silcon wafer was done in a 30% potassium hydroxide (KOH) and 10% isopropanol (IPA) solution at 80°C. This process exposes the {111} planes and creates square-base pyramidal pits with an opening angle of 70.52°. Next, metal was evaporated onto the mold. To create the asymmetry needed in the facets of the pyramid, the mold was placed at a fixed angle with respect to the silver source during a single-deposition step. A similar method has been used to create bowtie nanostructures.[115] Here, an angle of 15° was used with a nominal deposition thickness of 120 nm which yields facets with 35 nm and 110 nm thick silver when measured normal to the face. The metal was then template-stripped from the mold using a UV-curable optical-quality epoxy (Norland Products, NOA 61) and a glass microscope slide to produce upright silver pyramids.

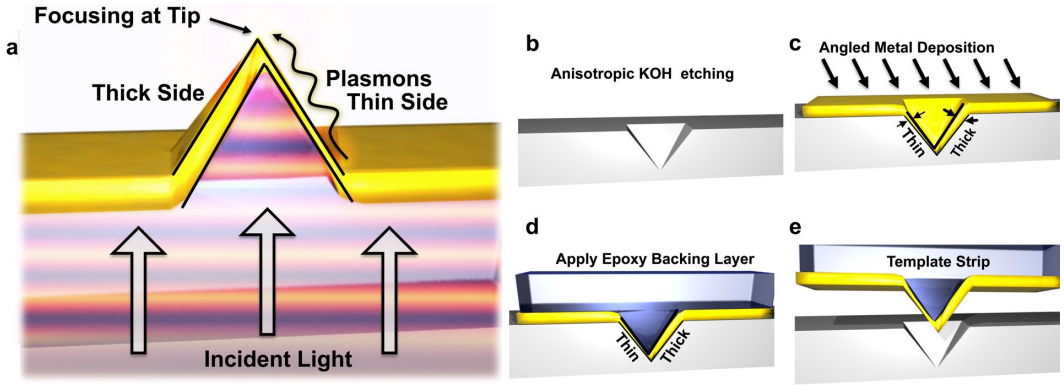

Figure 4.3: **Asymmetric pyramid fabrication.** (a) Schematic of the internal illumination nanofocusing scheme. Linearly polarized light is incident from below through a high-index dielectric (refractive index: 1.56) and plasmons are generated at the silver-air interface on the outside of the thinner facet of pyramid. Schematic of the fabrication scheme: (b) inverted pyramids are etched in the silicon mold through anisotropic etching. (c) Metal is deposited at an angle to create the asymmetry. (d) Optical epoxy is placed on the metal film and used to (e) template strip the pyramids. Figure adapted from Cherukulappurath et al.[17]

The internal asymmetry of the pyramid introduced here allows for Kretschmann-like coupling of plasmons from the inside to outside of the structure. The smooth facets created by template stripping allow the plasmons to propagate up the face of the pyramid with minimal losses. Finally, the sharp and well-defined tip creates a well-defined hotspot at the apex of the pyramid. A similar method has previously demonstrated by Garoli et al. where nanofocusing was obtained on wedges using a phase-shifting layer at the base.[116] This method requires precise alignment of the phase-shifting layer, though, and the hotspot is only generated at a single, arbitrary point along the wedge where the phase shifting layer and base of the pyramid happen to be aligned correctly. This would make it difficult to implement in most practical application such as NSOM and optical trapping where well-defined nanofocusing regions are desired. The method presented here allows for simple wafer-scale fabrication of large arrays of pyramids with well-defined hotspots. A wafer full of asymmetric pyramids is shown in Figure (4.4a) and Figure (4.4b) shows an SEM image of an array of template-stripped pyramids. To confirm the asymmetric deposition of metal, a cross-section of a single pyramid was created by FIB milling and the resulting SEM image is shown in Figure (4.4c) which displays the asymmetry.

To better understand the nanofocusing mechanisms in this system, FDTD simulations (FullWAVE, RSoft Inc.) were performed of the asymmetric pyramid structure. To reduce computational power and memory needed, only the top 1.5 μm of the pyramid where the nanofocusing occurs was simulated. The pyramid was illuminated with a square waveguide mode at the bottom of the computational area. The dispersion relationship of the dielectric function of the silver was taken into account with a Drude-Lorentz model fit to values measured experimentally via ellipsometry. The tip of the pyramid was was rounded to a 6 nm radius which is obtainable through template stripping. Figure (4.5) shows electric field maps for two different geometries of pyramids illuminated with light at 785 nm. The symmetric case is shown in Figures (4.5e-f) and shows plasmons generated on both facets and then destructively interfering at the tip,

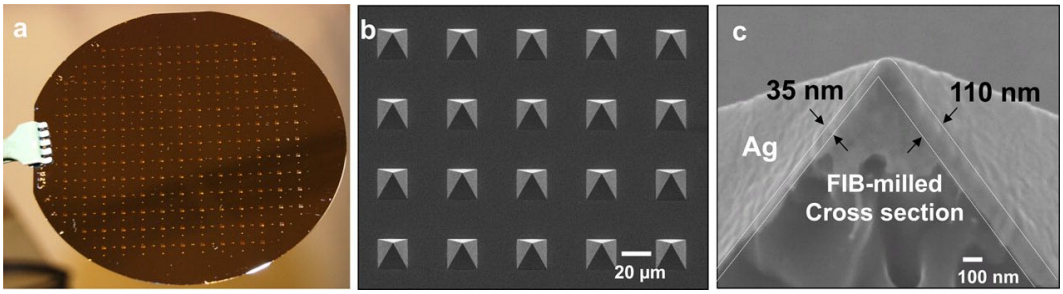

Figure 4.4: **Wafer-scale fabrication of asymmetric pyramids** (a) Photograph of a wafer full of asymmetric pyramids. (b) SEM image of an array of template-stripped silver pyramids with base widths of 20 μm. Over 1 million pyramids can be fabricated on a single wafer in parallel. (c) Cross-sectional SEM image of an asymmetric pyramid. The different in metal thickness between the two facets can be clearly seen. The porous structure of the epoxy seen here is due to melting of the epoxy during the FIB cross-sectioning. Figure from Cherukulappurath et al.[17]

thus not creating a nanofocused spot. In contrast, the asymmetric case shown in Figures (4.5a-d) only has surface plasmons on the thin facet and a strong local field at the tip is obtained. Figure (4.5) shows the electric field components in the (a) longitudinal (along the z- or tip axis) and (b) horizontal (along the x-axis) directions. A closer look around the tip corresponding to (a-b) can be see in Figures (4.5c-d). The out-of-phase plasmons causing the destructive interference for the symmetric case can be seen in Figures (4.5e-f) as the opposite polarity of the electric field on the two facets near the tip.

The coupling mechanism of free-space light to SPPs for asymmetric pyramids can be initially understood as similar to prism coupling on planar films, but the exact coupling mechanism is more complicated. The involvements of waveguide modes and reflections from the internal facets of the pyramid along with the presence of edge modes create many complicated interactions. This geometry is similar to the ones used by Bouhelier et al. for coated fibers[80] and Tanaka et al. for tetrahedral tips.[117] When the phase of the dielectric waveguide mode matches that of the SPPs, the SPPs can be directly excited in

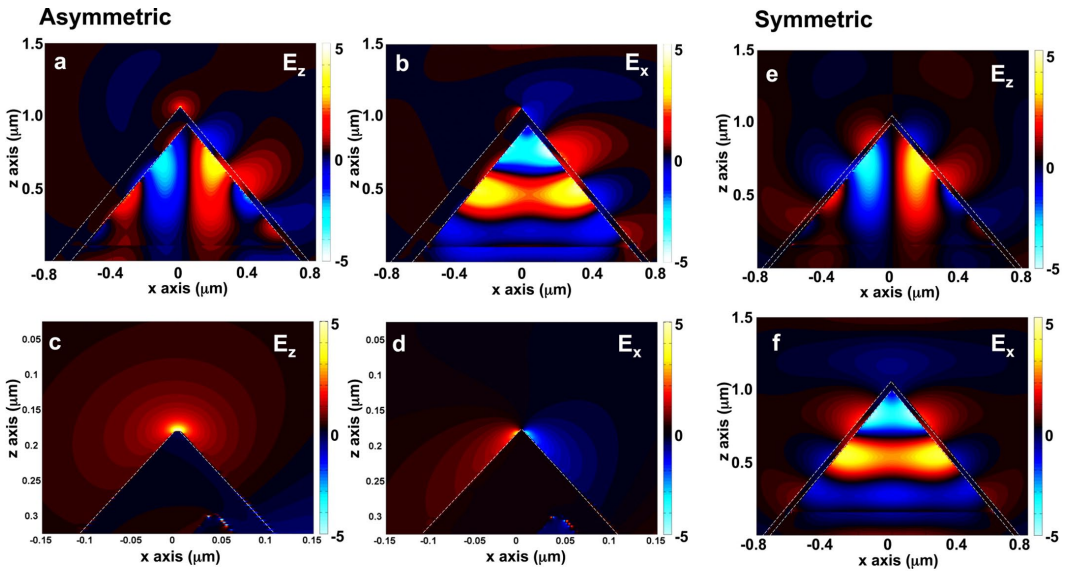

Figure 4.5: **Three-dimensional FDTD simulations** Pyramids are illuminated from below with lineally polarized light at 785 nm and the resulting electric field maps are plotted. (a) Asymmetric pyramids allow for plasmons to travel on only one side towards apex, and create a strong plasmonic field at the tip. The longitudinal (along the z-axis) field is plotted. (b) Electric field in the horizontal direction corresponding to the same condition as in (a). (c,d) Close up view near the tip of (a,b). The field enhancement around the tip in (c) is around 8. (e) Symmetric pyramids allow for plasmons to travel on both sides towards the apex. Since the lineally polarized incident light generate plasmons out of phase on the two sides, no field enhancement is seen around the tip. Electric fields along the longitudinal (z-axis) direction are shown in (e) and along the horizontal (x-axis) direction in (f). The images are saturated for clarity. Figure adapted from Cherukulappurath et al.[17]

a manner similar to Kretschmann coupling. It is also possible to get significant coupling through edge-modes as proposed by Tanaka et al.[117] For this structure it is believed this is a secondary effect though since FDTD simulations show waveguide coupling as the primary mechanism. The calculated field intensity at the apex of the asymmetric pyramid is over 60x when normalized to the incident field , which can yield thousand-fold enhancements for processes which depend on I^2 such as Raman and SHG. The field

is confined to a spot size of 12 nm (1/e of the maximum intensity) in the longitudinal direction for a tip radius of 6 nm which corresponds to a volume of λ^3 / 1,000,000.

4.2.2 Results and Discussion

Initial experiments were performed by internally illuminating the template-stripped pyramids with white light through a 50x objective (N.A. = 0.55). Since illumination was performed though a microscope objective, light will be incident from many angles. Some of the angles will efficiently couple into plasmons on the air-silver interface and create the nanofocusing. Light scattering from the tip into the far-field was collected though a 100x objective (N.A. = 0.9) and imaged onto a color charge-coupled device (CCD) (Thorlabs DCU224c). This fabrication scheme creates one thin facet and one thick facet opposite each other with the remaining two facets of equal thickness. CCD images of the light scattered by the tip are shown in Figures (4.6a-b) for (a) light polarized normal to the facets of different thicknesses and (b) light polarized normal to the facets of similar thickness. The amount of scattered light diminishes significantly for the case of similar thicknesses, implying that the scattered light from the tip is due to the asymmetric thickness of metal. The weakly scattered light from the tip in the case of the symmetric thickness could be due to any slight asymmetry in the excitation angles or a tilt in the sample or beam.

Next, measurements were taken with the same illumination and collection scheme as before, but this time using a laser at 785 nm for the source. Images of the pyramid are shown in Figures (4.6c-d) with the collection objective focused at the pyramid's (c) base and (d) tip. A bright spot is visible only at the tip, indicating that the generated plasmons travel along the facets towards the tip as expected from simulations. The output power of the scattered light from the tip was approximately 100 μW for an incident power of 10 mW at the illumination objective. This gives a total efficiency of coupling to SPPs and scattering from the tip to be around 1% for most tips. This efficiency is larger than most aperture probes and comparable to recent approaches to increase

transmission such as aperture probes leveraging extraordinary optical transmission.[118] Since this scheme exhibits low propagation losses due to the template stripped metal and reduced background signals due to the internal illumination, it should find many applications in near-field studies of single-molecule florescence and Raman scattering. Since the process can be done in parallel over a large array, it is simple to illuminate many asymmetric pyramids at once and obtain an array of hotspots. One such array is show in Figure (4.6f) where an array of 1 μm pyramids [SEM image shown in Figure (4.6e)] are all illuminated simultaneously. This array could be useful for applications such as NSOM, SERS, and optical trapping.

The coupling mechanism used here is Kretschmann-like and depends on the correct mode-coupling between the incident light and the SPP on the outside of the pyramid. What results is a sensitivity to the angle to illumination. Small changes in the angle can shift the wavelength of the light scattered from the tip. To demonstrate this the sample was illuminated internally by an adjustable condenser on an inverted microscope (Nikon Eclipse). The light was collected with the same 0.9 N.A. 100x air-objective as before. The field and condenser diaphragms of the microscope were adjusted so that the pyramid was illuminated by a mostly-collimated beam of white light. The position of the condenser was then slightly translated to vary the incidence angle on the pyramid. At different angles, spectra of the light scattered by the tip varied. Images from three different angles are shown in Figures (4.7a-c) displaying a green, orange, and red color. The spectra from three different incidence angles are shown in Figures (4.7d-f) and were taken with a deep-cooled CCD camera (Princeton Pixis 400) and an imaging spectrometer (Newport MS-257i). In this configuration it was difficult to measure the exact incidence angle, but adjustments showed a clear dependence on angle. To better understand the dependence of angle on SPP coupling, two-dimensional finite element method (FEM) simulations were performed on asymmetric wedge structures using COMSOL Multiphysics software. Here FEM was used rather than FDTD since it can better handle changes in the angle of illumination. The dependence of the wavelength

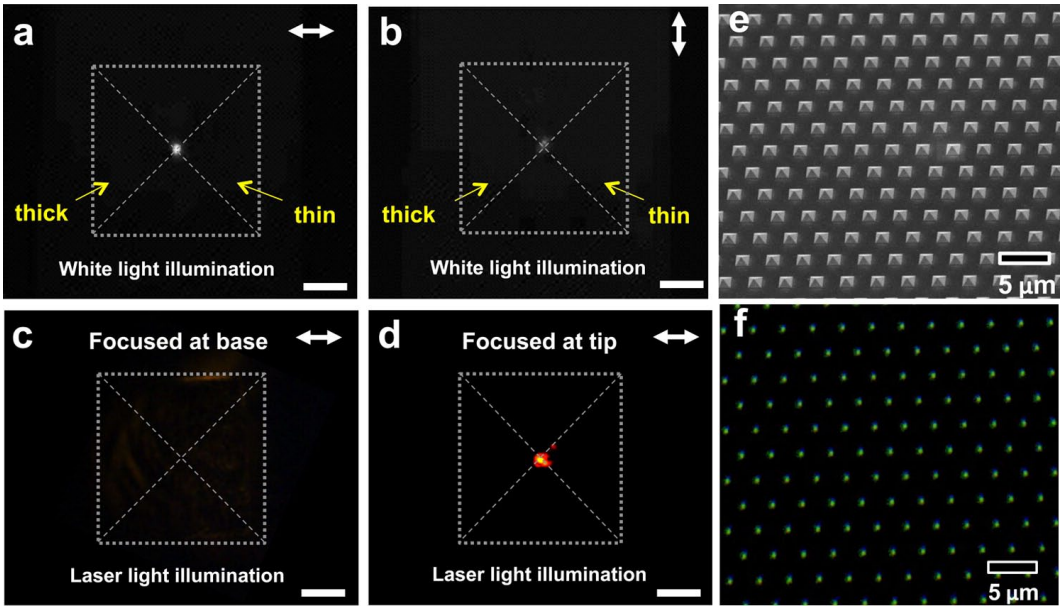

Figure 4.6: **Optical measurements of light scattered from pyramidal tips.** Microscope images of an asymmetric pyramid internally illuminated with a white light source. The position of the pyramids is represented by the white dashed lines. The polarization is normal to the asymmetric facets in (a) and to the symmetric facets in (b). Pyramids illuminated with a 785 laser are shown when (c) the base was in focus and (d) the tip was in focus. The light travels along the facets and scatters from the tip. The scale bars in (a-d) represent 5 μm. An array of template-stripped pyramids with 1 μm base widths are shown through (e) an SEM image and (f) light scattering from the tips while internally illuminated with white light. The array of hotspots demonstrate the parallel ability of this method. Figure adapted from Cherukulappurath et al.[17]

of light at the tip to incidence angle is shown in Figure (4.8a). The white dashed line represents the coupling wavelength from analytical Kretschmann coupling calculations for an infinite planar film and the close match indicates that the coupling mechanism for this wedge structure is primarily Kretschmann-like. Field intensity plots of an asymmetric wedge illuminated with 785 nm light at normal incidence and incidence tilted by 10° are displayed in Figures (4.8b,c). At the angle with the correct coupling, SPPs are excited along the facet and propagate towards the apex.

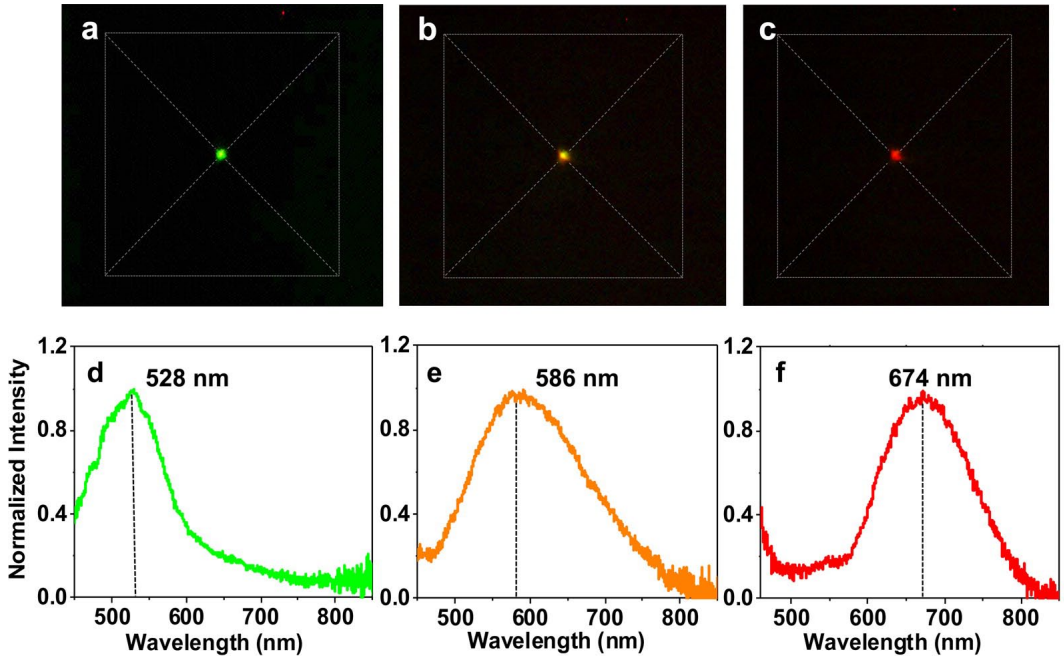

Figure 4.7: **Angle-dependent spectral tuning of light at the pyramidal tips.** Microscope images using a color CCD show that as the angle of the incident light is changed, the color scattered from the tip also changes from (a) green to (b) orange to (c) red. The corresponding spectra measured with an imaging spectrometer are shown in (d-f). Figure adapted from Cherukulappurath et al.[17]

The confined, high local field created by these asymmetric pyramids make them useful for a variety of enhanced spectroscopic processes such as SERS and SHG. To demonstrate the SERS capabilities, the silver pyramids were coated with a monolayer of benzenethiol and the Raman spectra scattered from the tip was collected. The pyramids were illuminated with a 785 nm laser diode though a 50x objective and the Raman signal was collected with a 100x objective and sent to a fiber-optic Raman spectrometer (Ocean Optics QE 65000) tuned for 785 nm though a multimode fiber. The efficiency of the internal illumination method was compared to both external illumination and illumination of a flat silver film. The geometry for internal illumination is illustrated in Figure (4.9a) and for external illumination in Figure (4.9b). The Raman spectra

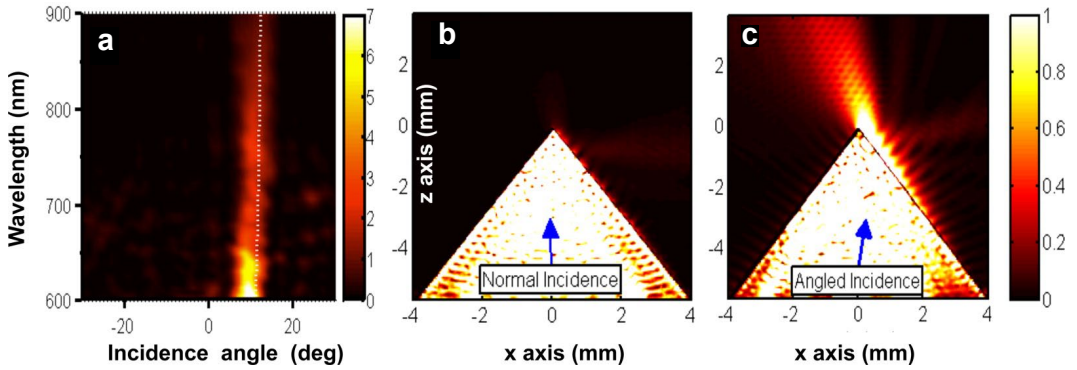

Figure 4.8: **2D FEM simulations of an asymmetric wedge.** The angle of incident light is varied. (a) Comparison of incidence angle to spectral response of light at the tip. The white dashed line corresponds to the analytical Kretschmann-coupling solution and matches well with the FEM simulations. Field intensity plots for a wedge under 785 nm (b) normal illumination show minimal focusing at the tip while (c) illumination at a 10° tilt shows significant focusing at the tip. This demonstrates the strong angular dependence of the SPP coupling. Figure adapted from Cherukulappurath et al.[17]

obtained from the internal illumination scheme is compared to the spectra from illumination of flat silver with similar conditions in Figure (4.9c). The Raman signature of benzenethiol can be seen with peaks at 1000, 1024, and 1075 cm^{-1} clearly for the internal illumination, but only a weak signal was measured from the flat silver as expected. A 100-fold increase in Raman scattering signal was measured for the tip compared to flat silver which follows the trend seen in FDTD. The spectra resulting from internal and external illumination are compared in Figure (4.9d). The internal illumination shows a stronger signal since the linearly polarized light doesn't efficiently excite plasmons on the outside of the smooth template-stripped pyramids.

Second harmonic generation (SHG) was also demonstrated on these asymmetric pyramids. A Nikon multiphoton microscope (A1 RMP+) was used for measurements with the pyramids illuminated by a femtosecond laser pulsed at a center wavelength of 800 nm though a 40x 0.5 N.A. objective. The light emitted from the tip was collected in transmission mode using the condenser on the microscope. The excitation was filtered

from the signal and the SHG signal was measured with a photomultiplier tube. A quadratic power dependence was observed which confirms that the signal is of second order. The incident light was polarized normal to the asymmetric facets and care was taken to use a power low enough to not damage the tip. The SHG image obtained from 4 pyramids is shown in Figure (4.9e) and each pyramid shows a bright spot which represents high local field intensities. An SHG image from a single pyramid is shown in Figure (4.9f). These show that the most efficient coupling occurs when the backside of the tip is illuminated.

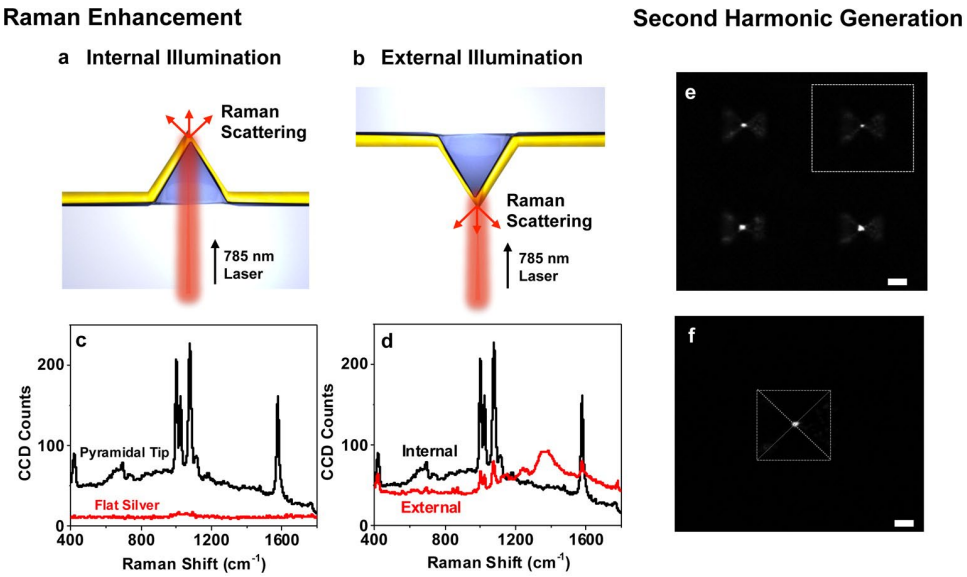

Figure 4.9: **Raman and scanning confocal SHG imaging.** Schematic of the (a) internal and (b) external illumination schemes. (c) Pyramids were coated with a monolayer of benzenethiol and the Raman signal scattered from the tip was collected with a 100x 0.9 N.A. objective. The Raman peaks for the internal illumination case are clearly visible and show much greater intensity than the signal obtained from an area of flat silver. (d) Comparison of the Raman signal collected from internal versus external illumination schemes. The Raman signal is stronger for the internal illumination scheme and also will have much less background. (e) SHG image from a scan a 4 different asymmetric pyramids. The bright spots show the 4 tips which generate SHG signals. Scale bar is 10 μm. (f) SHG image from a signal asymmetric pyramid with internal illumination. Scale bar is 5μm. Figure adapted from Cherukulappurath et al.[17]

4.2.3 Conclusion

These experimental and simulation results show that high field enhancements with a low background signal are easily obtainable for asymmetric pyramids illuminated internally. Through breaking the internal symmetry of the pyramids, SPPs can be launched on only one side of the pyramid which allows for nanofocusing with linearly polarized light at normal illumination. The method can easily create thousands of pyramids in parallel which can either be used individually or in an array. These structures are well suited for TERS and single-molecule florescence imaging with illumination through an optical fiber and will give a very high near-field contrast due to the very small background signal. While in an array these pyramids can be useful for applications such as optical trapping and plasmonic sensing, as well as high-throughput imaging applications.

4.3 Plasmonic nanofocusing with a metallic pyramid and an integrated C-shaped aperture

One possible scheme for nanofocusing with pyramids using internal illumination was presented previously, and in this section an alternate method is described. The many possible applications for nanofocusing with metallic tips mean that a variety of schemes can allow for the optimal geometry to be used for each application. As discussed before, efficient plasmonic nanofocusing at the tips of metallic pyramids requires precise control over the design and fabrication of the pyramids. Since SPPs are lossy, it is beneficial to allow the light to propagate though a low-loss dielectric material for as long as possible, so as to minimize the distance the more-lossy SPPs need to propagate. Often metallic tips for nanofocusing are patterned with FIB milling, but the surface-roughness of the as-deposited metals generally used as a base layer can be detrimental to the nanofocusing. Template stripping can solve this roughness problem and is once again used for this nanofocusing method. This method also once again uses internal illumination due to the

flexibility it gives with respect to probing geometries and also the reduced background. While internal illumination has been well established through the use of aperture NSOM tips,[119] the spatial resolution is determined by the size of the aperture. Small apertures are used, but the optical throughput decreases significantly for apertures <100 nm and the skin depth of real metals effectively increase the size of the aperture. One attempt to overcome these problems uses a tip-on-aperture design which uses a small hole to illuminate a protruding metallic tip.[120] Other hybrid designs have also been considered such as coaxial tips[121] and MIM waveguides.[93]

This method combines template stripping with precision FIB milling to create highly efficient devices. The important features provided by the template-stripped pyramids of the smooth interfaces and sharp tips are preserved and integrated with a C-shaped aperture which delivers light to the tip. Previous studies have shown that varying the shape of a subwavelength aperture can significantly change its transmission properties.[122,123] This design creates a tip-on-aperture device[102,120] with a high-transmission C-shaped aperture.[124,125] The asymmetry of the C-shaped aperture can efficiently transmit linearly polarized light and deliver it to the still-intact, sharp tip.

4.3.1 Method

Template stripping is once again used as the foundation for this fabrication scheme. The mold fabrication is the same process used in the previous section involving anisotropic etching of silicon with KOH [Figure (4.10a)]. The next step is to deposit a 200 nm thick layer of silver onto the mold, without the angular component used in the previous section [Figure (4.10b)]. While the film is still in the mold, FIB milling is performed to define patterns and holes in the film [Figure (4.10c)]. Milling at this time is beneficial since any implanted ions or FIB induced roughness on the inside of the pyramid is not critical and FIB milling through the backside of a metallic film has been shown to produce high quality cuts with less unwanted edge rounding of the aperture.[126] After defining the aperture, optical epoxy is used to attach a supporting glass microscope

slide to the pyramids [Figure (4.10d)] and the pyramids are template stripped from the mold [Figure (4.10e)]. The resulting structure is shown in Figure (4.10f) and contains an aperture surrounding the sharp tip and smooth, template-stripped surfaces, all of which were untouched by the FIB beam.

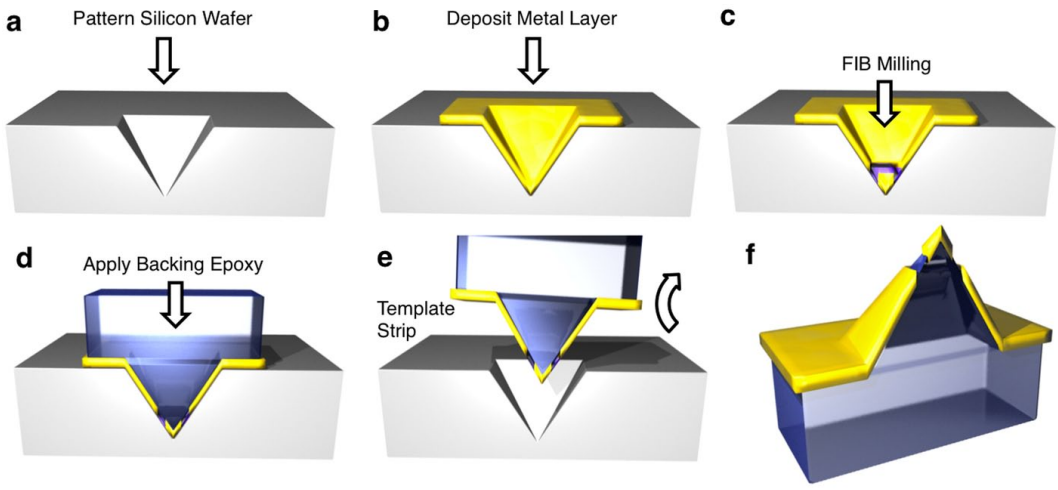

Figure 4.10: **C-shaped aperture pyramid fabrication process.** (a) A mold is made though anisotropic etching of silicon with KOH. (b) A 200 nm silver film is evaporated onto the cleaned mold. (c) FIB milling is used to define the C-shaped aperture through the backside of the metallic film. (d) Optical epoxy and a glass microscope slide are used to (e) template strip the pyramid from the mold. (f) The resulting structure keeps the sharp tip intact while also providing an efficient method for its excitation with linearly polarized light. Figure adapted from Lindquist et al.[10]

The fabricated structures are shown in Figure (4.11). From a top-view SEM image [Figure (4.11a)] the C-shape milled in the pyramid can be clearly seen. Since the C-shape is milled along the angled facets of the pyramid, the final structure has a significant three-dimensional nature which can be seen in the angled SEM images shown in Figures (4.11b,d). The C-shaped aperture has three legs, each with a width of 100 nm and covers a total area of 400-by-400 nm. As with the asymmetric pyramids, it is also possible to fabricate arrays of these structures like those shown in Figure (4.11c). Using this

same method it is also possible to fabricate the more common aperture probe like those in Figures (4.11e-f) which have 100 nm circular shaped apertures. The disadvantage with the circular aperture is that the sharp has been removed which will degrade the spatial resolution. The C-shaped aperture design allows for the tip to remain intact which allows the combination of the high transmission of the aperture just below the tip and the high field confinement possible with the sharp, metallic tip. The large taper angle (70.5°) of our pyramids also work well since it allows easy optical access of the tip and aperture from the backside of the pyramid. The large resonant transmission effects of planar C-apertures has been previously investigated,[125] and also suggested for use as near-field probes.[127] While this design resembles the planar C-aperture, the significant three-dimensional design makes it unique. In this design there is a metallic "tongue" which is lifted in the middle of the C and contains the important sharp tip. The tips itself is not fabricated by FIB or exposed to any processing. Template stripping makes it possible to have a sharp (<10 nm radius) which is free from roughness and contamination. The asymmetry needed is introduced by the three segments of the aperture and allow for efficient generation of plasmons that then propagate towards and focus at the tip.

4.3.2 Results and Discussion

To further characterize this structure, full three-dimensional FDTD simulations were performed and the results are shown in Figure (4.12). The pyramid is oriented such that the tip points along the +z axis and the tongue of the C-shaped aperture is aligned along the x-axis. Two different geometries were simulated to compare and contrast the results. The two designs are shown in the inset of Figure (4.12a) and the first is a single-slit aperture on one face of the pyramid the second is the C-shaped aperture. For reference, the coordinate axes used are portrayed in Figures (4.12a,b). To measure the spectra behaviors shown in Figure (4.12a), a pulsed input beam was used and z-component of the electric field was measured at the tip then Fourier-transformed. The

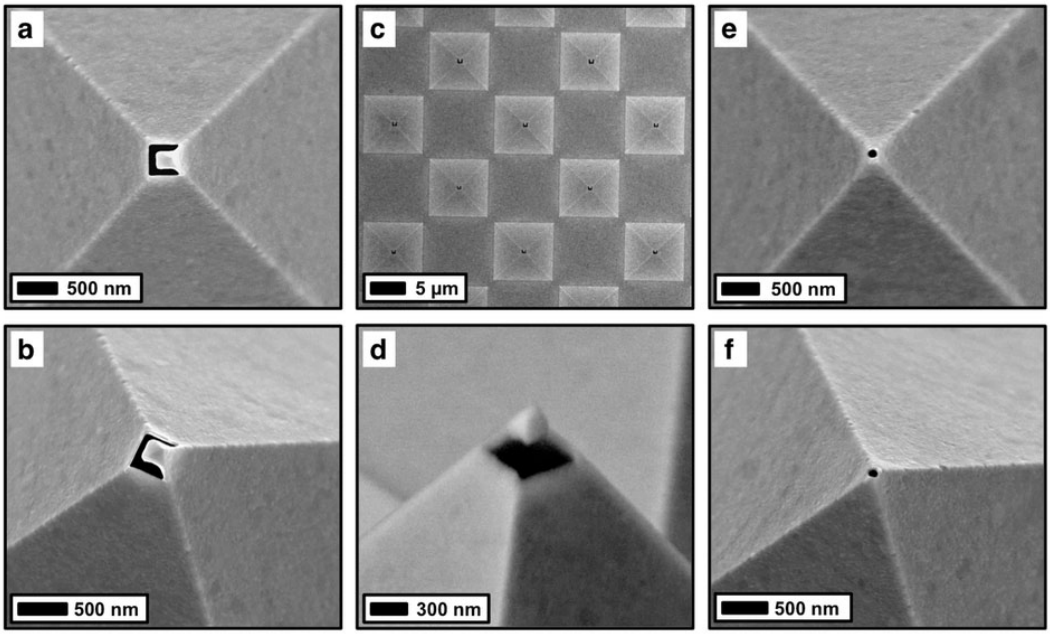

Figure 4.11: **SEM images of C-shaped aperture pyramids.** (a) Top-down SEM image of a pyramid with a C-shaped aperture patterned around the tip. (b) Angled view of the pyramid shown in (a). (c) An array of patterned pyramids. (d) Side-view SEM image showing the three-dimensional nature of the device and sharp tip. (e) SEM image of a pyramid with a circular aperture fabricated through the same method and used for comparison in measurements. (f) Angled view of the pyramid shown in (e). Figure from Lindquist et al.[10]

incident light was polarized along the x-axis. From the spectra it can be seen that both structures are capable of transmitting light and creating surface plasmons which propagate to the tip and focus, but for the case of the single slit, the field intensity is low. The C-shaped aperture, on the other hand, shows a resonance peak at 530 nm and a much higher field intensity at the tip. Cross-section field maps displaying the steady-state electric field are shown in Figures (4.12c-f). The intensity measured at the tip of a C-shaped aperture pyramid in Figure (4.12c) shows a >500x enhancement over the intensity just below the aperture inside the pyramid. The field intensity enhancement in Figure (4.12d) for a pyramid with a single slit is only 30x. This demonstrates that

while surface plasmons are generated by both patterns, the unique C-shaped slit pattern shows great improvements over the single slit. The asymmetry in the C-shape aperture is also important to allow linearly-polarized light to be transmitted and focused. Figure (4.12e) shows that when the incident light is polarized in the y-direction the plasmons generated by the two symmetric slits destructively interfere at the tip and create a null. It is also shown that changing the polarization for the case of a single slit will produce minimal transmission [Figure (4.12f)].

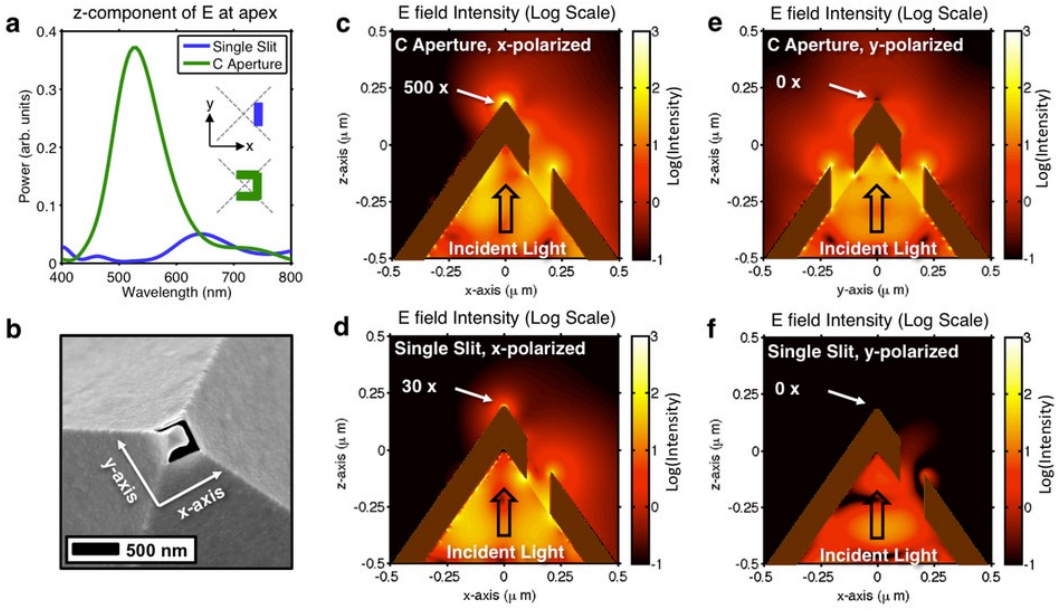

Figure 4.12: **FDTD simulations of the C-shaped aperture pyramids.** (a) Spectral response of pyramids with two different patterns, showing the z-component at the tip. The large resonant peak at 530 nm shows that the C-shaped aperture transmits much more light than the single slit. (b) SEM image of a C-shaped aperture device with the coordinate system used for the simulations. (c) Electric field intensity maps in the steady-state for a C-shaped aperture pyramid at its resonant wavelength. Illuminating with x-polarized light shows a hot spot at the tip for this device, and a much less intense hot spot for the case of a single slit seen in (d). Also, if the polarization is changed to the y-direction for the C-shaped aperture in (e) and single slit in (f), there is minimal nanofocusing at the tip. Figure from Lindquist et al.[10]

To help understand the system better we studied the structure with slits on a single face [similar to figure (4.12d)]. Pyramids were fabricated with an array of slits starting 4.5 μm from the tip measured along the face. The inside of the device before template stripping is shown in Figure (4.13a) and the final device in Figure (4.13b). The device was illuminated internally with 633 nm light and light transmitted though the pyramid was observed. In Figure (4.13c) the incident beam is polarized perpendicular to the slits and light is seen from both the slits and small spot at the tip. The spot at the tip is from plasmons which are generated by the slits then propagate towards and are scattered by the tip. When the incident beam is polarized parallel to the slits, as in Figure (4.13d), no light is seen at the apex of the pyramid showing that plasmons are not generated by the slits. Both of these results match with FDTD simulations and help verify their validity.

The behavior of the C-shaped aperture alone was also investigated. Two structures were fabricated in a similar method as the c-shaped aperture pyramids, but instead on a flat 200 nm thick silver film. Figure (4.14a) shows a fabricated hole aperture and C-shaped aperture structures on a flat film. The transmission spectra from both devices was measured and the results are shown in Figure (4.14b). The C-shaped aperture demonstrates significantly higher transmission than the hole. This comparison is similar to that of a circular aperture tip design versus our C-shaped aperture tips design. A major drawback of the circular aperture tip is the small amount of transmission, while the C-shaped aperture solves this problem.

Aperture pyramid devices are experimentally compared in Figure (4.15). First, microscope images were taken from the top of the pyramids for both illumination from the top and bottom of pyramids with circular apertures and C-shaped apertures and can be seen in Figure (4.15a). The images in 1-2 show a combination of internal and brightfield illumination and show the position of the pyramid. The images in 3-4 show only the light transmitted due to the internal illumination and it can be seen that the amount of light transmitted by the C-shaped aperture is significantly higher than the

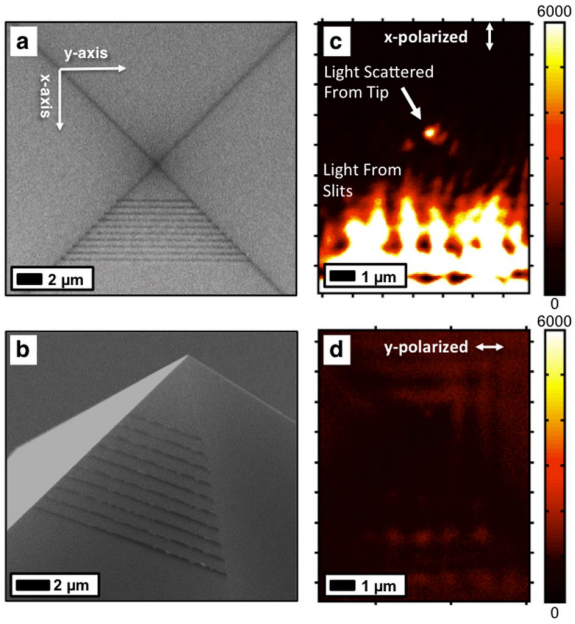

Figure 4.13: **Pyramid with slit array.** SEM images of a 200 nm thick pyramid with an integrated slit array both (a) before and (b) after template stripping. The axes shown in (a) are consistent with those in the FDTD simulations. A beam of light is incident from below the pyramid and the scattered light is observed from above with microscope. The orientation of the microscope images is same as the SEM image in (a). The light is polarized perpendicular to the slits in (c) which allows for plasmons to be generated by the slits and light is seen coming from the tip due to the scattering of the plasmons. The incident polarization is changed in (d) and minimal transmitted light is seen since plasmons are not generated. Figure from Lindquist et al.[10]

circular aperture. The spectra of the transmitted light in the far-field was also measured and is shown in Figure (4.15b). The measured spectra are an average of several devices and the spectra from the FDTD simulations are also shown as the dashed line. It can once again be seen that there is significantly more transmitted light for the C-shaped aperture than the circular aperture and that the high transmission of the C-shaped aperture is dependent on the incident polarization.

It should be noted that the measurements here do not directly measure the near-field. Instead, it is shown that the far-field measurements match with FDTD simulations

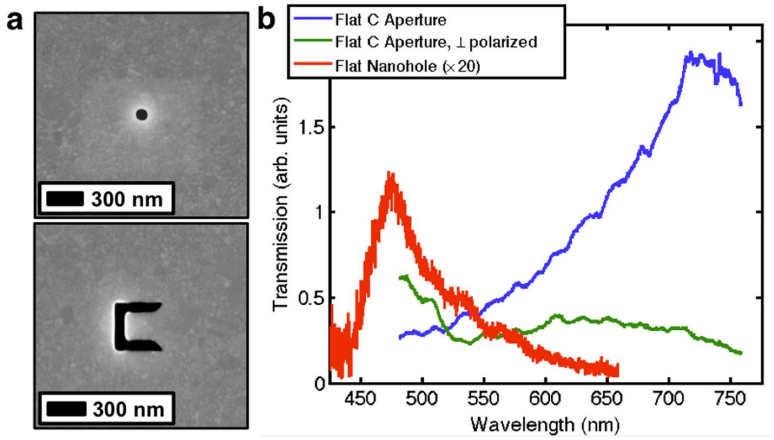

Figure 4.14: **Comparison of optical transmission through apertures on a flat film.** SEM images of a circular hole aperture and a C-shaped aperture milled in a flat 200 nm thick silver film are shown in (a). (b) The transmission spectra shows a significant increase for the C-shaped aperture compared to the circular hole. There is also a polarization dependence for the c-shaped aperture as discussed previously. Figure adapted from Lindquist et al.[10]

and then the near-field properties are elucidated via FDTD. In conclusion, we developed a new method to create a near-field probe which has many advantages. This method places a C-shaped aperture around the tip of a pyramid allowing for light to be coupled to the outside of the pyramid while minimizing background. Since the sharp tip is still intact the nanofocused spot will be very confined which should allow for high-resolution imaging. This new method should give the ability to create new probes for applications such as NSOM and TERS with improved performance and help advance the field.

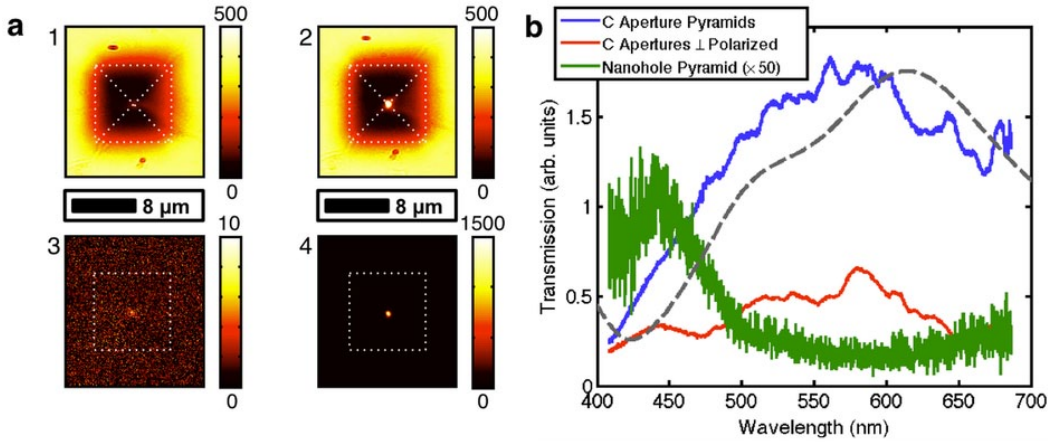

Figure 4.15: **Optical transmission spectra through pyramid apertures** (a) Microscope images of pyramids with integrated (1,3) circular and (2,4) C-shaped apertures when with (1,2) bright-field and internal illumination and (3,4) only internal illumination. The peak intensity from the C-shaped aperture is 150x brighter. (b) Transmission spectra from the pyramids shown in (a). FDTD results from the C-shaped aperture pyramid are shown by the dashed gray line. Here the peak transmission of the c-aperture is 50x more intense than the circular aperture. Figure from Lindquist et al.[10]

Chapter 5

Near-field Imaging

Using conventional optics and no prior information, an imaging system is bound by the diffraction limit which limits the maximum resolution to about $\lambda/2n$ where λ is the wavelength of the light and n is the refractive index of the material between the imaging system and the sample (e.g. air, water, or oil). This is because the waves captured by the system are only the propagating waves which have a finite maximum spatial-frequency. Increasing the resolution can be achieved through the use of the evanescent waves which contain the high-spatial-frequency components needed, but are nonradiative and bound to the surface necessitating the image be obtained very close to the surface.[74]

To glean this near-field information, often near-field optical microscopy (NSOM) is used. The system can be traced back to an idea by Synge in 1928 where he proposed a method to raster a 10 nm hole over the sample while being held only a few nanometres from the surface.[128] This idea was transformed and realized experimentally in 1972 by Ash and Nicholls for the microwave regime.[129] Then in 1984 both Lewis et al.[130] and Pohl et al.[131] demonstrated super-resolution down to $\lambda/16$ in the optical regime. Further progress was made and in 1989 Reddick et al. demonstrated NSOM as a tool to investigate light-matter interactions at the nanoscale[132] and Fischer et al. developed a single particle plasmon near-field microscope in the same year.[133] Since then many

people have continued to make modifications and improvements to various designs of NSOM systems. The basics have stayed the same and generally consist of either a sub-wavelength aperture of sharp metallic tip which is raster scanned over the sample of interest. Adding these elements can create an extremely small light source or locally scatter the near-field information into the far-field for collection by conventional optics. With the near-field information available through these methods, a wealth of information can be collected about the electronic, vibrational, structural, and dynamic properties of a sample.

When the small aperture method, commonly called aperture NSOM, is used for local illumination of the sample, the resolution is greatly dependent on the size of the aperture and the skin depth of the metal coating.[134] To obtain a higher resolution, a method called apertureless NSOM can be used which makes use of a sharp tip or particle to focus or scatter light locally.[135–137] This method can produce imaging resolutions 10x better than aperture NSOM since the resolution is determined by the tip diameter rather than an aperture. Apertureless NSOM has been proven to be a versatile method for probing the local field distribution in a variety of devices such as plasmonic waveguides and antennas,[138–140] biological membranes,[109,141] and integrated circuits.[142] This method has also proven to be versatile though its success in single-molecule fluorescence imaging[143,144] and vibrational imaging via Raman scattering.[145–147]

It is clear that NSOM imaging has many great benefits, but widespread adoption had been hampered by the low reproducibility of near-field probes. As discussed in Chapter 4, many methods have been attempted to fabricate sharp tips for nanofocusing, but each with problems. One promising method to create reproducible probes uses a colloidal metal nanoparticle on the end of a pulled fiber,[98,148] but the process of picking up the single nanoparticle is inefficient and painstaking. Additionally, the nanoparticles need to be larger than 60 nm due to quenching and limits the optical resolution. Using smaller nanoparticles places restrictions on the experiment and require the use of low-quantum-yield emitters,[149] high-index substrates,[100] or more complex probe geometries.[101]

In this chapter I show a new method for the fabrication of tips for near-field imaging. The tips are fabricated in a similar method to the ones described in Chapter 4, but here are isolated and individually template-stripped from the mold. This new method provides a procedure for the mass fabrication of high-quality, uniform, ultra-sharp metallic probes. The probes are then demonstrated in a variety of different experiments including single-molecule fluorescence, single-molecule tip-enhanced Raman spectroscopy (TERS), and fluorescence lifetime imaging. The tips are shown to perform well either matching or exceeding previous reports with other tips while maintain a usable tip yield of >95%.

The following contains work that has been produced though a collaborative effort, and is largely derived from the following publications:

1. Johnson, T. W., Lapin, Z. J., Beams, R., Lindquist, N. C., Rodrigo, S. G., Novotny, L. & Oh, S.-H. Highly reproducible near-field optical imaging with sub-20-nm resolution based on template-stripped gold pyramids. *ACS Nano* **6**, 9168-9174 (2012).[8]

   Contributions: For this paper I contributed to the initial idea and design, also I developed the fabrication process and fabricated all of the tips. I also helped interpret the results, and write the final paper.

2. Beams, R., Smith, D., Johnson, T. W., Oh, S.-H., Novotny, L., & Vamivakas, A. N. Nanoscale Fuorescence lifetime imaging of an optical antenna with a single diamond NV center. *Nano Letters* **13**, 3807-3811 (2013).[16]

   Contributions: For this paper I developed the process to fabricate and made the Ag tips. I had slight input to interpretation of the results and helped with revisions to the final paper.

5.1 Near-field imaging with highly reproducible template-stripped gold pyramids

5.1.1 Method

The fabrication of these sharp metallic tips follow a scheme similar to the one presented in Chapter 4. This method makes use of simple photolithography to define the structures and creates the nanoscale tip through a wet etching step. Generally to make devices with nanoscale features, advanced lithography tools are needed such as e-beam lithography or FIB milling. Here we instead take advantage of the anisotropic etching properties of silicon by KOH to create the nanoscale features. Similar ideas have been used in the fabrication of AFM cantilevers for quite some time, and using molds has also been pursued,[150–152] but the molds were either dissolved leaving a random dispersion of tips, or the sharp tips themselves were cut off, thus eliminating their benefit. The fabrication starts with a 100 nm Si_3N_4 thick mask on a silicon wafer. Photolithography is then used to pattern an array of 20 μm circles which are transferred into the Si_3N_4 mask through reactive ion plasma etching. The resist is then removed and the wafer is etched in KOH [Figure (5.1a)]. The exact conditions of the etch are critical to create a single point which is sharp. The conditions found to be optimal are etching for 90 min in a solution of 30% KOH saturated with isopropyl alcohol at 80°c. Gold was then deposited into the pits with an e-beam evaporator [Figure (5.1b)], and put in a hydrofluoric acid lift-off bath to remove the Si_3N_4 and unwanted gold, producing the structure shown in Figure (5.1c). The pyramids are now ready to be individually template-stripped from their mold [Figure (5.1d)]. This process starts by attaching a short piece of 15 μm diameter tungsten wire (Alfa Aesar) to one prong of a tuning fork with epoxy. The tuning fork is then mounted on 3-axis micropositioner to precisely move the wire attached to the fork. The wire is dipped into a drop of quick-setting epoxy to create a small drop on the end of the wire. The wire is then moved to, and placed in the backside of the gold pyramid in its mold. This position is kept while the epoxy sets, and then the wire is

pulled vertically, away from the mold, now with an attached pyramid. The resulting structure can be seen in Figure (5.2).

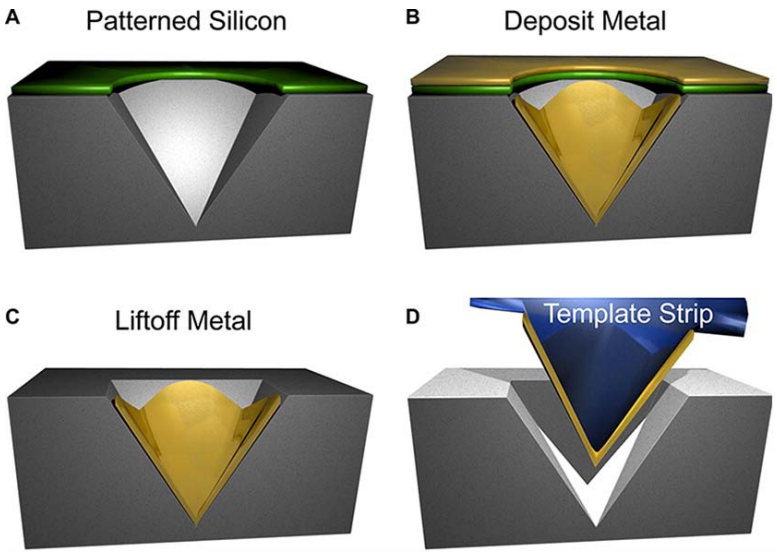

Figure 5.1: **Process schematic for sharp metallic tips.** (a) Photolithography is used to define 20 μm circles in a silicon-nitride mask (green) on silicon and subsequent KOH etching forms inverted pyramidal pits. (b) Gold is then deposited in the pit followed by (c) a lift-off step producing (d) inverted pyramids which are ready to be template stripped. Figure from Johnson et al.[8]

Since the structures are defined by a simple photolithography step, it is possible to make large arrays of devices in parallel. Figure (5.3a) shows an array of tips in a mold with a spacing of 50 μm between pyramids. With this spacing is it possible to simultaneously fabricate over 1.5 million tips on a single 4 inch wafer, each with uniform properties. A single pyramid in its mold is shown in Figure (5.3b), and a single pyramid removed from the mold and ready for use in Figure (5.3c). Through this method it is not only possible to make large quantities of pyramids, but they also have very sharp tips with about a 10 nm radius [Figure (5.3d)] which allows for high-resolution imaging.

Various other works have shown the use of gold tips fabricated by electrochemical etching or FIB milling, among others, to perform near-field fluorescence imaging[109] and

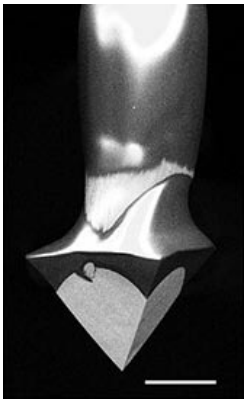

Figure 5.2: **Template-stripped pyramid on a tungsten wire.** The 20 μm base pyramids are individually glued to 15 μm diameter tungsten wire with epoxy. Scale bare 10 μm. Figure adapted from Johnson et al.[8]

near-field Raman scattering.[96,145] One major difficulty with these experiments is that the experimental results depend strongly on the particular properties of the tip. Even though all of the tips would look the same when imaged with an SEM, most of them would not produce any near-field enhancement. Because of this, experiments needed to be repeated many times through a trial-and-error approach with a yield of only about 5% and low repeatability. The performance and repeatability of the template-stripped gold pyramids presented here are quite different. Through experiments we saw a high yield of about 95% which were usable for near-field imaging and provided consistent resolution in both fluorescence and Raman.

The experimental setup used with the fabricated tip is depicted in Figure (5.4) and is a combination of a laser scanning confocal microscope and an AFM. The sample is placed on an x–y piezo scan-stage above an inverted confocal microscope and above the sample is a homebuilt AFM head which holds the gold tip. For excitation, a tightly focused radially polarized laser beam is used and the pyramid tip is positioned to be in the center of the optical focus. The tightly focused radially polarized beam provides a strong longitudinal electric field at the optical focus which excites a large electric field

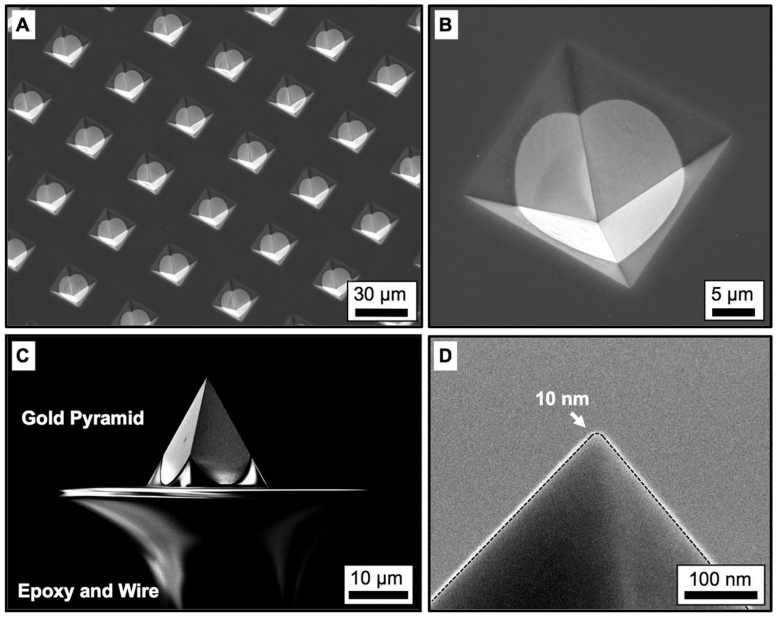

Figure 5.3: **SEM images of template-stripped tips** (a) An array of pyramids fabricated though simple photolithography allowing for 1.5 million tips to be made on a single wafer. (b) A single 200 nm thick gold tip in its mold. The mold protects the tip from contamination, allowing it to be stored for extended periods of time without degradation and the tips be removed individually on demand. (c) A pyramid removed from the mold and ready for use. (d) The radius of the tips is about 10 nm which makes high-resolution imaging possible. Figure from Johnson et al.[8]

enhancement at the pyramidal tip.[74] The sample is raster-scanned below the gold tip and the topographical information from the AFM head is collected simultaneously with the optical data from the microscope below the sample. A tip-sample distance of about 5 nm is maintained using either shear-force or dynamic normal mode feedback.[153] The photons emitted from the sample are collected through the objective, filtered, and sent to either an avalanche photo diode (APD) or a spectrometer and liquid-nitrogen cooled charge coupled device (CCD).

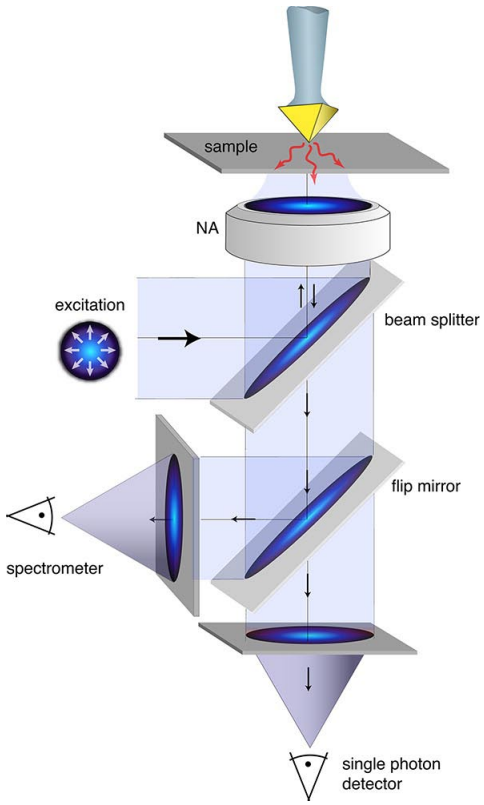

Figure 5.4: **Microscope setup used for near-field imaging.** The sample is placed on a scanning stage with an AFM on top supporting the pyramidal tip and an inverted confocal microscope below. Radially polarized light is focused with an objective to a diffraction limited spot and the pyramid tip is placed in the middle of the focus. The optical signal produced by the sample is collected through same objective and measured with a single-photon counting detector or spectrometer. Figure adapted from Johnson et al.[8]

5.1.2 Results

Near field fluorescence images of single molecules were taken to demonstrate the capabilities of the tips. Here a He–Ne laser ($\lambda = 632.8$ nm) was used to excite Atto 647N dye molecules and the collected signal is passed through a 650 nm long-pass filter to reject the excitation and then to an APD. The dye molecules were dispersed onto a

glass coverslip covered with a thin (≈2 nm) layer of polymethyl methacrylate (PMMA) to increase the photostability of the dye molecules through spin-casting of a dilute solution. An excitation power of 21 nW was used, which is very low, and allows for minimal unwanted photographing of molecules within the excitation volume and is possible due to the large fluorescent enhancements provided by the tip.

First, a confocal fluorescence imaging scan was taken without the tip [Figure (5.5a)] and it is clear that the resolution is not sufficient to identify individual molecules. The same area was then scanned with the tip in place [Figure (5.5b)] and not only are the individual molecules easily resolvable, but it is also possible to see the molecular transition dipole axis.[154] Molecules oriented in-plane exhibit a characteristic double-lobe pattern,[154] while molecules oriented along the axis of the pyramid (z-axis) show a single point. Single z-oriented molecules reveal an optical enhancement of around 200-fold and an optical resolution of 18 nm with the tip present. As the tip approaches a molecule the fluorescence rate increases and Figure (5.5c) shows the emission rate as a function of tip-sample distance of a single z-oriented molecule. The fluorescence enhancement is calculated from the ratio between the highest and lowest emission rates seen in the approach curve, after adjusting for the photoluminescence of the tip itself. This enhancement and resolution greatly exceed that shown in previous near-field fluorescence studies which use an 80 nm gold sphere for a tip and a similar sample.[98,148]

To further test the capabilities of the tips, near-field Raman imaging experiments were performed. This type of experiment has been performed before and has been shown to produce valuable chemical information about a sample. The problem, though, is that past efforts have mostly used chemically etched gold or silver tips[96,145,147] which can produce exceptionally large field enhancements, but most do not and makes the results not reproducible due to the variations in etch parameters and crystal structure of the metal wire. The pyramidal tips presented here, though, offer a repeatable solution and also makes quantitative modeling possible because of the well-defined probe geometry. To demonstrate the ability of these tips for TERS and near-field Raman

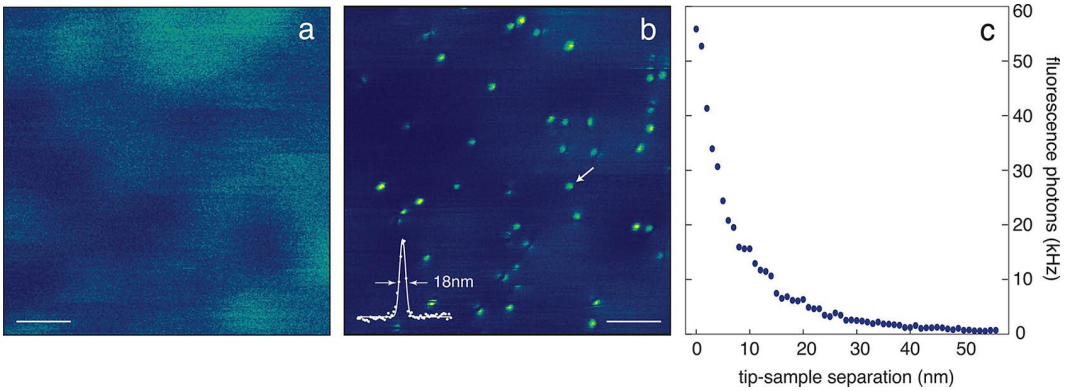

Figure 5.5: **Single-molecule fluorescence imaging of Atto 647N dye molecules.** (a) Confocal fluorescence image (contrast enhanced 5-fold) and (b) near-field fluorescence image of the same area taken with a template-stripped pyramidal probe. Scale bar: 200 nm. The full-width at half-maximum of an individual fluorescence spot in (b) is measured to be 18 nm. (c) The fluorescence rate as a function of the tip-sample distance showing an enhancement of about 200. Figure from Johnson et al.[8]

imaging, we measured a sample of carbon nanotube (CNT) bundles produced by the arc-discharge method. Since it is possible for the same tube bundle to be located and measured repeatability, this CNT sample provides a good platform to characterize the field enhancement and reproducibility of the pyramidal tips.

A near-field image of the Raman G band is shown in Figure (5.6a) for an arc-discharge CNT bundle excited with illumination at 785 nm. A cross-section taken at the white arrow shows a width of 40 nm. This 40 nm represents a convolution of the optical resolution provided by the tip with the actual non-zero width of the CNT bundle. The topographic image taken simultaneously with the near-field image is shown in Figure (5.6b) and the measured height of the CNT bundle is 6.2 nm. Spectra were taken of the CNT bundle both with the tip close to the surface and with the tip retracted and are shown in Figure (5.6c). The enhancement factor is then calculated by taking the ratio between the two spectra for a Raman band. Here the enhancement is about 10x which demonstrates that the pyramidal tips perform well in TERS experiments.

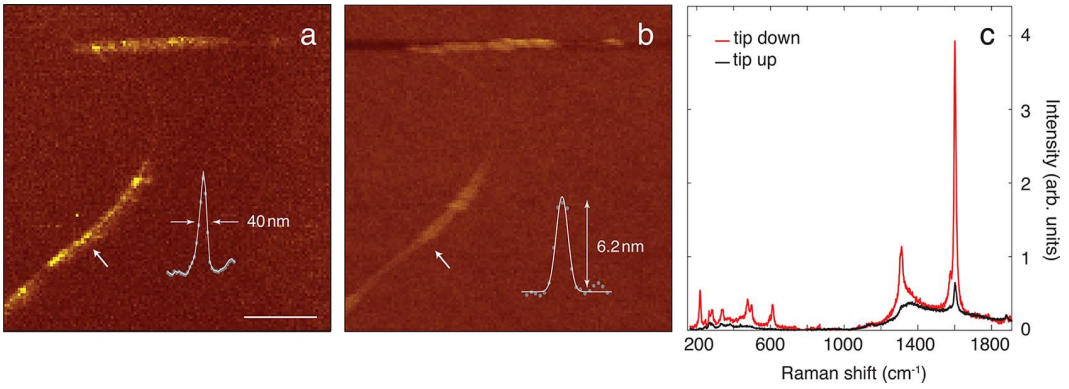

Figure 5.6: **Near-field Raman scattering from CNT bundles.** (a) Near-field Raman image of the G-band (1600 cm^{-1}) showing a CNT bundle width of 40 nm. Scale bar: 250 nm. (b) Corresponding topographic image measured along with (a) showing a CNT bundle width of 6.2 nm. (c) Collected Raman scattering spectra with and without the pyramidal tip showing an enhancement of 10. Figure from Johnson et al.[8]

5.1.3 Discussion

It may initially seem incongruent that the Raman enhancement is less than the fluorescence enhancement, but this difference can be explained by the dimensionality of the system. The single-molecules used in the fluorescence measurement are considered a zero-dimensional (0-D) object since they are essentially a point, while the CNTs used for Raman measurements are a one-dimensional (1-D) object, since it has a finite size in one dimension. Similarly if we were to measure an object evenly dispersed over a surface it would be a two-dimensional object. When a 0-D object is illuminated with confocal excitation over the area A and the near-field antenna enhances the field by a factor of f_0 in a subdiffraction area a, then the measured enhancement will be about f_0. For a the case with a 1-D object, though, the measured enhancement will be scaled by $(a/A)^{1/2} \approx 0.2$ due to the area where the confocal excitation still illuminates the CNT, but there is no enhancement due to the tip. The background is additionally increased in our CNT bundles since more than one nanotube is present in the confocal excitation

at a time. The mechanism for Raman enhancement in 1-D objects has been analyzed and discussed previously[96] and explains the perceived discrepancy in the enhancement factors presented here.

To better understand the system and the factors contributing to the large enhancements, FDTD simulations were performed for both pyramidal and conical tips with various tip angles (α) across a range of wavelengths (λ). The goal was to better understand the interactions and radiative properties of a quantum emitter when a tip is placed close to it. Experimentally the tip is illuminated by a focused high-order laser beam with an objective on the opposite side of the sample as the tip itself. This same objective is used to collect the photons emitted from the tip–sample interaction. Thus, the signal-to-noise of the system depends on the fraction of power collected by the objective which is radiating away from the tip, or in the backward direction. Any power which radiates towards the tip, in the forward direction, will predominantly couple to surface plasmons propagating along the sides of the tip.[87,155,156] This energy then is simply dissipated into heat unless a more complicated tip is used with, for example, an integrated grating to convert some of the energy in the surface plasmons to far-field radiation to be collected.[89]

The simulated configuration is shown in Figure (5.7a) and consists of a gold pyramid placed 3.75 nm above an electric dipole and the radiation patterns were evaluated. The dipole axis was oriented parallel to the tip axis and perfectly matched layers were used for all of the boundaries to avoid spurious reflections. The backward radiation (BR) efficiency was evaluated and defined as the power flux through the bottom half space ($z < 0$) normalized with the same power flux radiated by the electric dipole isolated in free-space. Thus the BR efficiency is 1 without the tip. Both conical and pyramidal tips were simulated with varying opening angles α and produced similar results, so only the data from the pyramidal tips is presented here. The simulation window was make large enough to reduce unwanted artifacts and reflections from the boundaries. Since the tip is modeled as an infinity extended object, the metal intersects the boundary which

can cause problems. To overcome this, the simulation window was made comparable to or larger than the surface plasmon propagation length. The propagation length increases with wavelength, so the simulation size needed to as well. Due to memory and processing time constraints, the window could not be made large enough so calculate the BR efficiency into near-infrared wavelengths, so only measurements out to 700 nm were made.

The results from our simulations are plotted in Figure (5.7b) and show an increase in BR efficiency for both an increase of the cone angle α and of wavelength λ. This trend comes from the fact that as the cone angle increases, the surface plasmons propagating along the sides of the pyramids become more mode-mismatched. This mode-matching has been studied extensively in other works and it has been discovered that plasmons more efficiently propagate along the shaft of a tip in the so-called adiabatic limit, which means a small α.[87] While adiabatic focusing is explained by many to be the best situation, here we see that the adiabatic limit just creates plasmons on the tip shaft which dissipate and cause energy to be lost. We see that the the backward radiation is enhanced more that a factor of 10 by varying α from 10° to 70° at a wavelength of 650 nm. This enhancement is not only due to the redistribution of the radiation pattern, but most of the enhancement is from the electromagnetic back-action, meaning the tip enhances the dipole's ability to release energy. This means that the enhanced BR efficiency corresponds to an increased radiative decay rate. The quantum emitter is prevented from complete quenching due to this increase and is part of the reason for out ability to obtain such high-quality near-field fluorescence imaging of single molecules.

5.1.4 Conclusion

Here we have presented a new method for fabricating metallic tips to be used as near-field probes. This new method is based on template stripping and allows for parallel fabrication of thousands of high-quality and high-performing tips. Additionally, the tips have been shown to very reproducible and a significant improvement over other

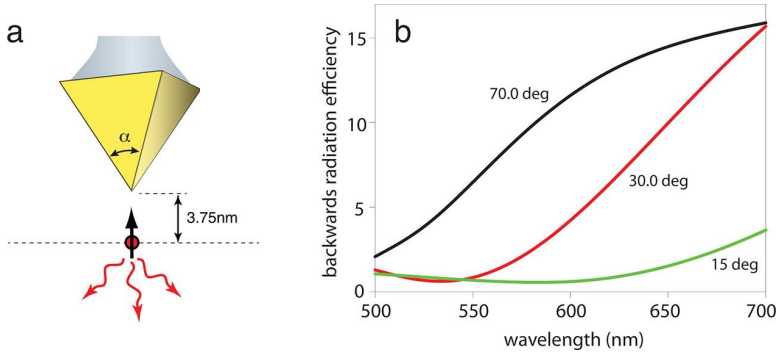

Figure 5.7: **Simulations of the backward radiation efficiency of a dipole placed in front of a pyramidal tip** (a) Schematic of the simulated area. A dipole is placed 3.75 nm from the tip of the pyramid and is oriented parallel to the tip axis. The BR efficiency is normalized to 1 for the dipole without the tip. (b) Simulation results for varying tip angle α and wavelength λ. A computational window of 2.43 x 2.43 x 1.63 μm was used with a mesh size of 2.5 nm. The results show a large increase in the BR efficiency as the tip angle α increases. Figure adapted Johnson et al.[8]

tip fabrication methods. The optimized structure provided a spatial resolution of less than 20 nm and gave fluorescence enhancements of $\approx$ 200x. They also provided good results while used for TERS imaging. The template-stripped probes presented here hold the potential to make near-field microscopy and spectroscopy a routine and reliable technique.

5.2 Nanoscale Fluorescence Lifetime Imaging of a Template Stripped Pyramid with a Single Diamond NV Center

The pyramidal tips presented in the previous section were shown to be useful, and here using a tip made in a similar manner, more advanced experiments are also shown. This experiment uses a single diamond nitrogen vacancy center (NV center) to perform nanoscale fluorescence lifetime imaging microscopy (FLIM) on the tip. The majority

of this work does not fall in the scope of this dissertation, but it is presented to show another use of the these near-field tips. The tips used for this experiment also needed a slightly different fabrication scheme. Complete details of the experiment can be found in the original publication by Beams et al.[16]

As photonic devices continue to shrink, a detailed understanding of how nanostructured environments effect the local density of optical states (LDOS) is useful. There have been numerous experiments which demonstrate the impact LDOS engineering has on the excited state decay dynamics using a variety of methods.[98,148,157–160] One method to map the LDOS is to use the excited state lifetime of an optically active material to monitor the local electromagnetic environment.[161,162] Previously groups have attempted to perform nanoscale FLIM with a single quantum system,[163,164] and here an NV center is used. Initial single emitter FLIM measurements used single molecules[148] quantum dots[158] and suffered from fluorescence bleaching and blinking, but the NV center exhibits stable photoluminescence at room temperature making is a better candidate. Here nanoscale FLIM of a pyramidal tip optical antenna is demonstrated using a single NV center.

The schematic for this experiment is presented in Figure (5.8). Here the probe (NV center) is fixed in space and the object (pyramid) is scanned over it as seen in Figure (5.8b). By monitoring the probe lifetime, an image can be created and the nanoscale LDOS created by the object can be observed. Figure (5.8c) shows the experimental setup which is similar to the setup presented in Figure (5.4), but with the addition of a third detector option for measurements of the intensity autocorrelation function. For illumination a laser with a wavelength of 532 nm was used, and since at this wavelength gold pyramidal tips don't perform well due to losses in the metal, a silver pyramidal tip was used instead. An SEM image of one of the tips used is shown as the inset in Figure (5.8c).

To fabricate the silver pyramids a different fabrication scheme than the one in Figure (5.1) was needed. The steps for KOH etching were the same, but a problem presents

itself at the lift-off step. For gold pyramids the lift-off step which removed the silicon nitride mask was done in hydrofluoric acid since gold is not etched by it. In contrast, when silver is used to make the pyramids, the hydrofluoric acid would etch away the pyramids if used in the same manner. To overcome this, the steps after the KOH etching were slightly modified. After etching the pyramids, but before the metal deposition, the wafer was placed in hydrofluoric acid to remove the silicon nitride. Since the mask used for the lift-off step has now been removed, a photoresist mask was added and patterned for the lift-off. This step required optimization since the resist needs to cover the large topographical features of 20 μm tall pyramidal pits. A thick positive resist (SPR-220) was used to cover the features and a very high exposure (8000 mJ/cm^2) was used to make sure the resist was fully exposed inside the pyramidal pits. After the photoresist was patterned the metal was deposited and the excess lifted off in an acetone bath. Using this method it is possible to create silver pyramids with many of the same benefits as the gold pyramids. Unfortunately the tips did not get quite as sharp as the gold ones and have a tip radius of about 30 nm [Figure (5.8a)] instead of the 10 nm tip radius seen with the gold tips. This difference is due to the deposition conditions used and the properties of the metals. After this publication further optimization was performed on the deposition conditions to minimize heating of the mold and the tip radius was able to be reduced to $\approx$ 10 nm for the silver tips as well.

Experimental results showing FLIM with a single NV center are shown in Figure (5.9) and study the impact of the optical antenna on the NV center's excited state dynamics. Figures Figure (5.9a,b) show the intensity and autocorrelation measurements of the single NV center with and without the silver pyramidal tip present. The tip reduces the lifetime by a factor of $\approx$ 3. Next the lifetime is recorded simultaneously with the near-field signal as the pyramidal tip is raster-scanned across the NV center which exploits the NV center's optical-transition lifetime as a probe of the optical antenna's nanoscale LDOS. Two sets of measurements which were taken with different NV center and tip combinations are are presented in Figures (5.9c,e and d,f). It can be seen that the

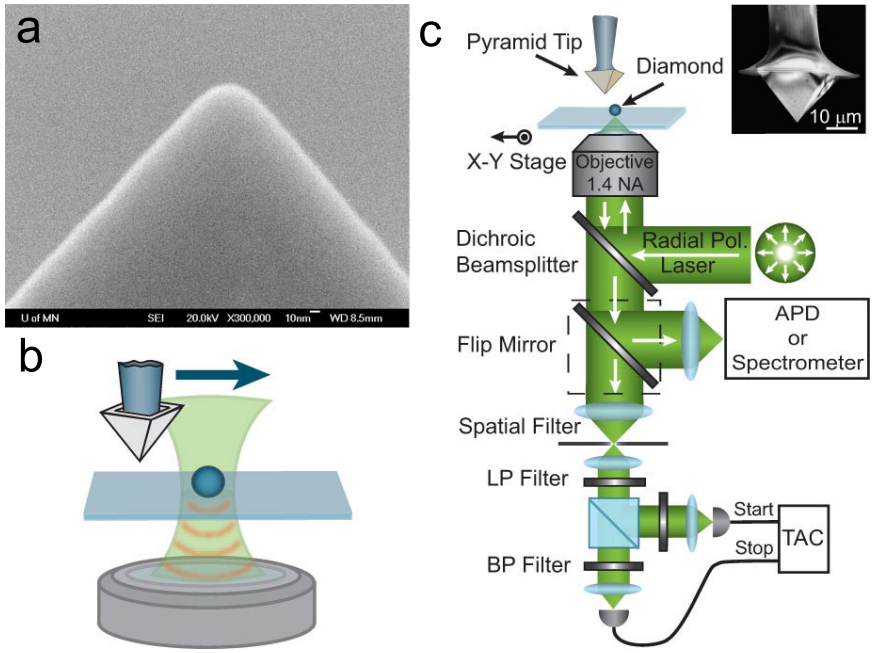

Figure 5.8: **Silver pyramidal tips and experimental setup.** (a) SEM image showing the tip of a silver pyramid with a radius of ≈ 30 nm. This is larger than the gold pyramids, but the increase in the usable wavelength range for the silver pyramids still made them more useful for here. (b) For this experiment the probe (NV center) is fixed in space and the object (pyramid) is scanned over it. (c) An inverted confocal microscope coupled with an AFM were used for the measurements. Detection was done with either a single APD, spectrometer, or pair of APDs (for intensity autocorrelation measurements). Inset: SEM image of the silver pyramid used. Figure adapted from Beams et al.[16]

hot spot is observable in both the FLIM and near-field measurements, showing that the difference in the lifetime matches with the near-field hotspots and validating the use of FLIM with NV centers. This demonstration shows that the NV center optical transition is a sensitive probe of the local electromagnetic mode structure and could in the future be used as a scannable probe. Also, the use of a well-defined optical antenna (silver pyramid) as the object to be probed allowed for consistent results between experiments

using different tips and once again demonstrates the importance of high-quality, well-defined, and reliable tips.

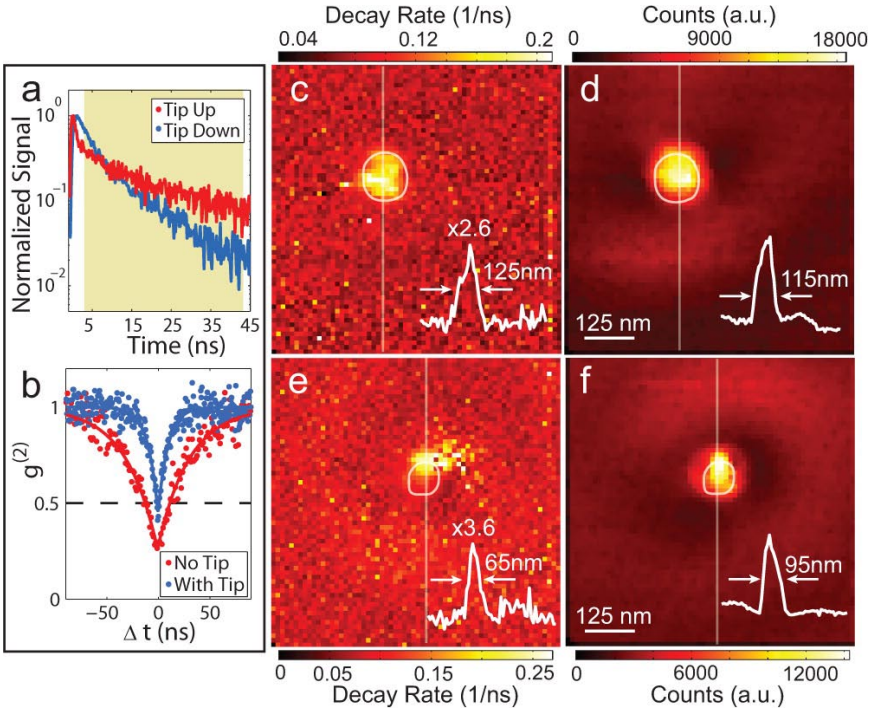

Figure 5.9: **FLIM with a single NV center** (a) Lifetime measurements for the NV center with and without the tip present showing a reduced lifetime with the tip present. (b) Intensity autocorrelation function for the NV center with and without the tip present. (c) FLIM measurements for one combination of tip and NV center and the corresponding (d) near-field fluorescence image. (e) FLIM measurements for a second combination of tip and NV center showing the repeatability and the corresponding (d) near-field fluorescence image. The white outlines represent the NV center location from topography measurements. Figure from Beams et al.[16]

Chapter 6

Template-stripped Sensors

The field of plasmonics has enabled unique devices in a variety of fields. So far this thesis has focused on using plasmonics for nanofocusing and near-field imaging, but another major use is for biosensing.[45,48,165,166] This chapter will focus on a novel plasmonic sensor to use for biosensing.

The use of surface plasmons for biosensing has seen significant progress using a variety of methods for excitation and detection.[48,166–169] Some of these structures include nanohole arrays,[45,165,170–177] nanoparticles,[178,179] and plasmonic interferometers.[180,181] These new sensors all show potential to enhance the sensitivity, multiplexing capacity, and biological interfacing of plasmonic sensors compared to conventional SPR instruments. The most commonly used plasmonic sensor has a very simple structure consisting of a ≈50 nm gold film on a prism which allows for Kretschmann excitation of SPs on the surface.[166,182,183] This sensor has gained popularity because no nanofabrication is needed to make it, and the reflective-mode geometry decouples the optical sensing path from the fluidic channels. When the optical path goes through the sensing fluid, as is common for transmission-mode plasmonic biosensors[45,165] or grating-based SPR sensors,[167,184] interference can occur causing the sensor to not work especially when using opaque, turbid, bubbly, or highly scattering fluids. Though quite useful, the

prism-coupling method also has significant drawbacks. First, the optical setup needed to create the large angle of incidence and collection can be cumbersome to align and often requires specialized equipment. Second, the sensing surface is tilted with respect to the optical axis making imaging difficult due to distortion and the depth-of-focus of the imaging lens limits the usable sensing area making it difficult to perform parallel imaging over a large, dense microarray.[171] Finally, it is difficult to tune the spectral resonances of the structure. Due to these limits, work is being done to find a nanoplasmonic sensor which allows for high-resolution, multiplex sensing at normal incidence with a conventional microscope.[168] Some of the plasmonic sensing methods used are shown in Figure (6.1a-c). Challenges are still being faced, though, to increase the sensitivity and performance of the sensors while still having a reproducible structure. The fabrication method should be able to produce high-quality structures at a low cost to make it viable for widespread use. One of the fabrication difficulties comes from surface roughness which can cause unwanted broadening and attenuation of the plasmonic resonances, sample-to-sample variation, and reduced SP propagation lengths.[55] The roughness can also degrade the quality of self-assembled monolayers or lipid membranes formed on the surface for sensing.[185,186] To solve this problem, we once again look to the template stripping method first presented in Chapter 3 which can produce both ultrasmooth unpatterned[187,188] and patterned[47,114,189] metal films. The ultrasmooth surface not only improves the plasmonic performance, but can also help improve the surface chemistry.[190] Many sensors have been made, but a method allowing for high-resolution SPR imaging with the optical path and fluidic path decoupled made from ultrasmooth metals with integrated gratings has not yet been realized. In this chapter a new sensor design is presented to overcome these challenges and the performance of the sensor is demonstrated.

The following contains work that has been produced though a collaborative effort, and is largely derived from the following publication:

1. Lindquist, N. C., Johnson, T. W., Jose, J., Otto, L. M. & Oh, S.-H. Ultrasmooth metallic films with buried nanostructures for backside reflection-mode plasmonic biosensing. *Annalen der Physik* **524**, 687-696 (2012).[7]

   Contributions: For this paper I helped conceptualize the idea and developed the process. I performed most of the fabrication and all of the SEM imaging. I also performed all of the experimental sensing. Finally, I helped interpret the results and write the paper.

6.1 Backside SPR

Here we show a new device architecture which includes an ultrasmooth, flat top surface with integrated plasmonic nanostructures just below the surface. A method for using this architecture as a biosensor is shown in Figure (6.1d) and offers great flexibility in design and usage. This sensor combines many of the advantages of conventional prism-based SPR instruments, such as a flat sensing surface and a reflection-mode geometry, with the advantages of more complex plasmonic biosensors, such as wide optical tunability, normally incident light, high-resolution imaging, and multiplexing, to create a versatile and user-friendly device. This new method is also not limited to only making biosensors, and could be used for nanophotonic circuitry and waveguides,[191] interferometric sensors,[180] spatial light modulators, plasmonic trapping,[38] or manipulating self-assembled monolayers and lipid bilayers.[192]

6.1.1 Method

The fabrication scheme is shown in Figure (6.2) and starts with the deposition of a 20 nm thick Au film by evaporation onto a clean silicon wafer [Figure (6.2a)]. Next, the desired structures are patterned by e-beam lithography followed by a 50 nm Au deposition and a lift-off process in acetone. The resulting structure is shown in Figure (6.2b) and consists of 50 nm tall Au stripes on top of the first 20 nm thick Au film. Care

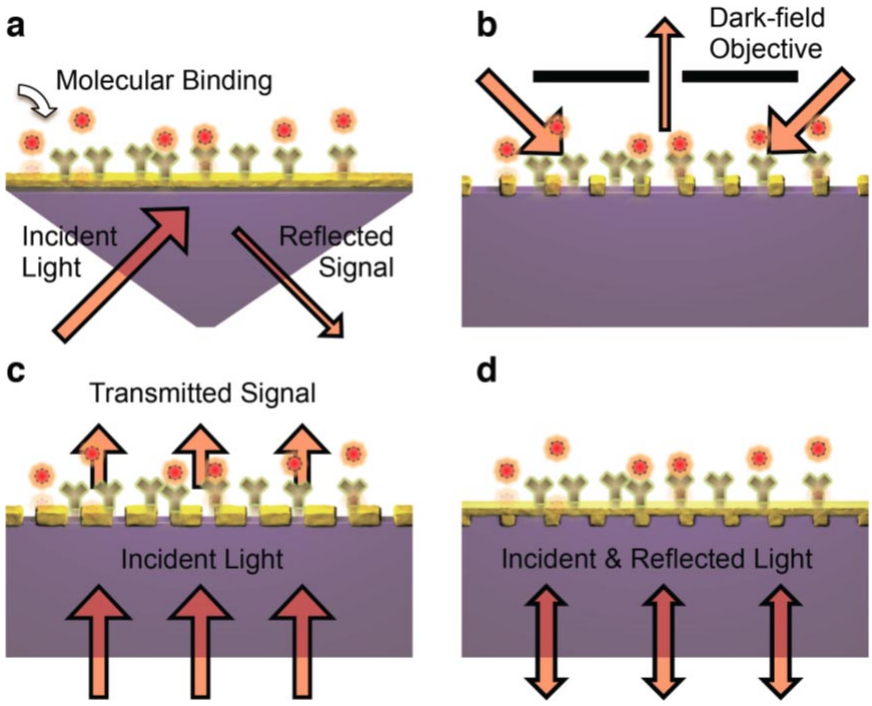

Figure 6.1: **Plasmonic sensing schemes.** (a) The most common, Kretschmann prism coupling. The optical and fluidic paths are decoupled, but light is incident at an oblique angle. (b) Nanoparticles as sensors. High sensitivities are possible, but the particles contribute significant topography to the sensor surface. (c) Nanohole array as a plasmonic sensor. Normal incidence is used, but the transmission mode geometry restricts the fluids used to only transparent ones.

needs to be taken during these processing steps to not damage the thin, initial Au film. Next, an optically transparent epoxy is applied (Norland 61) and the whole structure is template stripped from the silicon mold as seen in Figures (6.2c-d). The final sensor is shown in Figure (6.2e) and it can be seen that the patterned lines are buried in the epoxy and the final sensor surface is the ultrasmooth, template-stripped Au. This surface has a root-mean-square (RMS) roughness of less than 0.5 nm as measured by AFM, and the scans are shown in Figure (6.3).

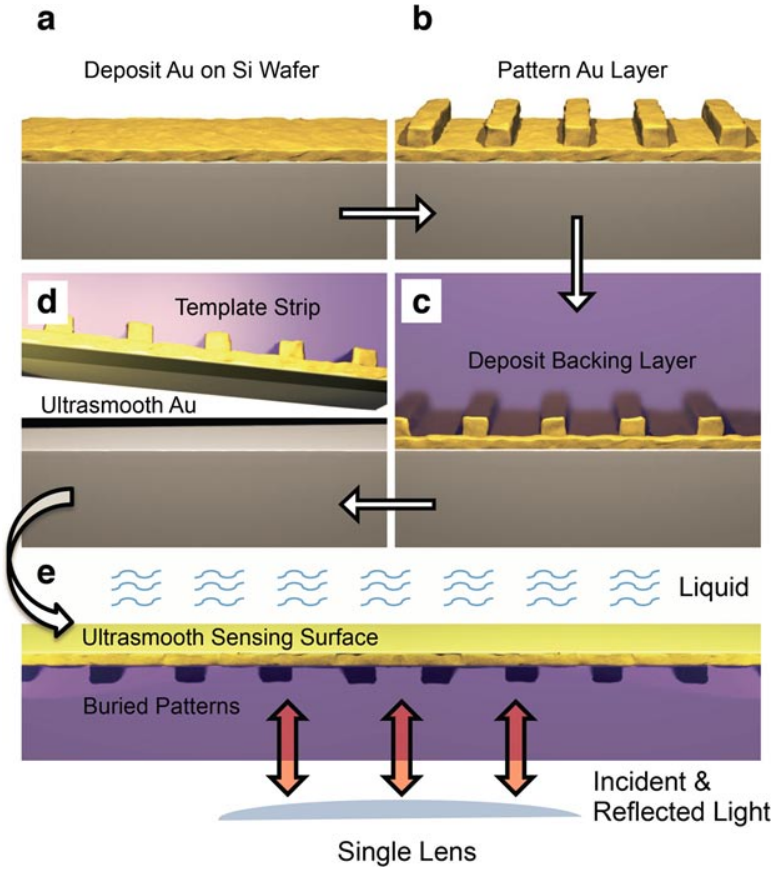

Figure 6.2: **Backside SPR fabrication schematic.** (a) A 20 nm thick layer of Au is deposited on a flat Si mold. (b) 50 nm thick Au lines are added. (c) An optically transparent epoxy is applied and (d) the device is template stripped from the mold. (e) The final device has an ultrasmooth top surface with nanostructures buried in the supporting backing layer.

Devices were fabricated with the grating period and linewidth being varied to demonstrate the tunability of the structure. Figure (6.4a) shows the optical reflection from an array of devices when illuminated through a 5x, 0.15 NA objective with 633 nm light and the varying response can be seen. SEM images of the sensor are shown in Figure (6.4b) before template stripping and in Figure (6.4c) after template stripping. The grating can still be seen through the thin Au layer in Figure (6.4c) by using a 15 keV SEM

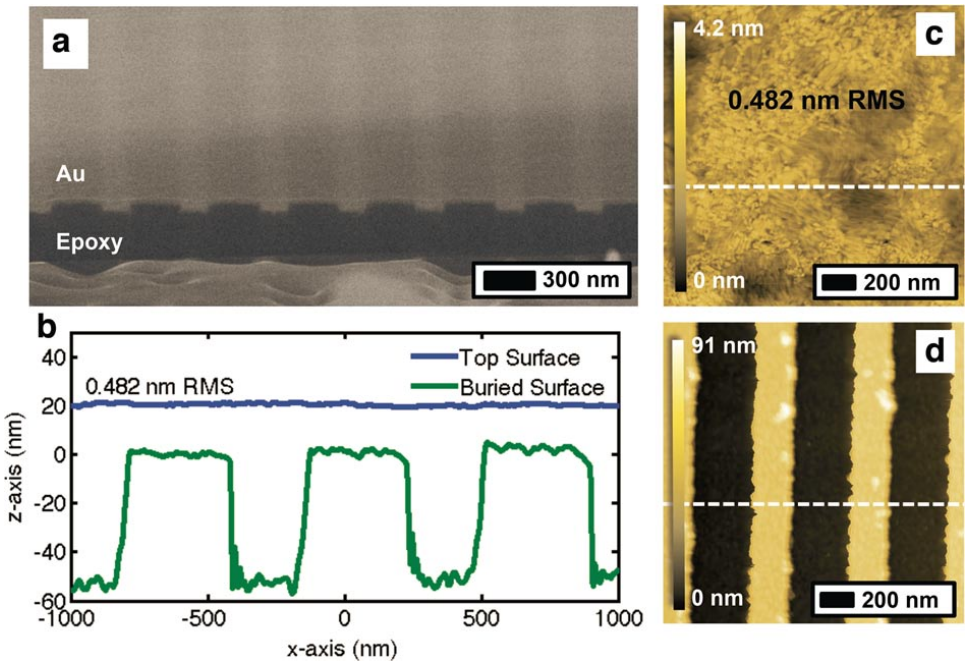

Figure 6.3: **Characterization of the sensor.** (a) Cross-sectional SEM image of the device. (b) AFM scans of the two sides of the metal film (before and after template stripping). (c) AFM scan of the sensor surface after template stripping shows less than 0.5 nm RMS roughness. (d) AFM scan of the gratings before template stripping. The dashed lines indicate the positions of the line-cuts used in (b).

accelerating voltage. This same process can be used to make a variety of other devices as well, with two examples being an embedded bull's eye[62] in Figure (6.4d) and an array of embedded nanodots in Figure (6.4e). For sensing applications all of the optics can be performed on the grating-side of the film leaving the ultrasmooth top surface free of restrictions when adding fluidics for biosensing applications. This allows for the use of complex microfluidic assemblies[193] and opaque liquids without needing to deal with the absorption or scattering which causes problems in grating-based SPR sensors[167] and transmission-mode sensors. Additionally, since both collection and excitation are done though a single lens at normal incidence, the alignment is straightforward and changing the magnification or illumination wavelength is trivial.

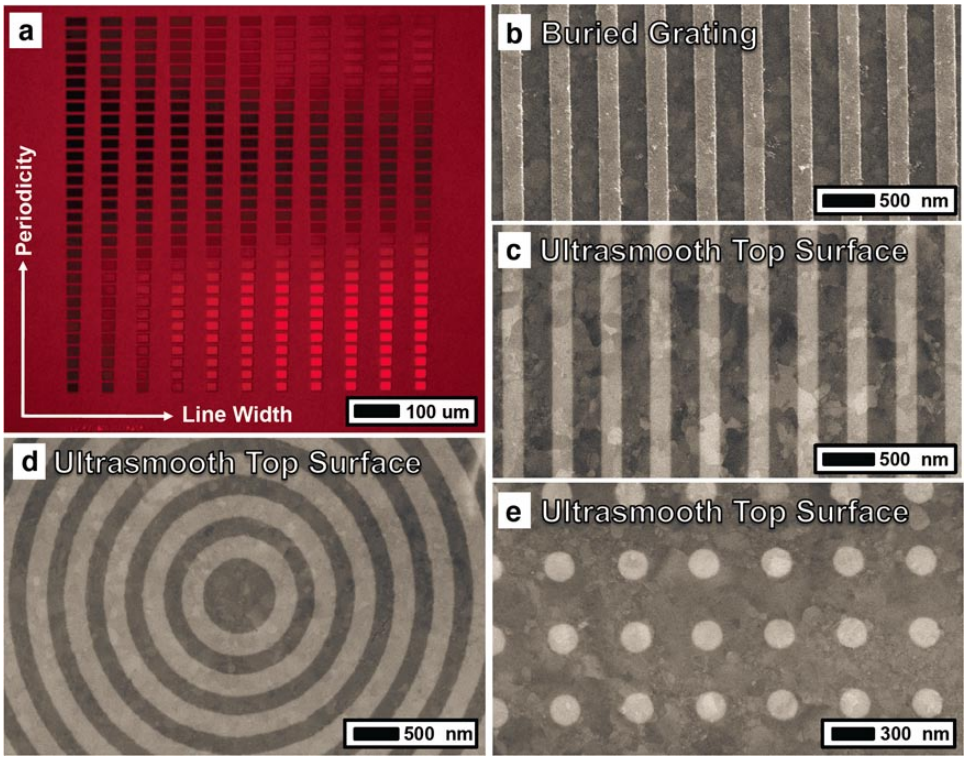

Figure 6.4: **Various plasmonic devices with backside features.** (a) Microscope image showing an array of buried grating devices. SEM image of a buried grating structure (b) before and (c) after template stripping. (d) A buried bull's eye and (e) buried nanodot array structure showing other structures possible with this fabrication method.

The backside grating devices were characterized though both FDTD simulations and experimentally. The FDTD simulations were 2D since the gratings are infinite in one dimension. The light was incident onto the grating side of the sensor and collected from the same side. The incident light was linearly polarized and oriented as to excite the plasmon resonance in this structure. A grid size of 10 nm was used in the x direction and in the z direction a 10 nm grid was used in the bulk and graded down to 1 nm at the sensor surface. To determine the field penetration depth, the point at which the z-component of the electric field amplitude had decayed to 1/e of the value at the

metal surface was used. Experimentally optical reflectivity measurements were done using an Eclipse Ti Nikon microscope with a 5x 0.15 NA objective. For illumination linearly polarized light was used and the back aperture of the objective was under-filled to provide mostly normal-incidence illumination. The light was sent to an imaging spectrometer (Newport MS-257i) to obtain the spectra. Bulk index sensing experiments were performed with glycerol in water mixtures where the glycerol percentage was varied to vary the index of refraction. The refractive indices were verified with a refractometer (Refracto 30PX, Mettler Toledo). Local index sensing was done using successive thin layers of ALD. After a layer of ALD was added, water was placed on the sensor surface to mimic the environment of a sensing experiment and the reflection spectra was obtained. Then the chip as dried with high-purity N_2 and the next layer of Al_2O_3 was applied, starting the process over again. The reflection spectra were normalized to the reflection from an unpatterned region where only the first, thin Au layer is present.

6.1.2 Results and Discussion

The reflection spectrum from an Au grating device with a period of 500 nm and a linewidth of 200 nm was obtained both through measurement [Figure (6.5a)] and simulation [Figure (6.5b)]. Three reflection dips are clearly seen in both spectra. For simulations the 20 nm thick Au film is placed at z = 0, with the buried gratings located at $z < 0$. The sensor area located at $z > 20$ nm and is filled with water (n = 1.33) and the area below the film ($z < 0$) is filled with epoxy (n = 1.56).

The origins of the multiple resonances can explained by looking at the two-fold contribution of the grating bumps. A similar strong plasmon coupling between multiple features was observed by Teperik et al. in a buried nano-void device.[194] The first contribution of the bumps in our device is to act as periodic coupling elements to excite propagating SPs on the metal film. Since the Au film is very thin, the plasmons on the two sides of the film will be strongly coupled (as discussed in Chapter 4). When light is re-radiated from these plasmons, it interferes with the directly reflected light

and creates resonance dips in the reflection. The penetration depth of propagating SPs into their surrounding dielectric medium is usually around 100-300 nm[195] and in our case penetrates 140 nm into the water. A second plasmon mode generated by the bumps is the localized plasmon resonance of the individual bump structures. These resonances will have a shorter lifetime than the propagating modes which translates into a broader resonance.[196] The field from this resonance is strongly concentrated at the bump-substrate interface, extending only 30 nm into the substrate in this case, and can easily couple back to propagating light. The three reflection dips seen in the visible spectrum are plotted in Figure (6.5b) and were studied individually by looking at the z-component of the electric field and are shown in Figure (6.5c). The resonance at 671 nm shows a strong field around the bumps, but the characterizing feature is the large penetration of the field into the water, so we will call this the water-side grating resonance. The resonance at 877 nm, in contrast, shows a large penetration of the field into the substrate, and we will call it the substrate-side grating resonance. The resonance in the middle at 752 nm we will call the coupled-mode resonance and shows a combination of propagating and localized modes penetrating into both the water and substrate sides similarly.[194,197] This resonance shows the shortest penetration depth of 80 nm into the water, or sensing side, of the Au film.

To better understand the resonances, many spectra were compared from devices with a period 300 nm to 1000 nm and are shown experimentally measured in Figure (6.6a) and from simulation in Figure (6.6b). First, by looking at the grating period range of 300 to 400 nm, a strong reflection dip is located at $\approx$ 780 nm in simulation and $\approx$ 670 nm experimentally which is mostly insensitive to changes in the period. This indicates a localized resonance, and the feature can be seen to extend through all of the grating periods. This region is highlighted by the dashed rectangles in Figures (6.6a-b). This mode can also couple with propagating modes, which is why there are areas where the localized resonance is less pronounced. The propagating modes can be solved for using an equation similar to Equation (4.1) since the film is thin enough

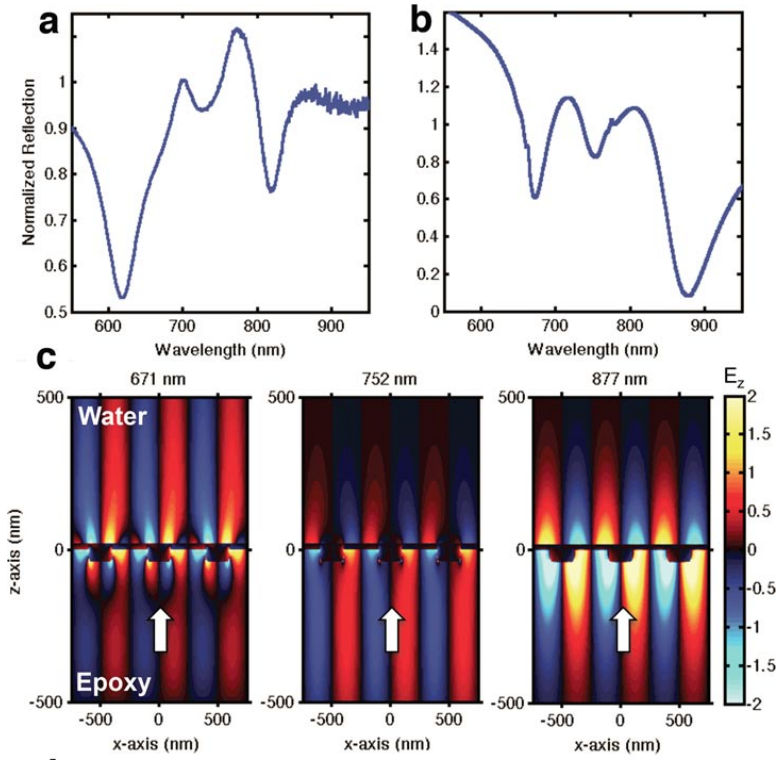

Figure 6.5: **Simulation and experimental characterization.** (a) Measured reflection spectra from a device with a period of 500 nm and linewidth of 200 nm. (b) FDTD reflection spectra for the device in (a). (c) Field maps showing the z-component of the electric field corresponding to the three dips in (b). The arrows indicate the direction of illumination. The spectra in (a)-(b) are normalized to the reflection from an unpatterned region.

to assume strongly coupled IMI plasmon modes.[198] This equation needs to be slightly modified to take into account the asymmetric (epoxy-gold-water) structure. The two resonances obtained by solving the full asymmetric IMI dispersion relation are plotted with dashed lines in Figures (6.6a-b). The lines are very sensitive to period indicating a grating-coupled plasmon. These resonances can be seen to intersect with the localized resonance to create many peaks and dips. This means that we are seeing a combined effect of the grating-type IMI plasmon and the localized mode to form the various modes

in our structure.[199]

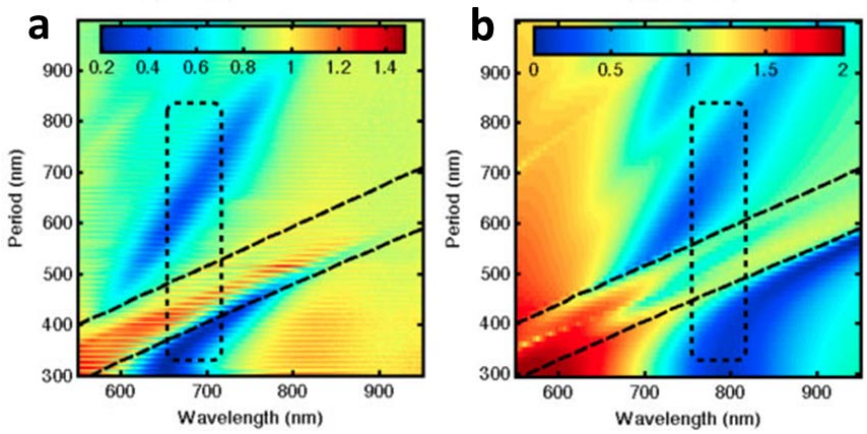

Figure 6.6: **Reflection spectra from devices with varying period** (a) measured experimentally and (b) from simulations. The black dashed lines represent the grating resonances for the propagating IMI plasmon modes and the dashed rectangle the localized resonance of the bump. The spectra are normalized to the reflection from an unpatterned region.

Sensing experiments were then performed, and the first step was to determine which peak to use. The bulk sensitivity was checked though FDTD simulations and it was found that the water-side grating reflection dip at 671 nm shifted by 300 nm per refractive index unit (RIU), the coupled-mode dip at 752 nm shifted 240 nm / RIU and that the peak between these two dips at 720 nm shifted by 356 nm / RIU. Thus the peak between these two reflection dips was used for sensing. In previous works it has been shown that spectral peaks and dips can have different responses due to the excitation of various propagating and localized modes.[200] The peak corresponding to the substrate-side grating plasmon did not shift significantly due to changes to the refractive index on the sensing side.

Experiments were done to measure both the bulk sensitivity and the local sensitivity of our device. For the bulk sensitivity measurement a microfluidic channel was put on the sensing surface and liquids with varying indices of refraction were injected. The position

of the peak with a wavelength around 700 nm was recorded for different solutions and the shift is plotted in Figure (6.7a). The bulk sensitivity is measured to be 410 nm per RIU. The shift of the spectral dip at 726 nm was also recorded and plotted for comparison. The local sensitivity is also important to measure, because for most sensing experiments the molecular interactions occur within a few nanometers of the surface. To measure this, thin layers of Al_2O_3 were successively deposited in a controlled manner via ALD while the peak position was monitored.[201,202] A 50 nm thick layer of Al_2O_3 was added in 2.5 nm steps at the beginning and increasing to 8 nm steps. The shift in the peak at 700 nm was once again followed and is shown in Figure (6.7b). This shows a linear shift if 1.1 nm per nm of Al_2O_3. These experiments show a slightly smaller shift compared to similar experiments done previously because they were done in water. This was done to better mimic the final use of the device but lowers the sensitivity since the change in the index of refraction is less between the water and Al_2O_3 compared to air and Al_2O_3. The local sensitivity was also characterized by measuring the peak shift before and after the sensor was soaked in a 1 nM solution of dodecanethiol in ethanol to form a self-assembled monolayer on the surface. This gave a spectra shift if 1.5 nm.

Many of the sensors which use plasmon resonances have an optical path which goes through the liquid being studied. This type of geometry requires that the liquid be optically transparent. Our device, though, has the optical path and the sensing liquid on opposite sides of the sensor so they do not interfere which allows for the use of opaque liquids. Food coloring dye of various concentrations was injected onto the sensor as shown in (6.7c) and the spectra was monitored and is shown in (6.7d). As the concentration increased the peak position shifted as expected, but there was no degradation of the signal as the solution become more opaque. As another example of a highly scattering liquid, a solution of milk was slowly injected onto the sensor and the spectral response was monitored in time with one spectrum taken every 2.7 sec. The shift in the position of the peak is plotted in (6.7e). The initial shift of 2 nm is mostly due to the bulk index change of the liquid and after rinsing with water a net shift of

about 0.5 nm is seen which is due to the absorption of milk proteins onto the Au surface. Being able to do measurements with liquids such as these would not be possible with many other plasmonic biosensors and demonstrates a key advantage to this backside buried grating structure.

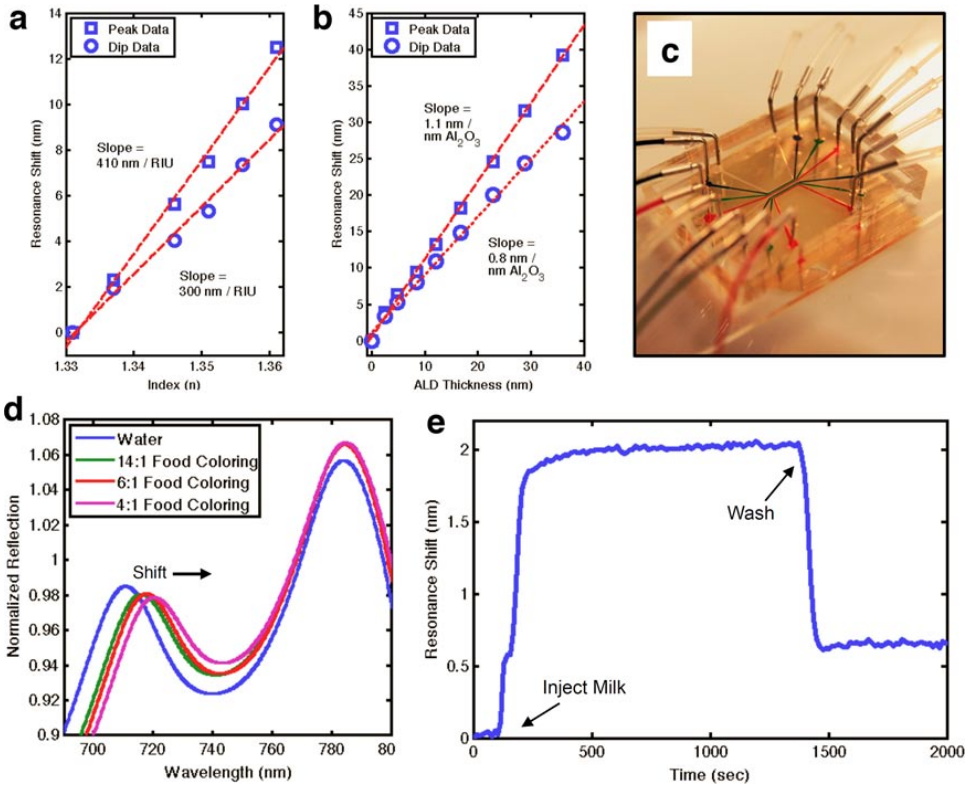

Figure 6.7: **Sensing with the backside SPR grating device.** (a) Bulk index measurements were done with varying concentrations of glycerol and water and show a sensitivity of 410 nm RIU^{-1} (b) Local sensitivity measurements were done with Al_2O_3 deposited by ALD giving a sensitivity of 1.1 nm per nm Al_2O_3. (c) Photograph of an example microfluidic chip. The backside geometry allows for the use of opaque and highly scattering solutions. (d) Spectra taken with varying concentrations of food coloring dye. (e) Real-time sensing of milk proteins absorbing to the Au sensor surface.

Here we show a new fabrication method to make devices with an ultrasmooth, flat

top surface which can be coupled to various nanoplasmonic structures buried in the substrate. When used as a sensor, this architecture maintains many of the benefits of conventional prism-based SPR systems since it operates in a reflection-mode geometry. This decoupling of the optical path and sensing solution allows for the use of opaque and high scattering solutions. This sensor also allows for the resonances to be easily tuned and to operate with normally incident light. The ultrasmooth surface of the sensing layer can be important when studying the biophysics of lipid membranes, membrane-bound receptors, or lipid rafts. Using the same method many other devices are possible as well such as on-chip nanophotonic circuitry and plasmonic trapping.

Chapter 7

Conclusion and Future Directions

7.1 Summary

This thesis presents a variety of novel metallic structures which can be used for plasmonic nanofocusing. The enabling technology used as the basis for these devices is template stripping. Template stripping makes it possible to fabricate ultrasmooth, patterned metallic films (Au and Ag) in a cost effective manner. This feat has not been previously possible due to the inherent roughness of as-deposited metals and difficulty in patterning due its polycrystalline nature. Work is done to demonstrate the capabilities of template stripping such as nanometric control over bump and groove heights, and integration of bumps, grooves, and holes. Next, template stripping is used to fabricate devices for nanofocusing.

Nanofocusing can applied to a variety of applications such as surface-enhanced spectroscopy, optical trapping, non-linear optics, heat-assisted magnetic recording, and single molecule fluorescence. Most methods to make sharp, metallic tips for nanofocusing suffer from low-throughput or low reliability. Here a new method is shown which can make reliable tips for nanofocusing in a high-throughput manner. This method can produce thousands of tips in parallel and yields can reach 95%. These tips are also very

high quality and can produce excellent results. The tip's performance was demonstrated through single-molecule near-field imaging. For single-molecule fluorescence, a resolution of < 20 nm was shown along with a measured fluorescence enhancement of > 200x. Near-field Raman imaging of carbon nanotube bundles was also shown demonstrating the versatility of the tips.

This new fabrication method also makes it possible to fabricate more complicated tip structures. Taking advantage of the ability to make more complex patterns with template stripping, two new schemes are shown which improve the capabilities of nanofocusing. Both of these schemes allow for the incident light to come from inside the pyramid and focus on the outside at the tip. The first makes use of a metal deposition at an angle to create an internal asymmetry to the pyramid. This allows for Kretschmann-like coupling on one face of the pyramid to generate plasmons which travel towards, and are focused by the tip. The other method places a C-shaped aperture around the tip which allows for efficient coupling of light from the inside to the tip. Both methods show significant nanofocusing with minimal background signal from the incident light.

7.2 Future Directions

Significant interest has been show for the distribution of the tips described in Chapter 5. Most companies making near-field imaging systems don't have the capability to provide a reliable and high-quality sharp metallic tips, and this is has been referred to as one of the biggest challenges to overcome in the near-field community. The process to make the tips has been patented,[203] and currently the University of Minnesota's office of technology commercialization is in negotiations with multiple companies who wish to license the technology. It is the hope that by doing this we will make it possible for researchers around the globe to use these tips for routine experiments. By making it more reliable to perform experiments we hope that the entire field will also grow with people exploiting the capabilities of near-field imaging in an array of fields.

There are also many possible extensions to this work. There is optimization on the fabrication which can still be done, different packaging schemes to be explored, and integrating some of the demonstrated nanofocusing concepts into near-field imaging microscopes. Here is a list of some of the possibilities which I have started to explore, but have not yet come to completion.

7.2.1 Oxidation sharpened tips with tunable cone angle

While the cone angle of these tips works well in our current optical setup, there are also times when different tip angles are desired. It has been shown that the tip angle can be tuned through dry oxidation of the silicon mold before metal deposition.[?,204] The oxide layer formed is not formed uniformly on the mold at sharp features and the tip angle can be tuned to be shallower with the angle dependent on the oxidation time. This has been shown for an array of pyramid tips, but not yet with near-field imaging. The concept is shown in Figure (7.1), where Figure (7.1a) shows the cross-section of a wedge a mold before oxidation and Figures (7.1b-d) show the mold after oxidation. I made some of these tips in a manner allowing them to be integrated with near-field imaging and then with a collaborator performed TERS imaging of nanotubes. We were able to get a resolution of <20 nm with decent field enhancements, but they did not perform as well as expected. The yield was also not sufficient, and the resolution not much improved. More work needs to be done here to optimize the time of oxidation and also re-optimize the metal deposition conditions. Since the tip angle is changing, it is possible that the ideal metal deposition conditions will be different. Once this method is optimized, it will give another knob which the designer can turn to create a tip optimized for a given situation.

7.2.2 Cantilever integration

The packaging of the tips is another area where advancement can be made. For imaging, the tip needs to be close to the surface of the sample, and so a feedback mechanism

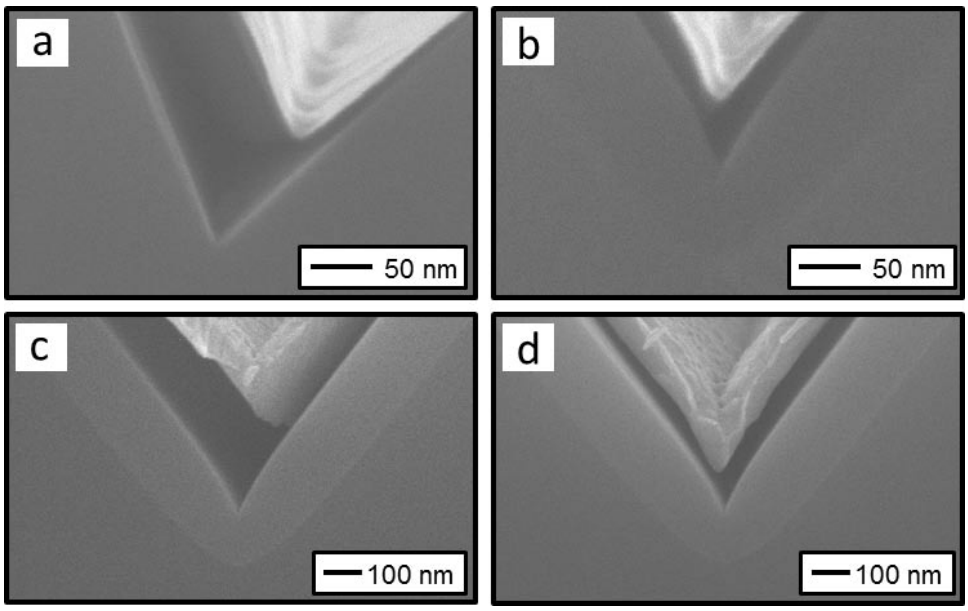

Figure 7.1: **Oxidation-tuned tip angle.** (a) Cross-sectional SEM image of a silicon mold before oxidation. (b)-(d) Cross-sectional SEM images of silicon molds after dry oxidation in a furnace at 1000°c. The oxide does not uniformly grow an the tip angle can be tuned by varying the time of oxidation.

needs to be used. For this work the pyramids were mounted on a tuning fork like the one shown in Figure (7.2a) and operated in either shear-force mode or dynamic normal mode for feedback. Another common resonator used in most commercial AFM systems is a cantilever. If the tips could be integrated with a cantilever they could find easier integration into AFM systems. Initial tests have been done using a small drop of epoxy to attach a tip to a pre-fabricated cantilever. The epoxy is placed on the silicon tip of a normal AFM cantilever, and then maneuvered to a metal tip in the mold. The epoxy is cured and then the cantilever is pulled away from the mold, taking the metal tip along with it. This has had some success as shown in Figures Figure (7.2b-c), but the process is not reliable. One problem is poor adhesion between the silicon cantilever and the epoxy. To improve this adhesion a 10 nm thick later of chromium was first evaporated

onto the cantilever. Another problem is that the cantilevers frequently break while attempting to pull the tip from the mold. Through optimization of the holding of the cantilever, the cantilevers used, and epoxy, this process should be possible and will open the door for more researchers to use these tips. It could also be possible to develop a process where the cantilevers are fabricated alongside the tips. One method would make use of SU-8 as the cantilever material due to its ease of patterning. This could allow for the mass-fabrication of tips which are pre-packaged and also remove the step of needing to attach the tips to tuning forks.

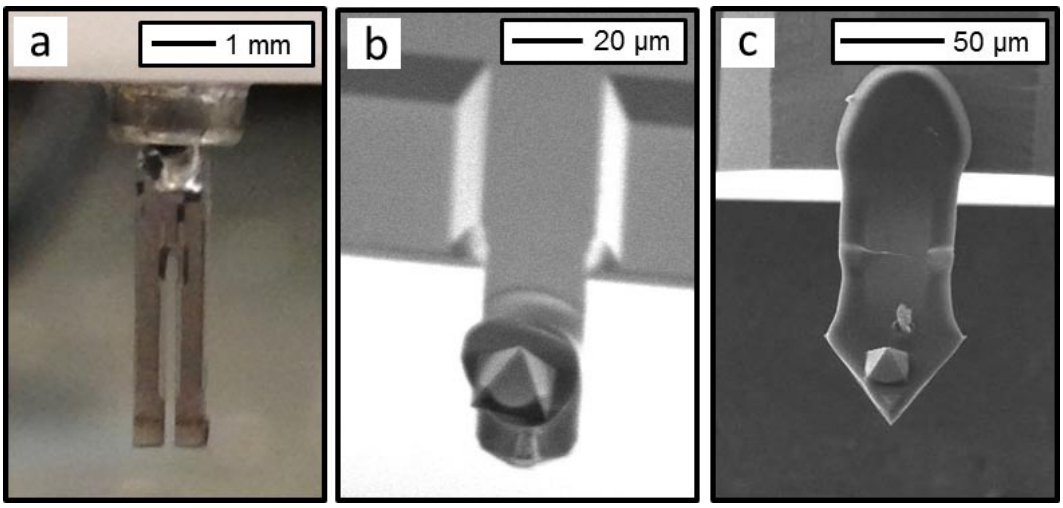

Figure 7.2: **Pyramid tips mounted on cantilevers.** (a) Photograph of a tuning fork used for feedback. (b)-(c) SEM images of tips attached to silicon cantilevers. This packaging scheme would increase the versatility of the tips.

7.2.3 Conductive pyramids

Another packaging scheme which would be beneficial is to make the tips electrically conductive. If the tips were electrically conductive they could be used for scanning tunneling microscopy (STM), where the feedback mechanism is a tunneling current between the tip and sample. STM mode operation would allow for studies combining

STM and optics such as light-emission studies. The one insulating component in the system is the epoxy used to attach the pyramid tip to the wire. Initial tests have attempted to use conductive epoxy and show that the tip response to an AC current,[19] but no proof of DC conductivity has been shown and the method does not make a reliable connection. The problem comes from how the epoxy is made conductive. Generally the epoxy contains silver flakes on the order of about 20 μm encased in a non-conductive epoxy. In normal use these flakes touch each other and make the bulk sample conductive. Here, though, the connection size is smaller than the silver flakes, and it is thought that generally no flakes are between the tungsten wire and the pyramid. Another possible scheme to make the tips conductive is shown in Figure (7.3). Here, the pyramid is patterned so that a large gold pad is left around the pyramid itself. When the pyramid is pulled out, the pad comes along with it as in Figure (7.3a). If the pad is then pushed up around the supporting wire as in Figure (7.3b), the electrical connection will be made. Here the malleability of gold is used in our favor allowing the structure to be easily re-formed. Initial tests have been tried, but optimization for this method is needed along with proof-of-concept experiments to demonstrate their conductivity.

7.2.4 Patterned tips

It could also be possible to add more functionality to these tips by making patterns on the pyramids. It has been previously shown that gratings can be patterned surrounding the tip and can allow for linearly polarized light to excite nanofocusing at the tip.[110] This has the benefits of being easier to excite (since radially polarized light is not needed), potentially greater coupling of the excitation light to the near-field spot, and potential for control over the polarization at the tip. Pattern pyramids have been made and are shown in Figure (7.4). Figures (7.4a) and (7.4b) show the difference between an unpatterned and patterned pyramid. Figure (7.4c) shows an SEM image of the patterning around a tip which form the gratings, and Figure (7.4d) shows a close-up of the tip, demonstrating that the tip is still ultra-sharp even after the extra processing.

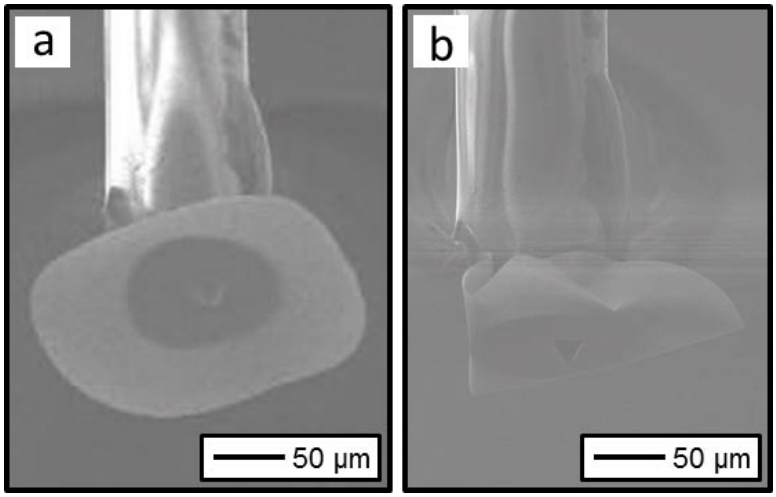

Figure 7.3: **Scheme to make tips electrically conductive.** (a) SEM image of a pyramid tip and surrounding gold pad after removal from the template. (b) The gold pad can then be pushed up against the supporting structure to form the electrical contact. In these images the pyramid was removed with an optical fiber, which could be coated with metal to make it conductive. The same process can be done with a thin tungsten wire.

This also demonstrates the different scales involved. The pyramid itself is around 20 μm, the patterning is in the 100's of nm's range, and the tip has a radius of around 5 nm. All three of these length scales interact to form the single, intense hotspot at the tip. I have fabricated some isolated patterned pyramids with gratings patterned on them, and they are currently being tested with near-field imaging. Some problems still need to be resolved such as the tip ripping out due to the differences in the template stripping procedure of an entire film versus a single tip. These issues are being worked on to be resolved. Once these tips work for near-field imaging, there will also need to be optimization done to determine the best bump spacing, bump size, and number of bumps for each wavelength used. It is also possible for different patterns to be made such as spirals for use with circularly polarized light. This gives the potential to once again extend the capabilities of these tips and allows for some complexity to be taken

away from the containing optical setup due to the increased complexity of the tip itself.

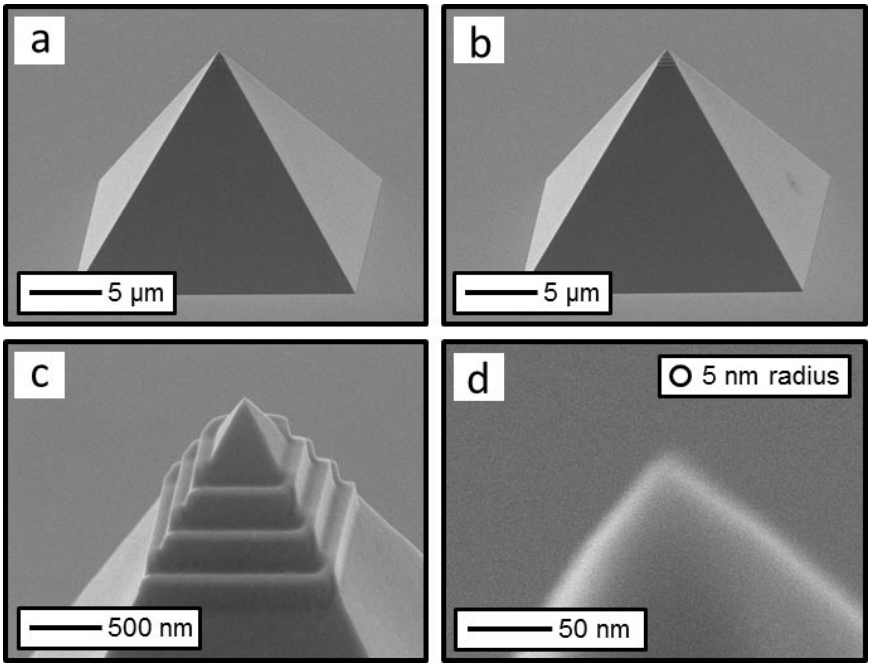

Figure 7.4: **SEM images of patterned pyramids.** (a) A full pyramid with no patterning and (b) a full pyramid with gratings patterned around the tip to generate nanofocusing at the tip from excitation with linearly polarized light. (c) A view of the patterns surrounding the tip showing the high quality metal films which is still produced. (d) A closeup of the tip showing a radius of ≈5 nm, demonstrating that the tip quality is not compromised through the extra patterning step.

7.2.5 Asymmetric tips integrated on an optical fiber

Another useful nanofocusing scheme which could see further development and integration into a near-field imaging system is the asymmetric pyramid scheme introduced in Chapter 4. This scheme allows for the pyramid to be illuminated internally. If instead of a wire, an optical fiber was used to remove the pyramid, the fiber could be used for the illumination, and reduce the background while allowing for more flexibility in the optical setup. I have worked on the process, but further optimization is still needed.

Figures (7.5a-b) show optical images, and (7.5c) an SEM image, of an asymmetric pyramid which has been removed from the mold and attached to a multi-mode optical fiber with optical-grade epoxy. When the pyramid is illuminated through the optical fiber with a 633 nm laser, it appears to be generating nanofocusing at the tip. Figure (7.5d) shows an optical image from a microscope when the pyramid is illuminated both internally and through bright-field to better see the placement of the pyramid. Figure (7.5e) shows the same pyramid with only internal illumination. Half of the pyramid shows some light leakage, as expected, and there is also an intense spot formed at the tip. This looks similar to the film-based pyramids and gives an indication that the system is working, but it has not yet been proven. Further work needs to be done to optimize the pulling and alignment procedures so that the asymmetric tips can be reliably pulled. Also, proof-of-concept experiments can be preformed to demonstrate the nanofocusing such as optical trapping or Raman. After this happens, the fiber can be mounted to a tuning fork and the tip can be scanned to perform near-field imaging. This new modality should provide many of the benefits of aperture-NSOM, but with a much higher resolution since the tip, which defines the resolution, is still intact.

7.2.6 Magnetic tips

It has been shown that it is also possible to template other metals besides gold and silver.[205] This method uses a thin layer of gold which is deposited into the mold first and used as a release layer. The desired metal is then deposited and the entire film stack is template stripped from the mold. Using this same method it could be possible to fabricate pyramids with a magnetic material, such as nickel, to create pyramids which can attract magnetic particles. I have done initial testing of this method with a 30 nm-thick later of gold followed by 200 nm of nickel. Two problems arose. First, when the wafer was removed from the evaporator after the deposition there was a high stress in the film, and since the gold doesn't adhere well to the silicon, and small bump would immediately cause the entire film to delaminate. A wafer after deposition which has

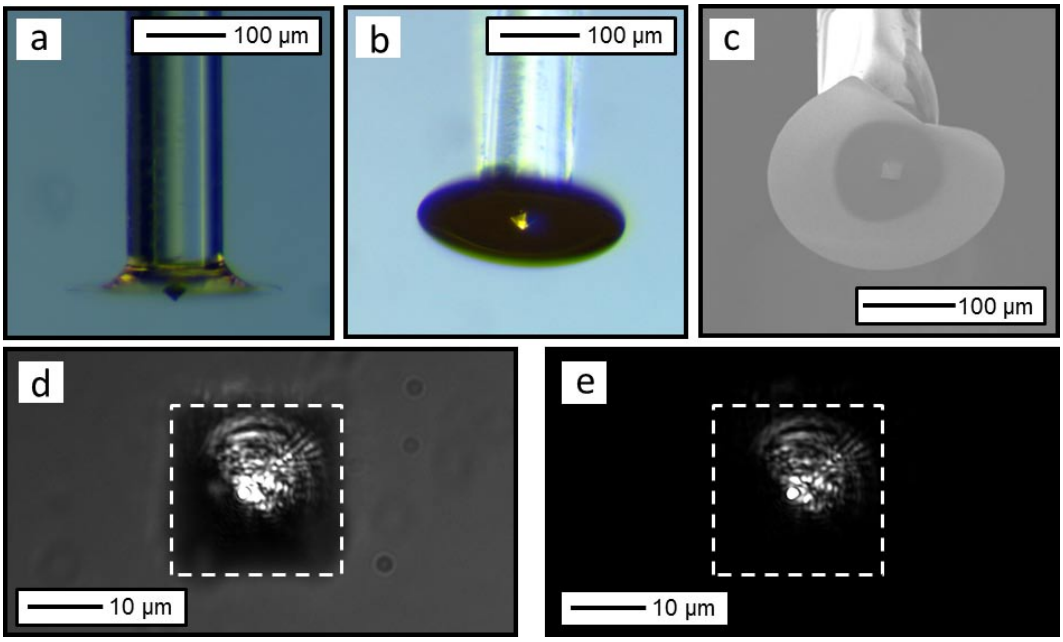

Figure 7.5: **Asymmetric pyramid mounted on an optical fiber.** (a)-(b) Optical microscope images of an asymmetric pyramid glued to an optical fiber with epoxy. (c) SEM image of the tip in (a). (d) Microscope image looking at the pyramid from above with both internal and bright-field illumination. (e) Same pyramid as in (d) with only internal illumination by a 633 nm laser. A bright spot can be seen at the tip indicating nanofocusing.

delaminated can be seen in Figure (7.6a). This problem was solved by letting the films cool before further processing. Secondly, the gold film was not thick enough to form a continuous layer along the sides of the pyramids since the deposition is onto an angled profile, making the thickness normal to the surface less than the nominal thickness deposited. This problem can be seen in Figure (7.6b) where the flat regions show a continuous film, but angled regions defining the pyramid don't have a continuous film. This problem can be solved by increasing the deposited gold layer to either 40 or 50 nm. Wedges have been made through this process and have shown great potential and the ability to attract magnetic beats along the tip. This process can be further developed

and proof-of-concept experiments need to be preformed.

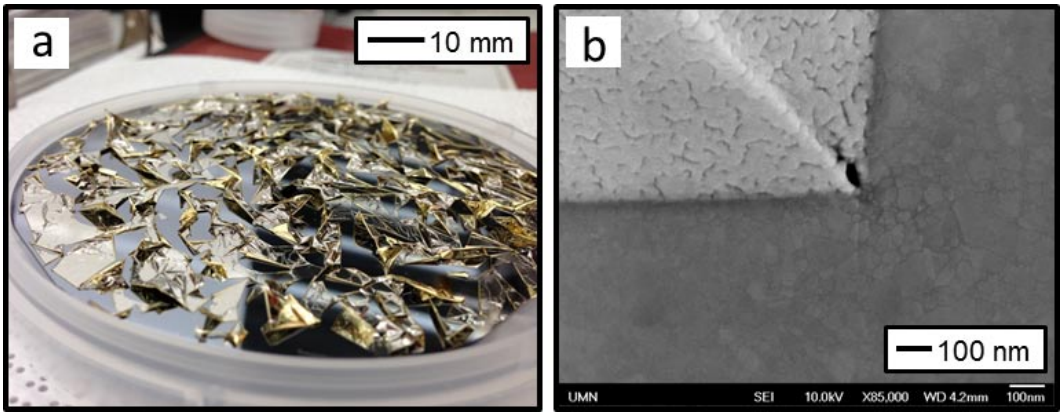

Figure 7.6: **Magnetic pyramids from template stripping.** (a) A photograph of a wafer where the gold and nickel film delaminated after deposition. This problem can be solved by letting the wafer cool before further processing. (b) SEM image of the template-stripped film stack. The gold is continuous in the flat regions, but is discontinuous in the angled regions. This problem can be solved by depositing a slightly thicker layer of gold.

7.2.7 Multi-sized pyramids

There are also times when it might be nice to place a substrate right above the tips of the pyramids, but not touching it. This substrate could be a coverslip to help with imaging or to create a small reservoir of water surrounding pyramid or it could be a conducting electrode to help with processes such as dielectrophoresis.[18] To do this, one could fabricate wedges surrounding the pyramids for protection. The wedges would be made slightly larger, and so would be slightly higher. The initial pattern size could then be adjusted to vary the distance between the supported substrate and the pyramid tip. An example structure is shown in Figure (7.7) where pyramids are surrounded by slightly taller wedges. This idea could help with the integration into other types of sensors and sensing methods.

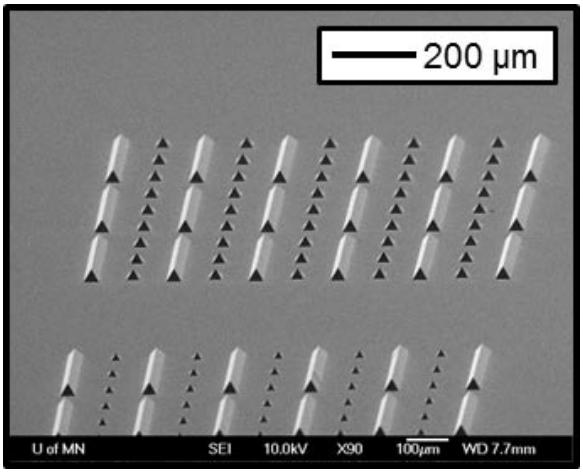

Figure 7.7: **Pyramids surrounded by wedges for protection.** SEM image of an example structure. A substrate can be place on top of, and supported by the wedges which would allow it to come within microns of the pyramid's tip without touching and damaging it.

7.2.8 Integration of multiple features

The power of this process is that many of the ideas presented here can also be integrated together to form even more complex tips. One could, for example imagine a magnetic, patterned pyramid which is mounted on a cantilever or an asymmetric pyramid which is also conductive with a tunable tip angle. Figure (7.8) shows a pyramid fabricated combining a tunable tip angle and the patterning of gratings around the tip. These integration schemes may also just be a sampling of the types of tips possible through the foundation provided by this method.

7.3 Conclusion

This thesis has presented a new fabrication technique for nanofocusing probes. This method opens the door for many possible modifications to the tip which can improve their functionality while also being reliable. This thesis has focused on setting a good

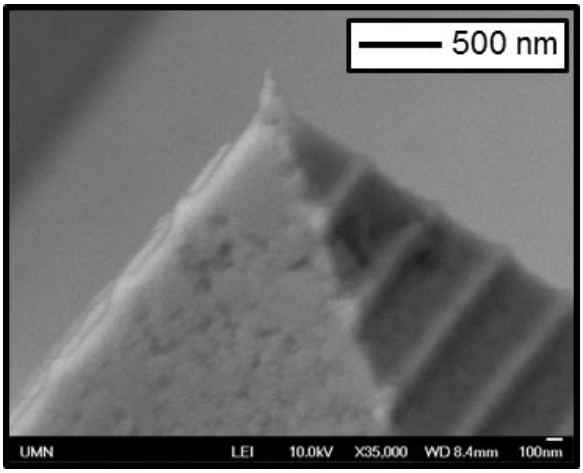

Figure 7.8: **Pyramid combining patterning and tip angle tuning.** SEM image of a pyramid demonstrating the integration of multiple features. Here the tip angle was tuned to be shallower and bumps were patterned around the tip.

foundation and extra effort has been done to optimize the base steps to set the method up well for continued advancement. Steps such as fabricating a sharp mold and optimized deposition conditions will still be used as the tips get more complex, and the better the base pyramids are, the better the more complex ones will be as well. This thesis has proven the method and has also presented either through larger studies (such as asymmetric pyramids) or ideas (such as the ideas immediately proceeding this section) many possibilities for the extension of this method to more complex designs. The invention of a tip which is reliable and can be mass-fabricated is useful in itself, but possibilities this method brings makes it even more exciting. The methods presented here should provide the foundation for many studies in the future and help the field of near-field imaging become more routine to a larger group of people.

References

[1] Im, H., Lee, S. H., Wittenberg, N. J., Johnson, T. W., Lindquist, N. C., Nagpal, P., Norris, D. J. & Oh, S.-H. Template-stripped smooth Ag nanohole arrays with silica shells for surface plasmon resonance biosensing. *ACS Nano* **5**, 6244–53 (2011). [Cited once on page xii.]

[2] Wittenberg, N. J., Im, H., Johnson, T. W., Xu, X., Warrington, A. E., Rodriguez, M. & Oh, S.-H. Facile assembly of micro- and nanoarrays for sensing with natural cell membranes. *ACS Nano* **5**, 7555–64 (2011). [Cited once on page xii.]

[3] Lindquist, N. C., Johnson, T. W., Norris, D. J. & Oh, S.-H. Monolithic integration of continuously tunable plasmonic nanostructures. *Nano Letters* **11**, 3526–30 (2011). [Cited 9 times on pages xii, 17, 20, 22, 23, 24, 27, 28, and 29.]

[4] Luhman, W. a., Hoon Lee, S., Johnson, T. W., Holmes, R. J. & Oh, S.-H. Self-assembled plasmonic electrodes for high-performance organic photovoltaic cells. *Applied Physics Letters* **99**, 103306 (2011). [Cited once on page xiii.]

[5] Lee, S. H., Johnson, T. W., Lindquist, N. C., Im, H., Norris, D. J. & Oh, S.-H. Linewidth-Optimized Extraordinary Optical Transmission in Water with Template-Stripped Metallic Nanohole Arrays. *Advanced Functional Materials* **22**, 4439–4446 (2012). [Cited once on page xiii.]

[6] Wittenberg, N. J., Johnson, T. W. & Oh, S.-H. High-density arrays of submicron spherical supported lipid bilayers. *Analytical chemistry* **84**, 8207–13 (2012). [Cited once on page xiii.]

[7] Lindquist, N. C., Johnson, T. W., Jose, J., Otto, L. M. & Oh, S.-H. Ultrasmooth metallic films with buried nanostructures for backside reflection-mode plasmonic biosensing. *Annalen der Physik* **524**, 687–696 (2012). [Cited twice on page xiii and 81.]

[8] Johnson, T. W., Lapin, Z. J., Beams, R., Lindquist, N. C., Rodrigo, S. G., Novotny, L. & Oh, S.-H. Highly reproducible near-field optical imaging with sub-20-nm resolution based on template-stripped gold pyramids. *ACS Nano* **6**, 9168–74 (2012). [Cited 13 times on pages xiii, 33, 37, 39, 41, 63, 65, 66, 67, 68, 70, 71, and 74.]

[9] Olmon, R. L., Slovick, B., Johnson, T. W., Shelton, D., Oh, S.-H., Boreman, G. D. & Raschke, M. B. Optical dielectric function of gold. *Physical Review B* **86**, 235147 (2012). [Cited 5 times on pages xiii, 17, 30, 31, and 32.]

[10] Lindquist, N. C., Johnson, T. W., Nagpal, P., Norris, D. J. & Oh, S.-H. Plasmonic nanofocusing with a metallic pyramid and an integrated C-shaped aperture. *Scientific Reports* **3**, 1857 (2013). [Cited 8 times on pages xiii, 35, 53, 55, 56, 58, 59, and 60.]

[11] Jose, J., Jordan, L. R., Johnson, T. W., Lee, S. H., Wittenberg, N. J. & Oh, S.-H. Topographically Flat Substrates with Embedded Nanoplasmonic Devices for Biosensing. *Advanced Functional Materials* **23**, 2812–2820 (2013). [Cited once on page xiii.]

[12] Im, H., Bantz, K. C., Lee, S. H., Johnson, T. W., Haynes, C. L. & Oh, S.-H. Self-assembled plasmonic nanoring cavity arrays for SERS and LSPR biosensing.

Advanced Materials **25**, 2678–2685 (2013). [Cited 3 times on pages xiv, 33, and 35.]

[13] Joy, N. a., Janiszewski, B. K., Novak, S., Johnson, T. W., Oh, S.-H., Raghunathan, A., Hartley, J. & Carpenter, M. a. Thermal Stability of Gold Nanorods for High-Temperature Plasmonic Sensing. *The Journal of Physical Chemistry C* **117**, 11718–11724 (2013). [Cited once on page xiv.]

[14] Lindquist, N. C., Jose, J., Cherukulappurath, S., Chen, X., Johnson, T. W. & Oh, S.-H. Tip-based plasmonics: squeezing light with metallic nanoprobes. *Laser & Photonics Reviews* **7**, 453–477 (2013). [Cited twice on page xiv and 35.]

[15] Reitich, F., Johnson, T. W., Oh, S.-H. & Meyer, G. A fast and high-order accurate surface perturbation method for nanoplasmonic simulations: basic concepts, analytic continuation and applications. *Journal of the Optical Society of America A* **30**, 2175–2186 (2013). [Cited once on page xiv.]

[16] Beams, R., Smith, D., Johnson, T. W., Oh, S.-H., Novotny, L. & Vamivakas, A. N. Nanoscale fluorescence lifetime imaging of an optical antenna with a single diamond NV center. *Nano Letters* **13**, 3807–11 (2013). [Cited 5 times on pages xiv, 63, 75, 77, and 78.]

[17] Cherukulappurath, S., Johnson, T. W., Lindquist, N. C. & Oh, S.-H. Template-stripped asymmetric metallic pyramids for tunable plasmonic nanofocusing. *Nano Letters* **13**, 5635–5641 (2013). [Cited 9 times on pages xiv, 34, 41, 43, 44, 47, 48, 49, and 50.]

[18] Barik, A., Otto, L. M., Yoo, D., Jose, J., Johnson, T. W. & Oh, S.-H. Dielectrophoresis-enhanced plasmonic sensing with gold nanohole arrays. *Nano Letters* **14**, 2006–2016 (2014). [Cited twice on page xiv and 103.]

[19] Jose, J., Kress, S., Barik, A., Otto, L. M., Shaver, J., Johnson, T. W., Lapin, Z. J., Bharadwaj, P., Novotny, L. & Oh, S.-H. Individual Template-Stripped Conductive Gold Pyramids for Tip-enhanced Dielectrophoresis. *ACS Photonics* (2014). [Cited twice on page xv and 98.]

[20] Ritchie, R. Plasma Losses by Fast Electrons in Thin Films. *Physical Review* **106**, 874–881 (1957). [Cited twice on page 2 and 10.]

[21] Barnes, W. L., Dereux, A. & Ebbesen, T. W. Surface plasmon subwavelength optics. *Nature* **424**, 824–30 (2003). [Cited twice on page 3 and 33.]

[22] Atwater, H. A. The Promise of Plasmonics. *Scientific American* **296**, 56–62 (2007). [Cited once on page 3.]

[23] Ozbay, E. Plasmonics: merging photonics and electronics at nanoscale dimensions. *Science* **311**, 189–93 (2006). [Cited once on page 3.]

[24] Schuller, J. A., Barnard, E. S., Cai, W., Jun, Y. C., White, J. S. & Brongersma, M. L. Plasmonics for extreme light concentration and manipulation. *Nature Materials* **9**, 193–204 (2010). [Cited once on page 3.]

[25] Lal, S., Link, S. & Halas, N. J. Nano-optics from sensing to waveguiding. *Nature Photonics* **1**, 641–648 (2007). [Cited twice on page 3 and 33.]

[26] Bethe, H. Theory of Diffraction by Small Holes. *Physical Review* **66**, 163–182 (1944). [Cited once on page 3.]

[27] Ebbesen, T., Lezec, H., Ghaemi, H., Thio, T. & Wolff, P. Extraordinary optical transmission through sub-wavelength hole arrays. *Nature* **391**, 667–669 (1998). [Cited once on page 3.]

[28] Shelby, R. A., Smith, D. R. & Schultz, S. Experimental verification of a negative index of refraction. *Science* **292**, 77–79 (2001). [Cited once on page 3.]

[29] Shalaev, V. M. Optical negative-index metamaterials. *Nature Photonics* **1**, 41–48 (2007). [Cited once on page 3.]

[30] Fang, N., Lee, H., Sun, C. & Zhang, X. Sub-diffraction-limited optical imaging with a silver superlens. *Science* **308**, 534–7 (2005). [Cited once on page 3.]

[31] Pendry, J. B. Negative Refraction Makes a Perfect Lens. *Physical Review Letters* **85**, 3966–3969 (2000). [Cited once on page 3.]

[32] Liu, Z., Lee, H., Xiong, Y., Sun, C. & Zhang, X. Far-field optical hyperlens magnifying sub-diffraction-limited objects. *Science* **315**, 1686 (2007). [Cited once on page 3.]

[33] Pendry, J. B., Schurig, D. & Smith, D. R. Controlling electromagnetic fields. *Science* **312**, 1780–2 (2006). [Cited once on page 3.]

[34] Cai, W., Chettiar, U. K., Kildishev, A. V. & Shalaev, V. M. Optical cloaking with metamaterials. *Nature Photonics* **1**, 224–227 (2007). [Cited once on page 3.]

[35] Ergin, T., Stenger, N., Brenner, P., Pendry, J. B. & Wegener, M. Three-dimensional invisibility cloak at optical wavelengths. *Science* **328**, 337–9 (2010). [Cited once on page 3.]

[36] Atwater, H. A. & Polman, A. Plasmonics for improved photovoltaic devices. *Nature Materials* **9**, 205–13 (2010). [Cited twice on page 3 and 23.]

[37] Bozhevolnyi, S. I., Volkov, V. S., Devaux, E., Laluet, J.-Y. & Ebbesen, T. W. Channel plasmon subwavelength waveguide components including interferometers and ring resonators. *Nature* **440**, 508–11 (2006). [Cited once on page 3.]

[38] Righini, M., Zelenina, A. S., Girard, C. & Quidant, R. Parallel and selective trapping in a patterned plasmonic landscape. *Nature Physics* **3**, 477–480 (2007). [Cited twice on page 3 and 81.]

[39] Challener, W. A., Peng, C., Itagi, A. V., Karns, D., Peng, W., Peng, Y., Yang, X., Zhu, X., Gokemeijer, N. J., Hsia, Y.-T., Ju, G., Rottmayer, R. E., Seigler, M. A. & Gage, E. C. Heat-assisted magnetic recording by a near-field transducer with efficient optical energy transfer. *Nature Photonics* **3**, 220–224 (2009). [Cited twice on page 3 and 33.]

[40] Zijlstra, P., Chon, J. W. M. & Gu, M. Five-dimensional optical recording mediated by surface plasmons in gold nanorods. *Nature* **459**, 410–3 (2009). [Cited once on page 3.]

[41] Mansuripur, M., Zakharian, A. R., Lesuffleur, A., Oh, S.-H., Jones, R. J., Lindquist, N. C., Im, H., Kobyakov, A. & Moloney, J. V. Plasmonic nano-structures for optical data storage. *Optics Express* **17**, 14001 (2009). [Cited once on page 3.]

[42] Xu, H., Bjerneld, E., Käll, M. & Börjesson, L. Spectroscopy of Single Hemoglobin Molecules by Surface Enhanced Raman Scattering. *Physical Review Letters* **83**, 4357–4360 (1999). [Cited once on page 3.]

[43] Moskovits, M. Surface-enhanced Raman spectroscopy: a brief retrospective. *Journal of Raman Spectroscopy* **36**, 485–496 (2005). [Cited once on page 3.]

[44] Haynes, C. L., McFarland, A. D. & Duyne, R. P. V. Surface-Enhanced Raman Spectroscopy. *Analytical Chemistry* **77**, 338 A–346 A (2005). [Cited once on page 3.]

[45] Brolo, A. G., Gordon, R., Leathem, B. & Kavanagh, K. L. Surface Plasmon Sensor Based on the Enhanced Light Transmission through Arrays of Nanoholes in Gold Films. *Langmuir* **20**, 4813–4815 (2004). [Cited 4 times on pages 3 and 79.]

[46] Brolo, A. G. Plasmonics for future biosensors. *Nature Photonics* **6**, 709–713 (2012). [Cited once on page 3.]

[47] Dahlin, A. B., Wittenberg, N. J., Höök, F. & Oh, S.-H. Promises and Challenges of Nanoplasmonic Devices for Refractometric Biosensing. *Nanophotonics* **2**, 83–101 (2013). [Cited twice on page 3 and 80.]

[48] Anker, J. N., Hall, W. P., Lyandres, O., Shah, N. C., Zhao, J. & Van Duyne, R. P. Biosensing with plasmonic nanosensors. *Nature Materials* **7**, 442–53 (2008). [Cited 3 times on pages 3 and 79.]

[49] Kim, J. Joining plasmonics with microfluidics: from convenience to inevitability. *Lab on a Chip* **12**, 3611–23 (2012). [Cited once on page 3.]

[50] Jackson, J. D. *Classical Electrodynamics* (Wiley, 1998), 3rd edn. [Cited once on page 5.]

[51] Drude, P. Zur Elektronentheorie der Metalle. *Annalen der Physik* **306**, 566–613 (1900). [Cited once on page 9.]

[52] Stern, E. & Ferrell, R. Surface Plasma Oscillations of a Degenerate Electron Gas. *Physical Review* **120**, 130–136 (1960). [Cited once on page 10.]

[53] Raether, H. *Surface Plasmons on Smooth and Rough Surfaces and on Gratings*, vol. 111 of *Springer Tracts in Modern Physics* (Springer Berlin Heidelberg, Berlin, 1988). [Cited 4 times on pages 12, 13, and 36.]

[54] Hegner, M., Wagner, P. & Semenza, G. Ultralarge atomically flat template-stripped Au surfaces for scanning probe microscopy. *Surface Science* **291**, 39–46 (1993). [Cited once on page 17.]

[55] Nagpal, P., Lindquist, N. C., Oh, S.-H. & Norris, D. J. Ultrasmooth patterned metals for plasmonics and metamaterials. *Science* **325**, 594–7 (2009). [Cited 7 times on pages 18, 25, 30, 34, 41, 80, and 134.]

[56] Tao, T. Focused ion beam induced deposition of platinum. *Journal of Vacuum Science & Technology B* **8**, 1826 (1990). [Cited twice on page 19 and 27.]

[57] Weiss, E. A., Chiechi, R. C., Kaufman, G. K., Kriebel, J. K., Li, Z., Duati, M., Rampi, M. A. & Whitesides, G. M. Influence of defects on the electrical characteristics of mercury-drop junctions: self-assembled monolayers of n-alkanethiolates on rough and smooth silver. *Journal of the American Chemical Society* **129**, 4336–49 (2007). [Cited once on page 20.]

[58] Laux, E., Genet, C., Skauli, T. & Ebbesen, T. W. Plasmonic photon sorters for spectral and polarimetric imaging. *Nature Photonics* **2**, 161–164 (2008). [Cited once on page 23.]

[59] Tsakmakidis, K. L., Boardman, A. D. & Hess, O. 'Trapped rainbow' storage of light in metamaterials. *Nature* **450**, 397–401 (2007). [Cited once on page 23.]

[60] Gan, Q., Ding, Y. & Bartoli, F. Rainbow Trapping and Releasing at Telecommunication Wavelengths. *Physical Review Letters* **102**, 056801 (2009). [Cited once on page 23.]

[61] Grupp, D. E., Lezec, H. J., Thio, T. & Ebbesen, T. W. Beyond the Bethe Limit: Tunable Enhanced Light Transmission Through a Single Sub-Wavelength Aperture. *Advanced Materials* **11**, 860–862 (1999). [Cited once on page 26.]

[62] Lezec, H. J., Degiron, A., Devaux, E., Linke, R. a., Martin-Moreno, L., Garcia-Vidal, F. J. & Ebbesen, T. W. Beaming light from a subwavelength aperture. *Science* **297**, 820–2 (2002). [Cited 3 times on pages 26 and 84.]

[63] Hyuk Park, J., Nagpal, P., Oh, S.-H. & Norris, D. J. Improved dielectric functions in metallic films obtained via template stripping. *Applied Physics Letters* **100**, 081105 (2012). [Cited once on page 28.]

[64] Johnson, P. B. & Christy, R. W. Optical Constants of the Noble Metals. *Physical Review B* **6**, 4370–4379 (1972). [Cited 4 times on pages 28, 31, and 32.]

[65] Palik, E. D. *Handbook of Optical Constants of Solids* (Academic Press, San Diego, 1998). [Cited twice on page 28.]

[66] Thèye, M.-L. Investigation of the Optical Properties of Au by Means of Thin Semitransparent Films. *Physical Review B* **2**, 3060–3078 (1970). [Cited 3 times on pages 28, 31, and 32.]

[67] Weaver, J. H., Krafka, C., Lynch, D. W. & Koch, E. E. *Optical Properties of Metals, Pt. II* (Fachinformationszentrum Energie, Physik, Mathematik, 1981). [Cited 3 times on pages 28, 31, and 32.]

[68] Schulz, L. G. & Tangherlini, F. R. Optical Constants of Silver, Gold, Copper, and Aluminum II The Index of Refraction n. *Journal of the Optical Society of America* **44**, 362 (1954). [Cited 3 times on pages 28, 31, and 32.]

[69] Schulz, L. G. The Optical Constants of Silver, Gold, Copper, and Aluminum I The Absorption Coefficient k. *Journal of the Optical Society of America* **44**, 357 (1954). [Cited 3 times on pages 28, 31, and 32.]

[70] Tompkins, H. & Irene, E. A. (eds.) *Handbook of Ellipsometry* (William Andrew, 2005). [Cited once on page 31.]

[71] Blanchard, N. P., Smith, C., Martin, D. S., Hayton, D. J., Jenkins, T. E. & Weightman, P. High-resolution measurements of the bulk dielectric constants of single crystal gold with application to reflection anisotropy spectroscopy. *Physica Status Solidi C* **0**, 2931–2937 (2003). [Cited twice on page 31 and 32.]

[72] Gramotnev, D. K. & Bozhevolnyi, S. I. Plasmonics beyond the diffraction limit. *Nature Photonics* **4**, 83–91 (2010). [Cited twice on page 33.]

[73] Novotny, L. & van Hulst, N. Antennas for light. *Nature Photonics* **5**, 83–90 (2011). [Cited twice on page 33.]

[74] Novotny, L. & Hecht, B. *Principles of Nano-Optics 2nd Edition* (Cambridge University Press, 2012), 2 edn. [Cited 4 times on pages 33, 61, and 67.]

[75] Bharadwaj, P., Deutsch, B. & Novotny, L. Optical Antennas. *Advances in Optics and Photonics* **1**, 438 (2009). [Cited once on page 33.]

[76] Novotny, L., Bian, R. & Xie, X. Theory of Nanometric Optical Tweezers. *Physical Review Letters* **79**, 645–648 (1997). [Cited once on page 33.]

[77] Righini, M., Ghenuche, P., Cherukulappurath, S., Myroshnychenko, V., García de Abajo, F. J. & Quidant, R. Nano-optical trapping of Rayleigh particles and Escherichia coli bacteria with resonant optical antennas. *Nano Letters* **9**, 3387–91 (2009). [Cited once on page 33.]

[78] Pang, Y. & Gordon, R. Optical trapping of a single protein. *Nano Letters* **12**, 402–6 (2012). [Cited once on page 33.]

[79] Gullans, M., Tiecke, T. G., Chang, D. E., Feist, J., Thompson, J. D., Cirac, J. I., Zoller, P. & Lukin, M. D. Nanoplasmonic Lattices for Ultracold Atoms. *Physical Review Letters* **109**, 235309 (2012). [Cited once on page 33.]

[80] Bouhelier, A., Renger, J., Beversluis, M. R. & Novotny, L. Plasmon-coupled tip-enhanced near-field optical microscopy. *Journal of Microscopy* **210**, 220–224 (2003). [Cited 5 times on pages 33, 37, and 43.]

[81] Lesuffleur, A., Kumar, L. K. S. & Gordon, R. Enhanced second harmonic generation from nanoscale double-hole arrays in a gold film. *Applied Physics Letters* **88**, 261104 (2006). [Cited once on page 33.]

[82] Danckwerts, M. & Novotny, L. Optical Frequency Mixing at Coupled Gold Nanoparticles. *Physical Review Letters* **98**, 026104 (2007). [Cited once on page 33.]

[83] Ghenuche, P., Cherukulappurath, S., Taminiau, T. H., van Hulst, N. F. & Quidant, R. Spectroscopic Mode Mapping of Resonant Plasmon Nanoantennas. *Physical Review Letters* **101**, 116805 (2008). [Cited once on page 33.]

[84] Stipe, B. C., Strand, T. C., Poon, C. C., Balamane, H., Boone, T. D., Katine, J. A., Li, J.-L., Rawat, V., Nemoto, H., Hirotsune, A., Hellwig, O., Ruiz, R., Dobisz, E., Kercher, D. S., Robertson, N., Albrecht, T. R. & Terris, B. D. Magnetic recording at 1.5 Pb m2 using an integrated plasmonic antenna. *Nature Photonics* **4**, 484–488 (2010). [Cited once on page 33.]

[85] Wood, R. The feasibility of magnetic recording at 1 Terabit per square inch. *IEEE Transactions on Magnetics* **36**, 36–42 (2000). [Cited once on page 33.]

[86] Babadjanyan, A. J., Margaryan, N. L. & Nerkararyan, K. V. Superfocusing of surface polaritons in the conical structure. *Journal of Applied Physics* **87**, 3785 (2000). [Cited 4 times on pages 33, 35, and 38.]

[87] Stockman, M. Nanofocusing of Optical Energy in Tapered Plasmonic Waveguides. *Physical Review Letters* **93**, 137404 (2004). [Cited 6 times on pages 33, 35, 38, 72, and 73.]

[88] Chen, X.-W., Sandoghdar, V. & Agio, M. Highly efficient interfacing of guided plasmons and photons in nanowires. *Nano Letters* **9**, 3756–61 (2009). [Cited once on page 33.]

[89] Ropers, C., Neacsu, C. C., Elsaesser, T., Albrecht, M., Raschke, M. B. & Lienau, C. Grating-coupling of surface plasmons onto metallic tips: a nanoconfined light source. *Nano Letters* **7**, 2784–8 (2007). [Cited 4 times on pages 33, 39, and 72.]

[90] Verhagen, E., Polman, A. & Kuipers, L. K. Nanofocusing in laterally tapered plasmonic waveguides. *Optics Express* **16**, 45 (2008). [Cited once on page 33.]

[91] Miyazaki, H. & Kurokawa, Y. Squeezing Visible Light Waves into a 3-nm-Thick and 55-nm-Long Plasmon Cavity. *Physical Review Letters* **96**, 097401 (2006). [Cited twice on page 33 and 35.]

[92] Halas, N. J., Lal, S., Chang, W.-S., Link, S. & Nordlander, P. Plasmons in strongly coupled metallic nanostructures. *Chemical Reviews* **111**, 3913–61 (2011). [Cited twice on page 33 and 35.]

[93] Choo, H., Kim, M.-K., Staffaroni, M., Seok, T. J., Bokor, J., Cabrini, S., Schuck, P. J., Wu, M. C. & Yablonovitch, E. Nanofocusing in a metalinsulatormetal gap plasmon waveguide with a three-dimensional linear taper. *Nature Photonics* **6**, 838–844 (2012). [Cited 3 times on pages 33, 35, and 52.]

[94] Chen, X., Park, H.-R., Pelton, M., Piao, X., Lindquist, N. C., Im, H., Kim, Y. J., Ahn, J. S., Ahn, K. J., Park, N., Kim, D.-S. & Oh, S.-H. Atomic layer lithography of wafer-scale nanogap arrays for extreme confinement of electromagnetic waves. *Nature Communications* **4**, 2361 (2013). [Cited twice on page 33 and 35.]

[95] Berweger, S., Atkin, J. M., Olmon, R. L. & Raschke, M. B. Light on the Tip of a Needle: Plasmonic Nanofocusing for Spectroscopy on the Nanoscale. *The Journal of Physical Chemistry Letters* **3**, 945–952 (2012). [Cited once on page 33.]

[96] Cançado, L., Jorio, A., Ismach, A., Joselevich, E., Hartschuh, A. & Novotny, L. Mechanism of Near-Field Raman Enhancement in One-Dimensional Systems. *Physical Review Letters* **103**, 186101 (2009). [Cited 4 times on pages 33, 66, 69, and 72.]

[97] Wang, Y., Srituravanich, W., Sun, C. & Zhang, X. Plasmonic nearfield scanning probe with high transmission. *Nano Letters* **8**, 3041–3045 (2008). [Cited once on page 33.]

[98] Anger, P., Bharadwaj, P. & Novotny, L. Enhancement and Quenching of Single-Molecule Fluorescence. *Physical Review Letters* **96**, 113002 (2006). [Cited 4 times on pages 33, 62, 69, and 75.]

[99] Kalkbrenner, T., Hå kanson, U., Schädle, A., Burger, S., Henkel, C. & Sandoghdar, V. Optical Microscopy via Spectral Modifications of a Nanoantenna. *Physical Review Letters* **95**, 200801 (2005). [Cited once on page 33.]

[100] Eghlidi, H., Lee, K. G., Chen, X.-W., Gotzinger, S. & Sandoghdar, V. Resolution and Enhancement in Nanoantenna-Based Fluorescence Microscopy. *Nano Letters* **9**, 4007–4011 (2009). [Cited twice on page 33 and 62.]

[101] Höppener, C., Lapin, Z. J., Bharadwaj, P. & Novotny, L. Self-Similar Gold-Nanoparticle Antennas for a Cascaded Enhancement of the Optical Field. *Physical Review Letters* **109**, 017402 (2012). [Cited twice on page 33 and 62.]

[102] Taminiau, T. H., Stefani, F. D., Segerink, F. B. & van Hulst, N. F. Optical antennas direct single-molecule emission. *Nature Photonics* **2**, 234–237 (2008). [Cited twice on page 33 and 52.]

[103] Pitarke, J. M., Silkin, V. M., Chulkov, E. V. & Echenique, P. M. Theory of surface plasmons and surface-plasmon polaritons. *Reports on Progress in Physics* **70**, 1–87 (2007). [Cited once on page 36.]

[104] Takahara, J., Yamagishi, S., Taki, H., Morimoto, A. & Kobayashi, T. Guiding of a one-dimensional optical beam with nanometer diameter. *Optics Letters* **22**, 475 (1997). [Cited once on page 36.]

[105] Roth, R. M., Panoiu, N. C., Adams, M. M., Osgood, R. M., Neacsu, C. C. & Raschke, M. B. Resonant-plasmon field enhancement from asymmetrically illuminated conical metallic-probe tips. *Optics Express* **14**, 2921 (2006). [Cited once on page 37.]

[106] Nerkararyan, K. Superfocusing of a surface polariton in a wedge-like structure. *Physics Letters A* **237**, 103–105 (1997). [Cited once on page 38.]

[107] Pile, D. F. P. & Gramotnev, D. K. Adiabatic and nonadiabatic nanofocusing of plasmons by tapered gap plasmon waveguides. *Applied Physics Letters* **89**, 041111 (2006). [Cited twice on page 38 and 39.]

[108] Neacsu, C. C., Berweger, S., Olmon, R. L., Saraf, L. V., Ropers, C. & Raschke, M. B. Near-field localization in plasmonic superfocusing: a nanoemitter on a tip. *Nano Letters* **10**, 592–6 (2010). [Cited once on page 39.]

[109] Sánchez, E., Novotny, L. & Xie, X. Near-Field Fluorescence Microscopy Based on Two-Photon Excitation with Metal Tips. *Physical Review Letters* **82**, 4014–4017 (1999). [Cited 3 times on pages 39, 62, and 65.]

[110] Lindquist, N. C., Nagpal, P., Lesuffleur, A., Norris, D. J. & Oh, S.-H. Three-dimensional plasmonic nanofocusing. *Nano Letters* **10**, 1369–73 (2010). [Cited twice on page 39 and 98.]

[111] Wang, H., Wu, Y., Lassiter, B., Nehl, C. L., Hafner, J. H., Nordlander, P. & Halas, N. J. Symmetry breaking in individual plasmonic nanoparticles. *Proceedings of the National Academy of Sciences of the United States of America* **103**, 10856–60 (2006). [Cited once on page 39.]

[112] Hao, F., Sonnefraud, Y., Van Dorpe, P., Maier, S. A., Halas, N. J. & Nordlander, P. Symmetry breaking in plasmonic nanocavities: subradiant LSPR sensing and a tunable Fano resonance. *Nano Letters* **8**, 3983–3988 (2008). [Cited once on page 39.]

[113] Aydin, K., Pryce, I. M. & Atwater, H. A. Symmetry breaking and strong coupling in planar optical metamaterials. *Optics Express* **18**, 13407–17 (2010). [Cited once on page 39.]

[114] Lindquist, N. C., Nagpal, P., McPeak, K. M., Norris, D. J. & Oh, S.-H. Engineering metallic nanostructures for plasmonics and nanophotonics. *Reports on Progress in Physics* **75**, 036501 (2012). [Cited twice on page 41 and 80.]

[115] Suh, J. Y., Huntington, M. D., Kim, C. H., Zhou, W., Wasielewski, M. R. & Odom, T. W. Extraordinary nonlinear absorption in 3D bowtie nanoantennas. *Nano Letters* **12**, 269–74 (2012). [Cited once on page 41.]

[116] Garoli, D., Zilio, P., Natali, M., Carli, M., Enrichi, F. & Romanato, F. Wedge nanostructures for plasmonic nanofocusing. *Optics Express* **20**, 16224 (2012). [Cited once on page 42.]

[117] Tanaka, K., Burr, G. W., Grosjean, T., Maletzky, T. & Fischer, U. C. Superfocussing in a metal-coated tetrahedral tip by dimensional reduction of surface-to edge-plasmon modes. *Applied Physics B* **93**, 257–266 (2008). [Cited twice on page 43 and 44.]

[118] Neumann, L., Pang, Y., Houyou, A., Juan, M. L., Gordon, R. & van Hulst, N. F. Extraordinary optical transmission brightens near-field fiber probe. *Nano Letters* **11**, 355–60 (2011). [Cited once on page 46.]

[119] Betzig, E. & Trautman, J. K. Near-field optics: microscopy, spectroscopy, and surface modification beyond the diffraction limit. *Science* **257**, 189–95 (1992). [Cited once on page 52.]

[120] Frey, H. G., Keilmann, F., Kriele, A. & Guckenberger, R. Enhancing the resolution of scanning near-field optical microscopy by a metal tip grown on an aperture probe. *Applied Physics Letters* **81**, 5030 (2002). [Cited twice on page 52.]

[121] Weber-Bargioni, A., Schwartzberg, A., Cornaglia, M., Ismach, A., Urban, J. J., Pang, Y., Gordon, R., Bokor, J., Salmeron, M. B., Ogletree, D. F., Ashby, P.,

Cabrini, S. & Schuck, P. J. Hyperspectral nanoscale imaging on dielectric substrates with coaxial optical antenna scan probes. *Nano Letters* **11**, 1201–7 (2011). [Cited once on page 52.]

[122] Gordon, R., Brolo, A., McKinnon, A., Rajora, A., Leathem, B. & Kavanagh, K. Strong Polarization in the Optical Transmission through Elliptical Nanohole Arrays. *Physical Review Letters* **92**, 037401 (2004). [Cited once on page 52.]

[123] van der Molen, K. L., Segerink, F. B., van Hulst, N. F. & Kuipers, L. Influence of hole size on the extraordinary transmission through subwavelength hole arrays. *Applied Physics Letters* **85**, 4316 (2004). [Cited once on page 52.]

[124] Shi, X., Hesselink, L. & Thornton, R. L. Ultrahigh light transmission through a C-shaped nanoaperture. *Optics Letters* **28**, 1320 (2003). [Cited once on page 52.]

[125] Lee, B., Lee, I.-M., Kim, S., Oh, D.-H. & Hesselink, L. Review on subwavelength confinement of light with plasmonics. *Journal of Modern Optics* **57**, 1479–1497 (2010). [Cited twice on page 52 and 54.]

[126] Leen, J. B., Hansen, P., Cheng, Y.-T. & Hesselink, L. Improved focused ion beam fabrication of near-field apertures using a silicon nitride membrane. *Optics Letters* **33**, 2827 (2008). [Cited once on page 52.]

[127] Cheng, Y.-T., Takashima, Y., Yuen, Y., Hansen, P. C., Leen, J. B. & Hesselink, L. Ultra-high resolution resonant C-shaped aperture nano-tip. *Optics Express* **19**, 5077–85 (2011). [Cited once on page 54.]

[128] Synge, E. A suggested method for extending microscopic resolution into the ultra-microscopic region. *Philosophical Magazine Series 7* **6**, 356–362 (1928). [Cited once on page 61.]

[129] Ash, E. A. & Nicholls, G. Super-resolution Aperture Scanning Microscope. *Nature* **237**, 510–512 (1972). [Cited once on page 61.]

[130] Lewis, A., Isaacson, M., Harootunian, A. & Muray, A. Development of a 500 Åspatial resolution light microscope. *Ultramicroscopy* **13**, 227–231 (1984). [Cited once on page 61.]

[131] Pohl, D. W., Denk, W. & Lanz, M. Optical stethoscopy: Image recording with resolution $\lambda/20$. *Applied Physics Letters* **44**, 651 (1984). [Cited once on page 61.]

[132] Reddick, R., Warmack, R. & Ferrell, T. New form of scanning optical microscopy. *Physical Review B* **39**, 767–770 (1989). [Cited once on page 61.]

[133] Fischer, U. & Pohl, D. Observation of Single-Particle Plasmons by Near-Field Optical Microscopy. *Physical Review Letters* **62**, 458–461 (1989). [Cited once on page 61.]

[134] Hecht, B., Sick, B., Wild, U. P., Deckert, V., Zenobi, R., Martin, O. J. F. & Pohl, D. W. Scanning near-field optical microscopy with aperture probes: Fundamentals and applications. *The Journal of Chemical Physics* **112**, 7761 (2000). [Cited once on page 62.]

[135] Zenhausern, F., OBoyle, M. P. & Wickramasinghe, H. K. Apertureless near-field optical microscope. *Applied Physics Letters* **65**, 1623 (1994). [Cited once on page 62.]

[136] Keilmann, F. & Hillenbrand, R. Near-field microscopy by elastic light scattering from a tip. *Philosophical transactions. Series A, Mathematical, physical, and engineering sciences* **362**, 787–805 (2004). [Cited once on page 62.]

[137] Novotny, L. & Stranick, S. J. Near-field optical microscopy and spectroscopy with pointed probes. *Annual Review of Physical Chemistry* **57**, 303–31 (2006). [Cited once on page 62.]

[138] Dorfmüller, J., Dregely, D., Esslinger, M., Khunsin, W., Vogelgesang, R., Kern, K. & Giessen, H. Near-field dynamics of optical Yagi-Uda nanoantennas. *Nano Letters* **11**, 2819–24 (2011). [Cited once on page 62.]

[139] Jones, A. C., Olmon, R. L., Skrabalak, S. E., Wiley, B. J., Xia, Y. N. & Raschke, M. B. Mid-IR plasmonics: near-field imaging of coherent plasmon modes of silver nanowires. *Nano Letters* **9**, 2553–8 (2009). [Cited once on page 62.]

[140] Schnell, M., Alonso-González, P., Arzubiaga, L., Casanova, F., Hueso, L. E., Chuvilin, A. & Hillenbrand, R. Nanofocusing of mid-infrared energy with tapered transmission lines. *Nature Photonics* **5**, 283–287 (2011). [Cited once on page 62.]

[141] Garcia-Parajo, M. F. Optical antennas focus in on biology. *Nature Photonics* **2**, 201–203 (2008). [Cited once on page 62.]

[142] Huber, A. J., Wittborn, J. & Hillenbrand, R. Infrared spectroscopic near-field mapping of single nanotransistors. *Nanotechnology* **21**, 235702 (2010). [Cited once on page 62.]

[143] Gerton, J., Wade, L., Lessard, G., Ma, Z. & Quake, S. Tip-Enhanced Fluorescence Microscopy at 10 Nanometer Resolution. *Physical Review Letters* **93**, 180801 (2004). [Cited once on page 62.]

[144] Frey, H., Witt, S., Felderer, K. & Guckenberger, R. High-Resolution Imaging of Single Fluorescent Molecules with the Optical Near-Field of a Metal Tip. *Physical Review Letters* **93**, 200801 (2004). [Cited once on page 62.]

[145] Anderson, N., Hartschuh, A., Cronin, S. & Novotny, L. Nanoscale Vibrational Analysis of Single-Walled Carbon Nanotubes. *Journal of the American Chemical Society* **127**, 2533–2537 (2005). [Cited 3 times on pages 62, 66, and 69.]

[146] Stöckle, R. M., Suh, Y. D., Deckert, V. & Zenobi, R. Nanoscale chemical analysis by tip-enhanced Raman spectroscopy. *Chemical Physics Letters* **318**, 131–136 (2000). [Cited once on page 62.]

[147] Ichimura, T., Hayazawa, N., Hashimoto, M., Inouye, Y. & Kawata, S. Tip-Enhanced Coherent Anti-Stokes Raman Scattering for Vibrational Nanoimaging. *Physical Review Letters* **92**, 220801 (2004). [Cited twice on page 62 and 69.]

[148] Kühn, S., Hå kanson, U., Rogobete, L. & Sandoghdar, V. Enhancement of Single-Molecule Fluorescence Using a Gold Nanoparticle as an Optical Nanoantenna. *Physical Review Letters* **97**, 017402 (2006). [Cited 4 times on pages 62, 69, and 75.]

[149] Bharadwaj, P. & Novotny, L. Plasmon-Enhanced Photoemission from a Single Y 3 N@C 80 Fullerene. *The Journal of Physical Chemistry C* **114**, 7444–7447 (2010). [Cited once on page 62.]

[150] Henzie, J., Kwak, E.-S. & Odom, T. W. Mesoscale Metallic Pyramids with Nanoscale Tips. *Nano Letters* **5**, 1199–1202 (2005). [Cited once on page 64.]

[151] Kim, B. J., Flamma, J. W., Ten Have, E. S., Garcia-Parajo, M. F., Van Hulst, N. F. & Brugger, J. Moulded photoplastic probes for near-field optical applications. *Journal of Microscopy* **202**, 16–21 (2001). [Cited once on page 64.]

[152] Kim, G. M., Kim, B. J., Ten Have, E. S., Segerink, F., Van Hulst, N. F. & Brugger, J. Photoplastic near-field optical probe with sub-100 nm aperture made by replication from a nanomould. *Journal of Microscopy* **209**, 267–271 (2003). [Cited once on page 64.]

[153] Karrai, K. & Grober, R. D. Piezoelectric tip-sample distance control for near field optical microscopes. *Applied Physics Letters* **66**, 1842 (1995). [Cited once on page 67.]

[154] Novotny, L., Beversluis, M., Youngworth, K. & Brown, T. Longitudinal Field Modes Probed by Single Molecules. *Physical Review Letters* **86**, 5251–5254 (2001). [Cited twice on page 69.]

[155] Chang, D., Sø rensen, A., Hemmer, P. & Lukin, M. Strong coupling of single emitters to surface plasmons. *Physical Review B* **76**, 035420 (2007). [Cited once on page 72.]

[156] Issa, N. A. & Guckenberger, R. Fluorescence near metal tips: The roles of energy transfer and surface plasmon polaritons. *Optics Express* **15**, 12131 (2007). [Cited once on page 72.]

[157] Curto, A. G., Volpe, G., Taminiau, T. H., Kreuzer, M. P., Quidant, R. & van Hulst, N. F. Unidirectional emission of a quantum dot coupled to a nanoantenna. *Science* **329**, 930–3 (2010). [Cited once on page 75.]

[158] Farahani, J. N., Pohl, D. W., Eisler, H.-J. & Hecht, B. Single Quantum Dot Coupled to a Scanning Optical Antenna: A Tunable Superemitter. *Physical Review Letters* **95**, 017402 (2005). [Cited twice on page 75.]

[159] Ropp, C., Cummins, Z., Nah, S., Fourkas, J. T., Shapiro, B. & Waks, E. Nanoscale imaging and spontaneous emission control with a single nano-positioned quantum dot. *Nature Communications* **4**, 1447 (2013). [Cited once on page 75.]

[160] Yoshie, T., Scherer, A., Hendrickson, J., Khitrova, G., Gibbs, H. M., Rupper, G., Ell, C., Shchekin, O. B. & Deppe, D. G. Vacuum Rabi splitting with a single quantum dot in a photonic crystal nanocavity. *Nature* **432**, 200–3 (2004). [Cited once on page 75.]

[161] Henkel, C. & Sandoghdar, V. Single-molecule spectroscopy near structured dielectrics. *Optics Communications* **158**, 250–262 (1998). [Cited once on page 75.]

[162] Rahmani, A., Chaumet, P., de Fornel, F. & Girard, C. Field propagator of a dressed junction: Fluorescence lifetime calculations in a confined geometry. *Physical Review A* **56**, 3245–3254 (1997). [Cited once on page 75.]

[163] Michaelis, J., Hettich, C., Mlynek, J. & Sandoghdar, V. Optical microscopy using a single-molecule light source. *Nature* **405**, 325–8 (2000). [Cited once on page 75.]

[164] Kuhn, S., Hettich, C., Schmitt, C., Poizat, J.-P. & Sandoghdar, V. Diamond colour centres as a nanoscopic light source for scanning near-field optical microscopy. *Journal of Microscopy* **202**, 2–6 (2001). [Cited once on page 75.]

[165] Dahlin, A., Zäch, M., Rindzevicius, T., Käll, M., Sutherland, D. S. & Höök, F. Localized surface plasmon resonance sensing of lipid-membrane-mediated biorecognition events. *Journal of the American Chemical Society* **127**, 5043–8 (2005). [Cited 3 times on pages 79.]

[166] Homola, J. Surface plasmon resonance sensors for detection of chemical and biological species. *Chemical Reviews* **108**, 462–493 (2008). [Cited 3 times on pages 79.]

[167] Homola, J., Yee, S. S. & Gauglitz, G. Surface plasmon resonance sensors: review. *Sensors and Actuators B: Chemical* **54**, 3–15 (1999). [Cited 3 times on pages 79 and 84.]

[168] Gordon, R., Sinton, D., Kavanagh, K. L. & Brolo, A. G. A new generation of sensors based on extraordinary optical transmission. *Accounts of Chemical Research* **41**, 1049–1057 (2008). [Cited twice on page 79 and 80.]

[169] Liedberg, B., Nylander, C. & Lundström, I. Biosensing with surface plasmon resonance how it all started. *Biosensors and Bioelectronics* **10**, i–ix (1995). [Cited once on page 79.]

[170] Rindzevicius, T., Alaverdyan, Y., Dahlin, A., Höök, F., Sutherland, D. S. & Käll, M. Plasmonic sensing characteristics of single nanometric holes. *Nano Letters* **5**, 2335–2339 (2005). [Cited once on page 79.]

[171] Tetz, K. A., Pang, L. & Fainman, Y. High-resolution surface plasmon resonance sensor based on linewidth-optimized nanohole array transmittance. *Optics Letters* **31**, 1528–1530 (2006). [Cited twice on page 79 and 80.]

[172] Lesuffleur, A., Im, H., Lindquist, N. C. & Oh, S.-H. Periodic nanohole arrays with shape-enhanced plasmon resonance as real-time biosensors. *Applied Physics Letters* **90**, 243110 (2007). [Cited once on page 79.]

[173] Yang, J.-C., Ji, J., Hogle, J. M. & Larson, D. N. Metallic nanohole arrays on fluoropolymer substrates as small label-free real-time bioprobes. *Nano Letters* **8**, 2718–24 (2008). [Cited once on page 79.]

[174] Eftekhari, F., Escobedo, C., Ferreira, J., Duan, X., Girotto, E. M., Brolo, A. G., Gordon, R. & Sinton, D. Nanoholes as nanochannels: flow-through plasmonic sensing. *Analytical Chemistry* **81**, 4308–11 (2009). [Cited once on page 79.]

[175] Masson, J.-F., Murray-Méthot, M.-P. & Live, L. S. Nanohole arrays in chemical analysis: manufacturing methods and applications. *The Analyst* **135**, 1483–9 (2010). [Cited once on page 79.]

[176] Yanik, A. A., Huang, M., Kamohara, O., Artar, A., Geisbert, T. W., Connor, J. H. & Altug, H. An optofluidic nanoplasmonic biosensor for direct detection of live viruses from biological media. *Nano Letters* **10**, 4962–9 (2010). [Cited once on page 79.]

[177] Nakamoto, K., Kurita, R. & Niwa, O. Electrochemical surface plasmon resonance measurement based on gold nanohole array fabricated by nanoimprinting technique. *Analytical chemistry* **84**, 3187–91 (2012). [Cited once on page 79.]

[178] McFarland, A. D. & Van Duyne, R. P. Single Silver Nanoparticles as Real-Time Optical Sensors with Zeptomole Sensitivity. *Nano Letters* **3**, 1057–1062 (2003). [Cited once on page 79.]

[179] Sonnefraud, Y., Verellen, N., Sobhani, H., Vandenbosch, G. A. E., Moshchalkov, V. V., Van Dorpe, P., Nordlander, P. & Maier, S. A. Experimental realization of subradiant, superradiant, and fano resonances in ring/disk plasmonic nanocavities. *ACS Nano* **4**, 1664–1670 (2010). [Cited once on page 79.]

[180] Gao, Y., Gan, Q., Xin, Z., Cheng, X. & Bartoli, F. J. Plasmonic Mach-Zehnder interferometer for ultrasensitive on-chip biosensing. *ACS Nano* **5**, 9836–44 (2011). [Cited twice on page 79 and 81.]

[181] Feng, J., Siu, V. S., Roelke, A., Mehta, V., Rhieu, S. Y., Palmore, G. T. R. & Pacifici, D. Nanoscale plasmonic interferometers for multispectral, high-throughput biochemical sensing. *Nano Letters* **12**, 602–9 (2012). [Cited once on page 79.]

[182] Piliarik, M., Vaisocherová, H. & Homola, J. A new surface plasmon resonance sensor for high-throughput screening applications. *Biosensors & Bioelectronics* **20**, 2104–10 (2005). [Cited once on page 79.]

[183] Shumaker-Parry, J. S., Aebersold, R. & Campbell, C. T. Parallel, quantitative measurement of protein binding to a 120-element double-stranded DNA array in real time using surface plasmon resonance microscopy. *Analytical Chemistry* **76**, 2071–2082 (2004). [Cited once on page 79.]

[184] Dostálek, J., Homola, J. & Miler, M. Rich information format surface plasmon resonance biosensor based on array of diffraction gratings. *Sensors and Actuators B: Chemical* **107**, 154–161 (2005). [Cited once on page 79.]

[185] Spinke, J., Yang, J., Wolf, H., Liley, M., Ringsdorf, H. & Knoll, W. Polymer-supported bilayer on a solid substrate. *Biophysical Journal* **63**, 1667–1671 (1992). [Cited once on page 80.]

[186] Cooper, M. A. Advances in membrane receptor screening and analysis. *Journal of Molecular Recognition* **17**, 286–315 (2004). [Cited once on page 80.]

[187] Naumann, R., Schiller, S. M., Giess, F., Grohe, B., Hartman, K. B., Kärcher, I., Köper, I., Lübben, J., Vasilev, K. & Knoll, W. Tethered Lipid Bilayers on Ultraflat Gold Surfaces. *Langmuir* **19**, 5435–5443 (2003). [Cited once on page 80.]

[188] Rueda, A., Vogel, N. & Kreiter, M. Characterization of gold films by surface plasmon spectroscopy: Large errors and small consequences. *Surface Science* **603**, 491–497 (2009). [Cited once on page 80.]

[189] Vogel, N., Zieleniecki, J. & Köper, I. As flat as it gets: ultrasmooth surfaces from template-stripping procedures. *Nanoscale* **4**, 3820–32 (2012). [Cited once on page 80.]

[190] Love, J. C., Estroff, L. A., Kriebel, J. K., Nuzzo, R. G. & Whitesides, G. M. Self-assembled monolayers of thiolates on metals as a form of nanotechnology. *Chemical Reviews* **105**, 1103–1169 (2005). [Cited once on page 80.]

[191] Ebbesen, T. W., Genet, C. & Bozhevolnyi, S. I. Surface-plasmon circuitry. *Physics Today* **61**, 44 (2008). [Cited once on page 81.]

[192] Castellana, E. T. & Cremer, P. S. Solid supported lipid bilayers: From biophysical studies to sensor design. *Surface Science Reports* **61**, 429–444 (2006). [Cited once on page 81.]

[193] Ouellet, E., Lausted, C., Lin, T., Yang, C. W. T., Hood, L. & Lagally, E. T. Parallel microfluidic surface plasmon resonance imaging arrays. *Lab on a Chip* **10**, 581–8 (2010). [Cited once on page 84.]

[194] Teperik, T. V., Popov, V. V., García de Abajo, F. J., Abdelsalam, M., Bartlett, P. N., Kelf, T. a., Sugawara, Y. & Baumberg, J. J. Strong coupling of light to flat metals via a buried nanovoid lattice: the interplay of localized and free plasmons. *Optics Express* **14**, 1965 (2006). [Cited twice on page 86 and 87.]

[195] Barnes, W. L. Surface plasmonpolariton length scales: a route to sub-wavelength optics. *Journal of Optics A: Pure and Applied Optics* **8**, S87–S93 (2006). [Cited once on page 87.]

[196] Klar, T., Perner, M., Grosse, S., von Plessen, G., Spirkl, W. & Feldmann, J. Surface-Plasmon Resonances in Single Metallic Nanoparticles. *Physical Review Letters* **80**, 4249–4252 (1998). [Cited once on page 87.]

[197] Giudicatti, S., Marabelli, F., Valsesia, A., Pellacani, P., Colpo, P. & Rossi, F. Interaction among plasmonic resonances in a gold film embedding a two-dimensional array of polymeric nanopillars. *Journal of the Optical Society of America B* **29**, 1641 (2012). [Cited once on page 87.]

[198] Burke, J., Stegeman, G. & Tamir, T. Surface-polariton-like waves guided by thin, lossy metal films. *Physical Review B* **33**, 5186–5201 (1986). [Cited once on page 88.]

[199] Kelf, T., Sugawara, Y., Cole, R., Baumberg, J., Abdelsalam, M., Cintra, S., Mahajan, S., Russell, A. & Bartlett, P. Localized and delocalized plasmons in metallic nanovoids. *Physical Review B* **74**, 245415 (2006). [Cited once on page 89.]

[200] Sannomiya, T., Scholder, O., Jefimovs, K., Hafner, C. & Dahlin, A. B. Investigation of plasmon resonances in metal films with nanohole arrays for biosensing applications. *Small* **7**, 1653–1663 (2011). [Cited once on page 89.]

[201] Whitney, A. V., Elam, J. W., Zou, S., Zinovev, A. V., Stair, P. C., Schatz, G. C. & Van Duyne, R. P. Localized surface plasmon resonance nanosensor: a high-resolution distance-dependence study using atomic layer deposition. *The Journal of Physical Chemistry B* **109**, 20522–20528 (2005). [Cited once on page 90.]

[202] Im, H., Lindquist, N. C., Lesuffleur, A. & Oh, S.-H. Atomic layer deposition of dielectric overlayers for enhancing the optical properties and chemical stability of plasmonic nanoholes. *ACS Nano* **4**, 947–54 (2010). [Cited once on page 90.]

[203] Oh, S.-H. & Johnson, T. W. Method of Forming Individual Metallic Microstructures. International Patent No. WO/2014/003843 (2014). [Cited once on page 94.]

[204] Im, H. & Oh, S.-H. Oxidation Sharpening, Template Stripping, and Passivation of Ultra-Sharp Metallic Pyramids and Wedges. *Small* 1–5 (2013). [Cited twice on page 95 and 135.]

[205] Park, J. H., Nagpal, P., McPeak, K. M., Lindquist, N. C., Oh, S.-H. & Norris, D. J. Fabrication of smooth patterned structures of refractory metals, semiconductors, and oxides via template stripping. *ACS Applied Materials & Interfaces* **5**, 9701–8 (2013). [Cited once on page 101.]

[206] Nielsen, C. B., Christensen, C., Pedersen, C. & Thomsen, E. V. Particle Precipitation in Connection with KOH Etching of Silicon. *Journal of The Electrochemical Society* **151**, G338 (2004). [Cited once on page 135.]

Appendix A

Fabrication Methods and Recipes

A.1 Isolated gold pyramid fabrication

A.1.1 Basic fabrication process

1. Start with a prime <100> wafer coated with 400 ÅSi_3N_4
2. Pattern wafter with circular holes

   Method 1: Photolithography

   (a) Bake at 120°C for 5 min

   (b) Put in vapor HMDS for 3 min

   (c) Spin coat S1805 photoresist on wafer at 6000 ROM for 30 sec

   (d) Bake at 115°C for 1 min

   (e) Expose to mask with circles in stepper with a dose of 125 mJ/cm^2

   (f) Bake at 115°C for 1 min

   (g) Develop in 351:H_2O 1:5 for 35 sec

   (h) Rinse with DI water

   (i) Dry with N_2

Mathod 2: E-beam lithography

(a) Spin coat PMMA 950 C4 at 3500 RPM for 30 sec

(b) Back at 180°C for 10 min

(c) Write pattern with circles on Vistec

(d) Develop in MIBK:IPA 1:3 for 35 sec

(e) Rinse with IPA

(f) Dry with N_2

3. Etch in AV etcher for 15 sec (50 watts power; 100 mTorr pressure; 100 SCCM O_2)

4. Etch nitride in AV etcher for 2.25 min (100 watts power; 30 mTorr pressure; 12 SCCM CHF_3, 42.5 SCCM N_2, 3 SCCM O_2)

5. Etch PMMA away in AV etcher for 15 min (O_2Clean recipe)

6. Etch in KOH for 60 min (30% KOH saturated with IPA at 80°C, with wafer face up)

7. Rinse for 10 min in H_2O

8. Etch iron oxide particles in 1:5 HCl:H_2O for 5 min

9. Rinse for 10 min in H_2O

10. Clean in H_2SO_4:H_2O_2 1:1 at 120°C for 25 min

11. Rinse in H_2O

12. Dip in 10:1 BOE for 10 sec

13. Rinse in H_2O

14. Clean in H_2SO_4:H_2O_2 1:1 at 120°C for 5 min

15. Rinse in H_2O
16. Dry with N_2
17. Deposit Au on wafer in AJA-2 sputterer system. 300 sec of Au deposition (about 250 nm).
18. Lift-off by etching nitride in HF 49% for 7 min (or until nitride is gone making the surface hydrophobic)
19. Inspect pyramid tips by SEM

A.1.2 Deposition for Ag pyramids

For silver, the deposition conditions found to be the best are using the CHA evaporator with an initial rate of 0.5 Åper sec for the first 50 nm, then up to 2 Åper sec until the final thickness of 200 nm. A gold backing layer can also be added for protection.

A.1.3 Deposition optimization

For these pyramids the size of the tip is a very important trait. For a particular metal, the tip radius is dependent on not only the mold, but also the deposition conditions of the metal. Figure (A.1) demonstrates this fact by looking at cross-sectional SEM images of wedges. In both of the cases the mold is very sharp (about 2 nm radius), but the filling is different between the two. Figure (A.1a) shows a good deposition with the tip radius of the metal being around 5 nm. It should be noted that the metal wedge pulled slightly away from the mold during the cross-sectioning, but the tip can still clearly be seen. Figure (A.1b), on the other hand, shows metal which was poorly deposited and the tip has a much larger radius of curvature. It had previously been shown that very slow deposition produces the smoothest films when template stripping flat films,[55] but it does not give the best tips. Experiments show that fast sputtering gives the sharpest tips when using gold. This may be due to the increased energy of the particles compared

to e-beam evaporated metal, but another likely case is that it is due to temperature. If the deposition rate is slow, the deposition takes a long time which give the substrate a long time to heat up. It has been shown that a sharp tip left at room temperature for 2 weeks will blunt itself due to ion migration,[204] and an increase in temperature will speed this process up. With the optimal deposition conditions sharp pyramids can consistently be made.

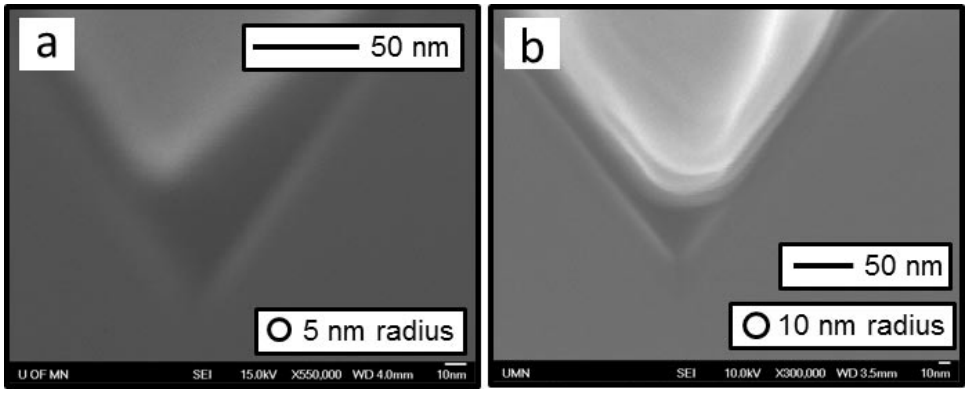

Figure A.1: **Cross-sectional SEM image of metal deposited in a wedge mold.** (a) Demonstrates a sharp tip while (b) shows a tip which is significantly more blunt. Changing the deposition conditions can vary the sharpness of the tip.

A.1.4 Removal of Iron Oxide

Another problem which can occur during fabrication of the pyramidal molds is the precipitation of iron oxide particles.[206] During the KOH etching process there can be small amounts of iron present in the solution which can then precipitate on the surface. Figure (A.2) shows SEM images of the precipitated particles on a pyramid mold after KOH etching. To remove these particles the silicon wafer should be placed in a bath of 1:5 HCl:H_2O for 5 min after KOH etching. This will remove the particles which are unwanted in future steps.

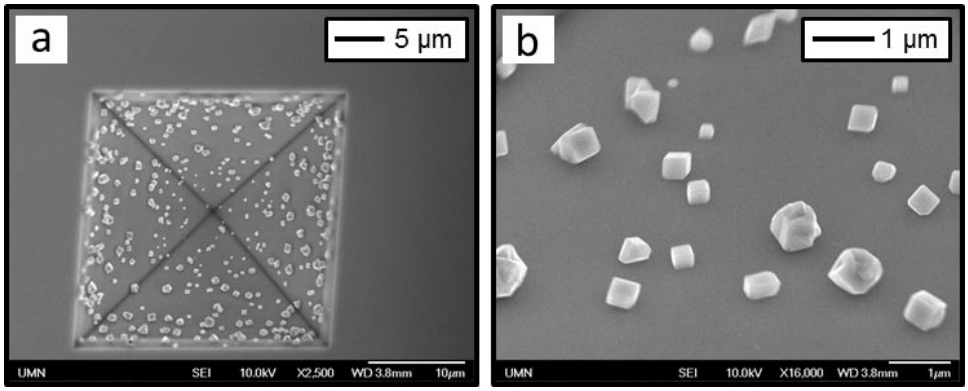

Figure A.2: **Iron oxide particles precipitated during KOH etching.** SEM images of the iron oxide particles. The particles can be removed in a bath of HCl.

A.1.5 Knife Edges

Another common problem when making pyramids is knife edges. When a pyramid is etched, we want for it to come to a single point, such as the ones shown in the SEM images of Figures (A.3a-c). It is also possible for the pyramid to come to two points where a line connects the two points. This is called a knife edge and is shown in Figures (A.3d-f). The knife edge pyramid is essentially a small wedge. It is known that if the initial etch mask for KOH etching is an oval, it will make a wedge-shaped structure. As this oval becomes more like a circle, the wedge will become more like a pyramid. This is because of how the KOH anisotropically etches by leaving the (111) planes exposed. To make a perfect pyramid, an oval needs to be patterned with a minor and major axis of the same length. Any difference between the minor and major axis will result in a knife edge of that size. This leads to a very tight tolerance. The pyramids generally have a diameter of 20 μm and so to get a 10 nm knife edge or less the tolerance between the two axes is 2000:1.

To keep within this tolerance, all the the steps in the process need to be precisely controlled. First, the mask for the photolithography needs to be made. The trouble

is that the mask-making machine isn't always perfectly calibrated. To calibrate it I made many different masks with various offsets. I then make pyramid molds and could determine which offset was needed for the machine to make perfect circles. Next, the photolithography process needs to be tuned and adjusted to find an optimized process. It is also helpful to use a 5x stepper for the exposure as to reduce and error caused by the photomask. Also, the process for etching the silicon nitride needs to be optimized. The recipe needed to be tuned to give as good of a selectivity of silicon nitride over silicon and the etch time was tuned to not over-etch into the silicon. Finally, the position and orientation of the wafer in the KOH bath needs to be optimized. I found that the wafers should either be periodically rotated during the etch or that they can be placed face up. With these optimizations it is possible to produce wafers where 95% of the pyramids have less than a 20 nm knife edge.

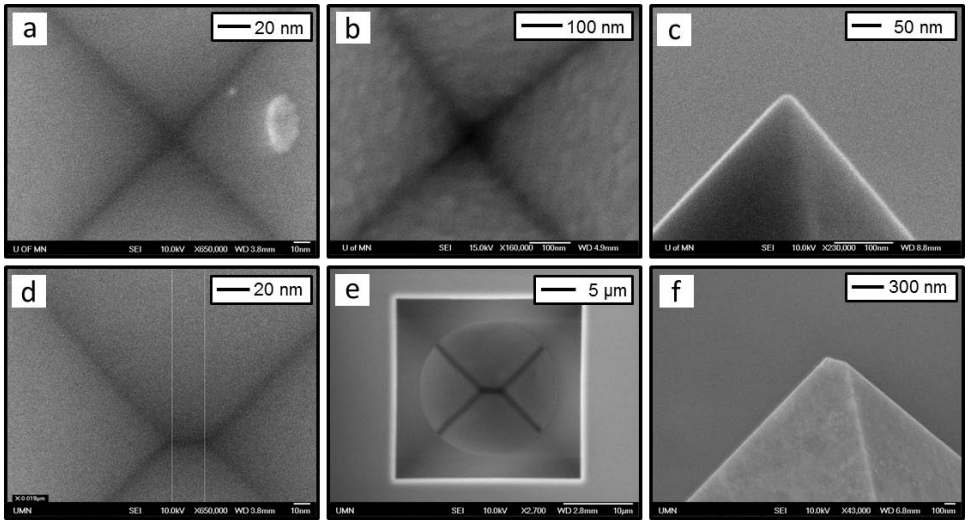

Figure A.3: **Comparison of pyramids with and without knife edges.** SEM images are shown comparing pyramids and molds with and without knife edges. Panels (a)-(c) don't have knife edges while (d)-(f) have knife edges. Panels (a) and (d) are looking into the Si mold after KOH etching, but before metal deposition. Panels (b) and (e) are looking to the mold before template stripping, but after metal deposition. Panels (c) and (f) show the final template stripped pyramids.

A.1.6 Optimization of mold etching

To make a pyramids with a sharp tip, it is important to have a sharp mold. Figure (A.4a) shows an example of a mold not etched well which is not sharp and thus will not produce sharp pyramids. Figure (A.4b) shows an example of a mold which is etched well and a very sharp point is reached. To consistently get sharp molds it is important to optimize the KOH etching recipe. I found that etching the molds for 60 min in a solution of 30% KOH saturated with IPA at 80°C will consistently give a sharp mold.

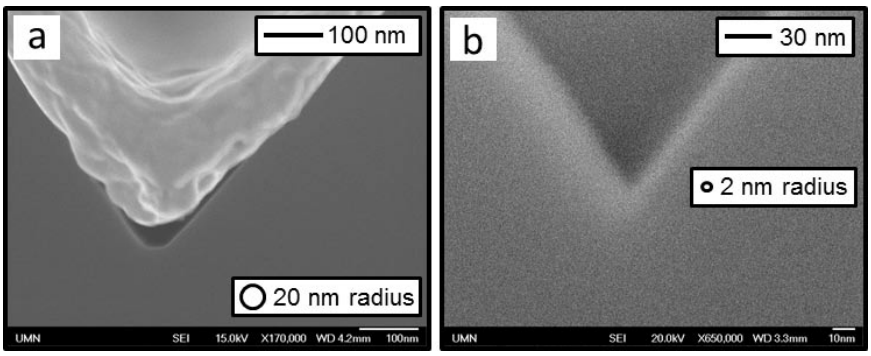

Figure A.4: **Optimization of mold etching** (a) SEM image of a mold which was not etched correctly and so does not come to a sharp point. (b) SEM image of a mold etched with optimized conditions to produce a mold where the point has about a 2 nm radius.

A.2 Fabrication of gratings from Chapter 3

1. FIB milling of patterns

   (a) Start with clean <100> silicon wafter

   (b) System used: FEI Dual Bean Quanta 200 3D

   (c) Milling current 50 pA and 30 kV accelerating voltage

   (d) For grooves: adjust milling times to create grooves of slightly different depths

   (e) For bumps: ion induced deposition of platinum done with a current of 10 pA and 30 kV accelerating voltage beam

2. Deposit 11 nm thick layer of silica via atomic layer deposition (Cambridge Nano Tech, Inc.)

3. Metal deposition

   (a) Using CHA SEC600 e-beam evaporator

   (b) Base pressure of 2×10^{-6} Torr

   (c) 300 nm Ag deposited at 0.1 Å per second initially, and 1 Å per sec after 50 nm (100 nm for bump and aperture devices)

   (d) Anneal at 200 °C for 10 min in rapid thermal annealer (RPT-600S)

4. Template strip

   (a) Apply optical epoxy (Norland Products, NOA 61) between sample and clean glass slide

   (b) Cure under UV lamp

   (c) Age on hotplate for 12 hours at 55 °C

   (d) Use razor blade to separate silicon wafer and glass slide

A.3 Fabrication of asymmetric pyramids from Chapter 4

1. Start with a pyramid mold using the fabrication as described above

2. Mount the mold at an angle of around 15° in the deposition chamber

3. Deposit 120 nm of Ag or Au in the CHA evaporator. Start with a deposition rate of 0.2 Åper sec and increase to 1 Åper sec after the first 40 Å

4. Template strip using the method described previously

Appendix B

Common Acronyms

Table B.1: A listing of the common acronyms used throughout the dissertation text.

Acronym	**Definition**
AFM	Atomic Force Microscope
APD	Avalanche Photodiode
BR	Backward Radiation
CNT	Carbon Nanotube
FDTD	Finite Difference Time Domain
FEM	Finite Element Method
FIB	Focused Ion Beam
FLIM	Fluorescence Lifetime Imaging Microscopy
IPA	Isopropanol
KOH	Potassium Hydroxide
LDOS	Local Density of Optical States
LSPR	Localized Surface Plasmon Resonance

Continued on next page

Table B.1 – continued from previous page

Acronym	Meaning
NSOM	Near-field Scanning Optical Microscopy
PDMS	Polydimethylsiloxane
PMMA	Polymethyl Methacrylate
RIU	Refractive Index Unit
RMS	Root-Mean-Square
SAM	Self Assembled Monolayer
SEM	Scanning Electron Micrograph
SERS	Surface Enhanced Raman Spectroscopy
SP	Surface Plasmon
SPP	Surface Plasmon Polariton
SPR	Surface Plasmon Resonance